NOTE TO USERS

University of Alberta

MULTI-DIMENSIONAL RECONSTRUCTION OF SEISMIC DATA

by

Bin Liu 

A thesis submitted to the Faculty of Graduate Studies and Research in partial fulfillment of the requirements for the degree of **Doctor of Philosophy**.

in

Geophysics

Department of Physics

Edmonton, Alberta
Fall 2004

Your file Votre référence
ISBN: 0-612-95971-6
Our file Notre référence
ISBN: 0-612-95971-6

Acknowledgements

The author wishes to express her sincere thanks to her academic supervisor, Dr. Mauricio D. Sacchi, for his guidance and encouragement during the period of this research.

I also want to thank members of my examining committee for their valuable suggestions on this thesis.

My gratitude go out to all the members of the SAIG group for all these years of intellectual support.

Special thanks are due to my husband, Xuqing Wu, for his unflinching support and understanding during the years of study.

Finally, I would like to thank my parents for their love and support and for always having confidence in me.

Contents

List of Figures

List of Tables

Chapter 1

Introduction

1.1 Overview of the problem and solutions

A seismic wavefield is a continuous multi-dimensional signal of time and space. Data recorded in a reflection seismic survey are the result of sampling a continuous wavefield at discrete spatial positions. The sampling theorem (Oppenheim et al., 1983) tells us that a continuous wavefield should be sampled at a rate greater than the Nyquist rate such that the continuous wavefield may be reconstructed from the sampled (recorded) wavefield. However, perfect wavefield sampling may never happen in the real world. Seismic data are always spatially incomplete to some degree since the receiver coverage is necessarily limited in areal extend. This incompleteness can be divided into three categories: lack of areal extent, sparse areal sampling, and irregular gaps in the recording array (Thorson, 1984). Cable length truncation is an example of the first category. The sparsity is often due to economical reasons. Field obstacles, dead traces, and cable feathering (particularly for marine surveys) can also result in irregular data gaps.

The incompleteness of the recorded wavefield creates problems for multi-channel processing steps such as suppression of coherent noise (multiples and ground roll), migration and inversion. Imaging for Amplitude Variation with Offset (AVO) or Amplitude Variation with Angle (AVA) analysis is an example where well sampled data are required in order to retrieve accurate estimates of AVO/AVA signatures. AVO or AVA techniques can be used for quantitative seismic discrimination of lithologies and fluids, therefore, they provide an additional interpretive dimension to seismic data analysis. In particular, they permit us to move beyond the traditional structural interpretation into technologies

capable of retrieving physical rock properties.

Since the early 1980s, the seismic exploration community started to use seismic amplitude analysis, namely AVO/AVA analysis, to estimate hydrocarbon indicators and to predict lithology. It has also become an essential tool in the hydrocarbon exploration industry to evaluate risk during exploration and development stages. AVO refers to the phenomena that amplitude of seismic reflections varies depending on the incidence angle and physical parameters above and below the reflecting interface. Equations used to describe this dependency become the models for AVA analysis, i.e., (Shuey, 1985). The name of AVO is often used instead of AVA since in very simple geological settings, offset (source-receiver distance) and angle of incidence are related by a simple equation (Castagna and Smith, 1994). Also, seismic data are collected directly at specified offsets not angles.

Conventionally, AVO/AVA analysis is applied to normal-moveout (NMO) corrected common midpoint panels (CMP). One pitfall of this approach is that NMO cannot handle structural dips and therefore, the AVO/AVA analysis could lead to erroneous interpretations (Resnick et al., 1986). To apply AVA techniques to the case where reflectors have dips or structural complexity, full prestack migration should be used to produce migrated data for AVA analysis.

As traditional migration for imaging structures, migration for AVO analysis can be implemented in a variety of ways. However, in general, formulations of migration for AVO analysis differ from the traditional migration in two important ways (Mosher et al., 1996). First, the migration is performed on prestack data and individual offset information is preserved in the output data. Rather than producing a single migrated section, the downward continued wavefield is kept as a prestack data volume. Second, it is essential to use an amplitude-preserving type of migration operator [1], otherwise AVO analysis is doomed to failure.

All migration algorithms require a properly sampled wavefield as the input to extrapolate into the subsurface wavefield. For example, Kirchhoff migration, based on high

[1]The migration must be capable of undoing all the amplitude distortions produced by wave propagation between sources and receivers. A migration method capable of undoing such distortions and thus producing angle-dependent reflection coefficient at analysis points in a lossless, isotropic, elastic earth is called a "true-amplitude migration" (Gray, 1997).

frequency asymptotic (ray) approximations, can produce both reflection coefficients and angle dependent reflectivity at any locations in the image. Therefore it can be used for AVO analysis in areas of moderate structural complexity (Tygel et al., 1999). Kirchhoff migration can be described as a process of summing through the discrete sampled data along the trajectories defined by travel times. It relies on the constructive and destructive interference of amplitudes migrated with a suite of restricted offset ranges to reproduce a correctly imaged reflector. If the spatial sampling is incomplete, Kirchhoff migration may produce unreliable amplitude responses. Fidelity of AVO analysis of prestack migrated gathers can, therefore, be severely compromised. Conventional solutions for dealing with sparse sampling are *flex binning* [2] and *normalization* (Zheng et al., 2001). For example, normalize each trace in an input CMP gather by the gather fold (number of traces contributing to the gather) before migration or normalize traces in a specified offset range by the fold within that range. The latter permits to balance the energy of each offset contribution. Normalization can also be applied after migration by what is known as the *hit count method* (Zheng et al., 2001). Canning and Gardner (1998) described the concept of *area weighting*, specifically for the case of common offset and common azimuth subsets of the data volume. However, simple binning and normalization schemes are often not sufficient to handle severely sparse data sets.

Wave equation migration method is another type of migration method based directly on the solution of the acoustic wave equation. It is well known for its capacity of being able to handle structural imaging in complex geological settings. Wave equation migration can be used to produce angle domain common image gathers that can be used for AVA analysis (de Bruin et al., 1990; Prucha et al., 1999; Mosher and Foster, 2000; Sava et al., 2001; Rickett, 2002; Sava and Fomel, 2003). Wave equation migration makes the assumption of the complete coverage of the recording geometry, missing data are often treated as zeros and the use of the incorrect wavefield can induce artifacts in migrated data and distort migrated amplitudes.

Though all direct migrations suffer from the incomplete sampling problem, least-squares migration can mitigate sampling artifacts by posing the imaging problem as an inverse problem and use a numerical approach to obtain a solution (Nemeth et al., 1999;

[2]Basically, this is a nearest neighbor interpolation scheme

Duquet et al., 2000; Kuehl and Sacchi, 2002; Kuehl, 2002; Kuehl and Sacchi, 2003). In least-squares migration, standard migration is regarded as the adjoint of a seismic modeling operator which is an approximation of the process that governs the wave propagation in the subsurface and it can be further modified to approximate the inverse operator. In particular, Nemeth et al. (1999) used Kirchhoff migration as the adjoint of the modeling operator. Duquet et al. (2000) developed a different regularization scheme where an offset smoothing constraint is used for least-squares common offset Kirchhoff migration. Kuehl and Sacchi (2002; 2003) proposed least-squares DSR (double square root) migration. The least-squares migration is constrained by a ray parameter dependent smoothing regularization that increases the robustness of the inversion. The constraint penalizes discontinuities and rapid amplitude changes that most likely stem from imaging artifacts and acquisition related noise.

In general, least-squares migration can reconstruct an image which can then be used to model well sampled data for AVO/AVA analysis. The disadvantage of this type of methods is that their implementations often involve iterative solutions of the linear equation, which can make them time-consuming. In addition, least-squares migration methods will fail if the velocity model used for the migration/de-migration operators is not known with sufficient detail.

A more popular strategy to deal with the problem of incomplete sampling is to regularize the survey by interpolating/extrapolating the recorded wavefield prior to migration. Reconstruction before migration will precondition the measured wavefield for the migration process. Thus preventing problems associated to data sampling.

Several interpolation/reconstruction schemes have been proposed. For example, one group of methods are based on continuation operators. In particular, shot continuation (Bagaini and Spagnolini, 1993; Mazzucchelli et al., 1998) and offset continuation (Bolondi et al., 1982; Ronen, 1987; Bagaini and Spagnoliniz, 1996; Fomel, 2003) can be used to predict missing shots or missing offsets using the specified velocity model. These methods suffer from irregularities in the input geometry. Inversion (Chemingui, 1999) can be used to deal with problems induced by irregular input geometries but in general this can lead to computational expensive procedures.

Coherent dip interpolation methods (Larner et al., 1981) search multi-channel data

for locally coherent dips and interpolate amplitudes linearly along those dip directions in the time-space domain. This family of methods do not handle multi-dips crossing events very well in the time-space domain. Pieprzak and McClean (1988) proposed a method that can deal with multi-dips, by involving an intelligent data adaptive procedure for picking dips in small overlapping spatio-temporal gates. Unfortunately, this approach to wavefield interpolation is prohibitively expensive for 3-D surveys. An automatic dip picking program is an obvious necessity for 3-D surveys where large amounts of data are acquired [3] (Pieprzak and McClean, 1988). However, an automatic search technique may provide misleading directions if noise is present (Spitz, 1991).

Another group of methods often used by industry are based on linear prediction. Spitz (1991) has introduced anti-alias f-x interpolation schemes with prediction filters. In f-x interpolation the underlying signal model is a superposition of complex sinusoids in the f-x domain; this is equivalent to a superposition of linear events in the t-x domain (Sacchi and Kuehl, 2001). Claerbout (1992) proposed a method to interpolate aliased data using 2-D prediction error filters in the t-x domain. Crawley et al. (1999) described a method to further improve the accuracy of the interpolation for non-stationary data, however, is relatively more expensive. A similar method can also be developed in the f-k domain (Gulunay and Chambers, 1996; Guo et al., 1996; Gulunay and Chambers, 1997). The advantage of applying trace interpolation in the Fourier domain is the efficiency of the fast Fourier transform (FFT) and the fact that the solution of linear equations that appears in f-x interpolation becomes complex division in the f-k domain (Gulunay, 2003). The above prediction error filter (PEF) type of interpolation methods are effective in dealing with aliased data since the information at low frequency is used to construct high frequencies. However, this is only possible if the data consists of a superposition of complex harmonics in the f-x domain. This limits the application of these methods to small spatio-temporal windows where the aforementioned assumption is satisfied.

The Radon transform can be used for trace interpolation. Lu (1985) used a semblance-scaled local slant stack to handle conflicting dips and to generate higher resolution output data. Kao (1997) applied a special slant stack and a novel iterative signal extraction scheme on traces in a small spatial window. The slant stack is modified to take advantage

[3] Typical 3-D survey involves processing data sets that can occupy several Terabytes of disk space!!

of the alias resisting property of α-trimmed mean. Yilmaz and Taner (1994) proposed a method where aliasing is suppressed by modifying the decomposed data (before inverse slant stacking) using fuzzy number theory. Hugonnet (1997) proposed to use a sparse Radon decomposition to attenuate spatial aliasing. The least-squares nonuniform Radon transform was used for trace interpolation by Schonewille and Duijndam (1998). Trad (2001) and Trad et al. (2002) proposed an interpolation method with high-resolution time-variant Radon transforms.

Fourier based interpolation methods make assumptions that the wavefield to be interpolated is spatially band limited. They have attractive computational properties but also have limitations with respect to regularizing aliased data. If the NMO velocity is known, the NMO process can be used to shrink the spatial bandwidth of the seismic wavefield before interpolation (Jakubowicz, 1994). The non-uniform FFT can be used to handle the irregular input geometry (Duijndam et al., 1999; Schonewille, 2000; Zwartjes and Duijndam, 2000). Zwartjes and Duijndam (2000) have proposed a Fourier reconstruction for sparse seismic data based on the high resolution Fourier transform proposed by Sacchi and Ulrych (1996) and Sacchi et al. (1998). In this method, the Fourier transform of the unknown sampled wavefield is retrieved via inversion. The inverted Fourier coefficients are used to perform the synthesis of data at new spatial positions. Liu and Sacchi (2001; 2003) have proposed a Fourier domain reconstruction method where band limited reconstruction is formulated as a minimum-norm least-squares type problem where an adaptive spectral weighted norm regularization term is used to constrain solutions. The method incorporates both bandwidth and spectrum shape of the data as a prior knowledge into the band limited data reconstruction problem , and often yields a better solution than the conventional band limited data reconstruction. The algorithm is implemented using a preconditioned conjugate gradients (CG) method and FFTs, thus, is very efficient tool to be used to interpolate large volumes of 3-D prestack data sets. In addition, computational efficiency allows the method to be easily expanded to a higher dimensional interpolation scheme. The multi-dimensional scheme has an advantage as it allows the method to exploit the multi-dimensional nature of the seismic wavefield for an optimal seismic data reconstruction.

1.2 Outline

This thesis starts with an introduction to the problem of sampling and signal reconstruction in problems of 1-D and multi-dimensional band limited signals. In particular, sampling and reconstruction issues of the multi-dimensional band limited seismic wavefield are discussed. In the Chapter 3, 1-D and multi-dimensional minimum weighted norm interpolation (MWNI) methods for seismic data reconstruction are presented in great details. In addition, the extension to 2-D and 3-D interpolation schemes is analyzed with real and simulated data.

In Chapter 4, 2-D/3-D wavefield MWNI schemes are applied to synthetic data to test its effectiveness for wave equation AVA imaging. In Chapter 5, two field data examples are presented where 3-D and 4-D MWNI methods are applied to real world problems. The first data set consists of a 3-D common azimuth prestack volume where 3 independent spatial coordinates are simultaneously interpolated. The second example, is a 3-D data prestack data volume with 4 independent spatial coordinates (2 midpoint and 2 offsets) or in other words a multi-azimuth interpolation.

Finally, Chapter 6 summarizes the main points of this thesis and suggests future research avenues to further improve the reconstruction of prestack seismic data.

Chapter 2

Band limited wavefield reconstruction

Geophysical signals are continuous functions of time and/or space. In the seismic experiment, a source of energy is used to generate waves that propagate into the earth's interior. Reflections, generated at geological interfaces, are recorded and processed to estimate a model of the subsurface. The recorded wavefield is the sampled version of the continuous wavefield. The sampled version has two meanings here. First, it indicates that the recorded wavefield is the discrete representation of the continuous wavefield. Second, it means that the recorded wavefield is always incomplete to some degree, due to, for example, the finite aperture of the receiver array and missing intermediate receivers. The sampling process, therefore, leads to two questions. Firstly, can the continuous wavefield be *properly* sampled in a way such that it can be fully reconstructed based on the discrete wavefield? Secondly, if the sampled wavefield is an incomplete sequence, can the full discrete wavefield be completely or partially reconstructed based on the available information?

The first question concerns the periodic sampling of a continuous signal. A problem well-studied by the seismic acquisition community. A detailed study can be found in Vermeer (1990). The answer to the question is well known, that is, it is possible to uniquely reconstruct a continuous signal from its samples if the continuous signal is band limited. Sections 2.1 and 2.2 provide a review of the sampling and reconstruction process for 1-D and multi-dimensional continuous band limited signals.

The second question concerns the discrete to discrete seismic data reconstruction

problem in which case the reconstruction can be posed as an inverse problem. The inverse problem is often ill-posed. In fact, other constraints besides the band limited assumption must be considered in order to obtain a unique and stable signal reconstruction (Jain and Ranganath, 1981). This problem is examined in Chapter 3.

2.1 Sampling and reconstruction of 1-D continuous signals

A discrete representation of a continuous-time[1] signal is typically obtained through periodic sampling [2]. The periodic sampling process can be mathematically represented by two stages (Oppenheim and Schafer, 1989). The first stage is to multiply the continuous function $x_c(t)$ by a periodic impulse train

$$s(t) = \sum_{n=-\infty}^{\infty} \delta(t - nT)\,, \tag{2.1.1}$$

where $\delta(t)$ is the unit impulse function and T is the sampling period. Consequently,

$$x_s(t) = x_c(t) \sum_{n=-\infty}^{\infty} \delta(t - nT) \tag{2.1.2}$$

$$= \sum_{n=-\infty}^{\infty} x_c(nT)\delta(t - nT)\,. \tag{2.1.3}$$

The resulting signal $x_s(t)$ is a continuous signal, but it only has non-zeros values at integer multiples of T. The latter can be converted to a discrete sequence, $x(n)$, indexed by the integer temporal sample n:

$$x(n) = x_c(nT)\,, \quad -\infty < n < \infty\,. \tag{2.1.4}$$

The periodic sampling process is depicted in Figure 2.1.

We denote $X_c(\Omega)$ the continuous Fourier transform of $x_c(t)$ defined by:

$$X_c(\Omega) = \int_{-\infty}^{\infty} x_c(t)e^{-j\Omega t}dt\,, \tag{2.1.5}$$

[1]Continuous-time signals (hereafter referred to as continuous signals) are defined for a continuous independent variable.

[2]The same analysis is valid for spatial signals.

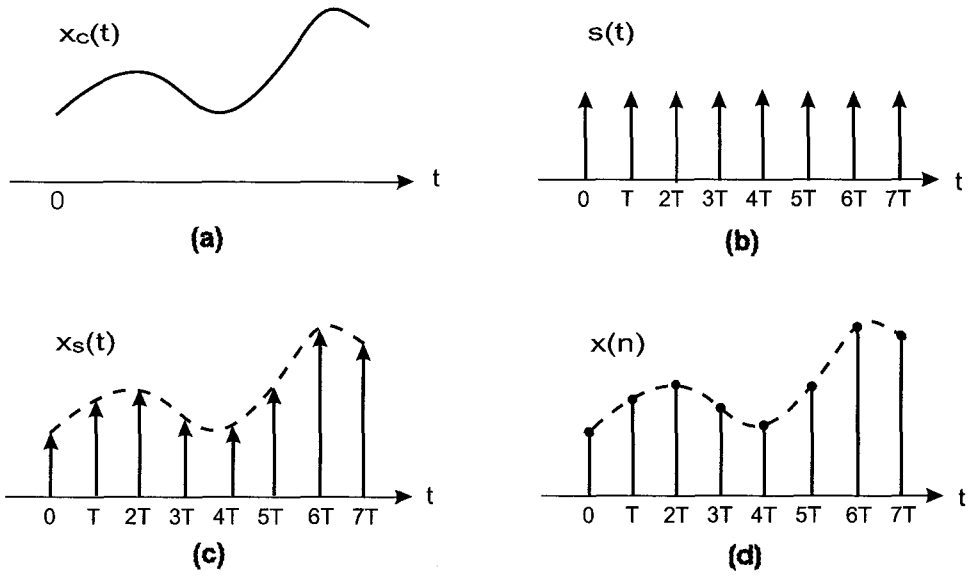

Figure 2.1: The periodic sampling process of a 1-D continuous signal. (a) A continuous signal $x_c(t)$. (b) Periodic impulse train $s(t)$. (c) The signal $x_s(t)$. (d) The discrete sequence $x(n)$.

and, the inverse Fourier transform:

$$x_c(t) = \frac{1}{2\pi}\int_{-\infty}^{\infty} X_c(\Omega)e^{j\Omega t}d\Omega\,. \tag{2.1.6}$$

The Fourier transform of the periodic impulse train $s(t)$ is also a periodic impulse train (Oppenheim et al., 1983):

$$S(\Omega) = \frac{2\pi}{T}\sum_{k=-\infty}^{\infty}\delta(\Omega - k\Omega_s) \tag{2.1.7}$$

where $\Omega_s = 2\pi/T$ is the sampling frequency in radian per second. Therefore, the Fourier transform of $x_s(t)$ can be represented as

$$X_s(\Omega) = \frac{1}{2\pi} X_c(\Omega) * S(\Omega) \tag{2.1.8}$$

$$= \frac{1}{2\pi} \int_{-\infty}^{\infty} X_c(\Omega - \tau) \frac{2\pi}{T} \sum_{k=-\infty}^{\infty} \delta(\tau - k\Omega_s) d\tau$$

$$= \frac{1}{T} \sum_{k=-\infty}^{\infty} \int_{-\infty}^{\infty} X_c(\Omega - \tau) \delta(\tau - k\Omega_s) d\tau$$

$$= \frac{1}{T} \sum_{k=-\infty}^{\infty} X_c(\Omega - k\Omega_s) \tag{2.1.9}$$

where the symbol $*$ is used to denote convolution. We now define $X(\omega)$, the discrete Fourier transform of the sequence $x(n)$,

$$X(\omega) = \sum_{n=-\infty}^{\infty} x(n) e^{-j\omega n} . \tag{2.1.10}$$

The inverse discrete-time Fourier transform is given by

$$x(n) = \frac{1}{2\pi} \int_{2\pi} X(\omega) e^{j\omega n} . \tag{2.1.11}$$

It can be shown that

$$X_s(\Omega) = X(\omega)|_{\omega=\Omega T} . \tag{2.1.12}$$

Consequently, from equation (2.1.12) and (2.1.9) we can arrive to the following expression:

$$X(\omega) = \frac{1}{T} \sum_{k=-\infty}^{\infty} X_c(\frac{\omega}{T} - \frac{2\pi k}{T}) . \tag{2.1.13}$$

Equation (2.1.9) shows that the Fourier transform of the sampled data is produced by superimposing copies of $X_c(\Omega)$ that are shifted by integer multiples of the sampling frequency Ω_s. Figure 2.2 depicts the frequency-domain representation of the sampling operator. Figure 2.2a shows a continuous signal $x_c(t)$. Figure 2.2b represents the spectrum of the continuous signal $x_c(t)$ that is band limited to the interval $-\Omega_N$ to Ω_N. Figure 2.2c shows the spectrum of the periodic sampling operator with sampling frequency $\Omega_s = 2\pi/T_1 > 2\Omega_N$, and Figure 2.2d shows the spectrum of the sampled signal.

The spectrum of another periodic sampling operator, but now with sampling frequency $\Omega_s = 2\pi/T_2 < 2\Omega_N$, is shown in Figure 2.2e. Figure 2.2f shows the spectrum of the sampled signal obtained with the second periodic sampling operator. Note that when the bandwidth of the signal Ω_N is less than one half the sampling frequency Ω_s, each spectral replica is separated by Ω_s and no overlap occurs as illustrated in Figure2.2d . Therefore, the original continuous signal can be recovered from the sampled signal with an ideal low-pass filter. If the bandwidth of the signal is greater than one half the sampling frequency Ω_s, the spectra of the replications are mixed together as illustrated in Figure 2.2f. In this case, the sampled version of the signal contains frequencies, which are commonly referred as *aliases*, that are not present in the original signal. Moreover, the original continuous signal can no longer be recovered exactly by a low-pass filtering operation.

This leads to the Shannon or Nyquist Sampling Theorem which states that for a band limited signal with maximum frequency Ω_N, the sampling frequency Ω_s must be greater than twice the maximum frequency, i.e.,

$$\Omega_s > 2\Omega_N \tag{2.1.14}$$

in order to have the signal reconstructed without aliasing. The frequency Ω_N is commonly referred as the Nyquist sampling frequency, and the frequency $2\Omega_N$ is called Nyquist rate.

If a continuous signal is sampled correctly according to the sampling theorem, it can be reconstructed perfectly from its samples. The perfect reconstruction can also be thought of as a two-step process. First, the discrete samples are converted into a continuous signal. Given a sequence of sample $x(n)$, a weighted impulse train $x_s(t)$ can be formed in which the n-th sample is associated with the impulse train at $t = nT$:

$$x_s(t) = \sum_{n=-\infty}^{\infty} x(n)\delta(t - nT)\,. \tag{2.1.15}$$

Then the weighted impulse train $x_s(t)$ is filtered through an ideal low-pass filter with cutoff frequency π/T,

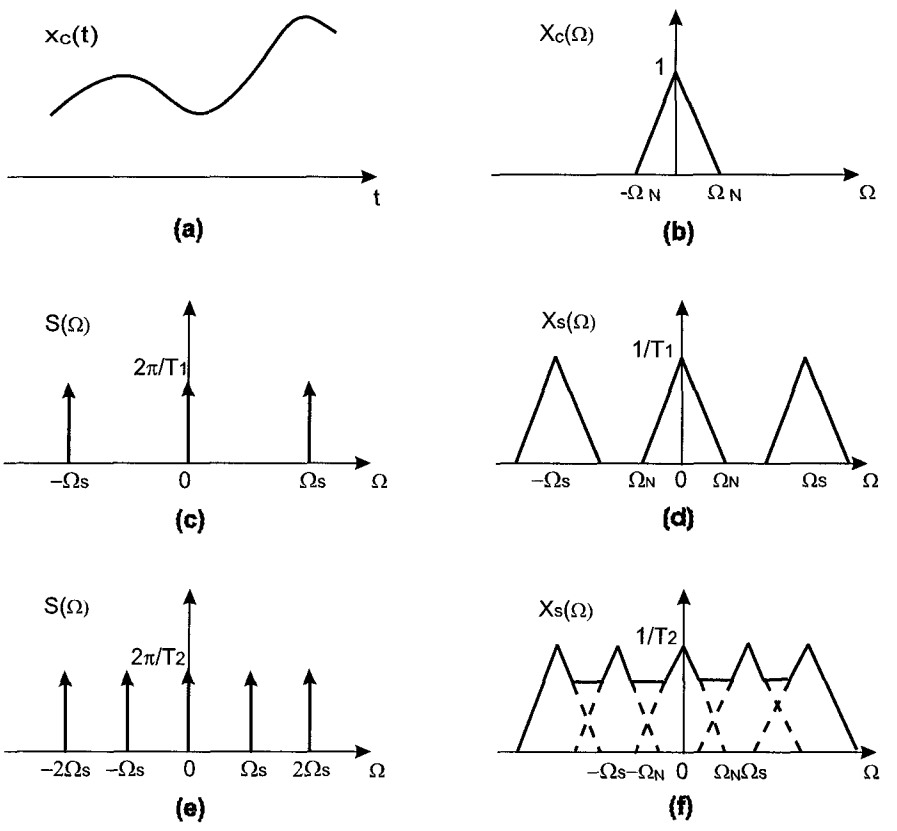

Figure 2.2: The frequency-domain representation of the periodic sampling operator. (a) A continuous-time signal $x_c(t)$. (b) The spectrum of the continuous-time signal that is band limited to the interval $-\Omega_N$ to Ω_N. (c) The spectrum of a periodic sampling function with the sampling frequency $\Omega_s = 2\pi/T_1 > 2\Omega_N$. (d) The spectrum of the result of sampling using the sampling function as shown in (c). (e) The spectrum of another periodic sampling function with the sampling frequency $\Omega_s = 2\pi/T_2 < 2\Omega_N$. (f) The spectrum of the result of sampling using the sampling function as shown in (e).

$$H(\Omega) = \begin{cases} T, & |\Omega| < \pi/T \\ 0, & \text{otherwise} \end{cases} \tag{2.1.16}$$

such that the Fourier transform of the filter output will be identical to the Fourier transform of the original continuous signal $x_c(t)$. Note the filter has a gain T that needs to compensate with the factor $1/T$ in equation (2.1.9). The corresponding impulse response is the inverse Fourier transform of $H(\Omega)$:

$$h(t) = T/2\pi \int_{-\pi/T}^{\pi/T} e^{j\Omega t} d\Omega \tag{2.1.17}$$

$$= \frac{sin(\pi t/T)}{\pi t/T} \tag{2.1.18}$$

$$= \text{sinc}(\frac{t}{T}) . \tag{2.1.19}$$

This two-step procedure therefore can be described mathematically as

$$x_r(t) = \sum_{n=-\infty}^{\infty} x(n) \frac{sin[\pi(t-nT)/T]}{\pi(t-nT)/T} \tag{2.1.20}$$

$$= \sum_{n=-\infty}^{\infty} x(n) \text{sinc}(\frac{t-nT}{T}) , \tag{2.1.21}$$

where $x_r(t)$ is the recovered continuous signal. In general, the continuous signal can be reconstructed exactly from $x_s(t)$ by means of a low-pass filter with gain T and a cutoff frequency Ω_c greater than Ω_N and less than $\Omega_s - \Omega_N$. In this case, the impulse response is given by

$$h(t) = T\frac{\Omega_c}{\pi} \text{sinc}(\frac{\Omega_c t}{\pi}) , \tag{2.1.22}$$

so that

$$x_r(t) = \sum_{n=-\infty}^{\infty} x(n) T \frac{\Omega_c}{\pi} \text{sinc}[\frac{\Omega_c(t-nT)}{\pi}] . \tag{2.1.23}$$

Using equation (2.1.23), band limited continuous signals can be reconstructed from their samples using a linear combination of *sinc* functions, where the *sinc* functions are weighted by sample values. Interpolation using the *sinc* function as in equation (2.1.23) is commonly referred to as band limited interpolation, since it implements an exact reconstruction if $x(t)$ is band limited and the sampling frequency satisfies the conditions of the sampling theorem (Oppenheim et al., 1983).

An extension to the above reconstruction process is resampling. Consider the process where a continuous signal x_c has been sampled at a rate of $\Omega_{\text{old}} = 1/T_{\text{old}}$, and discrete samples are $x_{\text{old}}(n) = x_c(nT_{\text{old}})$. The discrete-time band limited signal $x(n)$ can be resampled to change its effective sampling rate. The sampling rate can be decreased or

increased. Decreasing the sampling rate is known as decimation. The original sampling rate can be decimated or downsampled by a integer factor of N_D by retaining the N_Dth samples and discarding the remaining samples. Relative to the original sample rate, Ω_{old}, the new sample rate is

$$\Omega_{new} = \frac{\Omega_{old}}{N_D}. \tag{2.1.24}$$

An example of decimation of a sequence by a factor of $N_D = 2$ is illustrated in Figure 2.3. Figure 2.3a shows the discrete replicated spectrum of $x_{old}(n)$, $X_{old}(\omega)$. The spectrum of the decimated data $X_{new}(\omega)$ is shown in Figure 2.3b. Note that $X_{old}(\omega)$ could have been obtained directly from sampling the continuous signal at a new sampling rate. In addition, there is a limit to the amount of decimation that can be performed relative to the bandwidth of the original signal. Figure 2.3c shows an example where the new sampling rate after decimation will result in the aliased spectrum. Therefore, a low-pass filter (shaded area) needs to be applied before decimation. Figure 2.3d shows the resulting alias-free spectrum after decimation with the low-pass filter. It is clear that high frequency components can be lost during the decimation process.

Increasing the sampling rate is often called interpolation. To increase a given sample rate or upsample by a factor of N_U, zeros must be inserted between each sample x_{old} by a factor of N_U to create a new sequence $x'_{new}(n')$ where

$$x'_{new}(n') = x_{old}(n), \quad \text{when } n' = N_U n. \tag{2.1.25}$$

An example of upsampling by a factor of $N_U = 2$ is depicted in Figure 2.4. Figure 2.4a and 2.4b show the original sequence $x_{old}(n)$ and its spectrum $X_{old}(\omega)$. Figure 2.4c is the new sequence $x'_{new}(n')$ obtained by inserting zeros between each sample of $x_{old}(n)$. The spectrum of $x'_{new}(n)$, $X'_{new}(\omega)$ is shown in Figure 2.4d. Note that the spectrum of the zero-padded sequence $X'_{new}(\omega)$ is two times the replication of the spectrum of the original sequence since the effective sampling frequency Ω_{new} is increased and the spectrum of x_{old} was already replicated 2 times between 0 radian/second and Ω_{new}. The final step is to apply a low-pass filter (shaded area) to $X'_{new}(\omega)$ to simulating the new folding (sampling) frequency. The resulting spectrum $X_{new}(\omega)$ and sequence $x_{new}(n)$ are shown

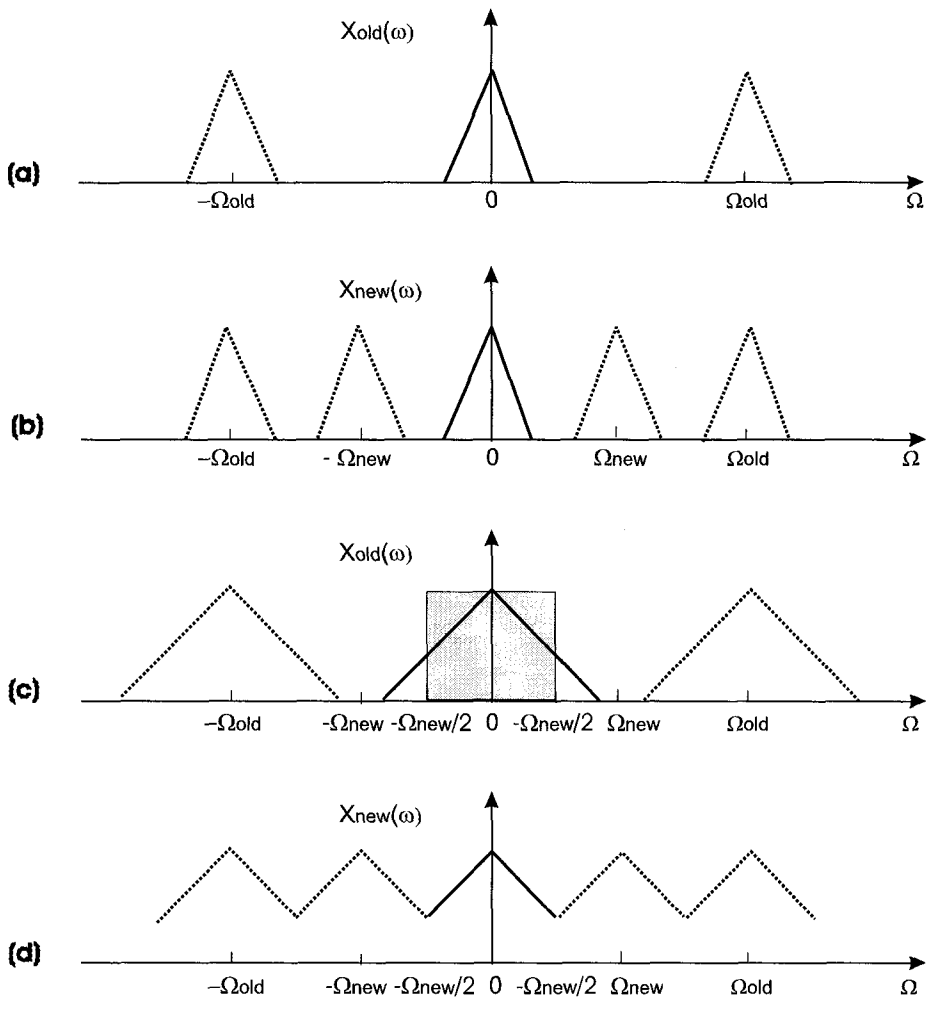

Figure 2.3: Decimation by a factor of two. (a) Spectrum and replications of the original sequence. (b) Spectrum of the sequence decimated by a factor of 2. (c) An example where low-pass (shaded area) filtering is needed before decimation to avoid aliasing. (d) Spectrum of the alias-free decimated signal.

in Figure 2.4f and 2.4e, respectively.

Note that the interpolation and decimation processes discussed above are valid for changing the sampling rate by an integer factor. It is important to stress, however, that by using combined interpolation and decimation processes, the sampling rate can be changed by a non-integer factor (Lyons, 1997).

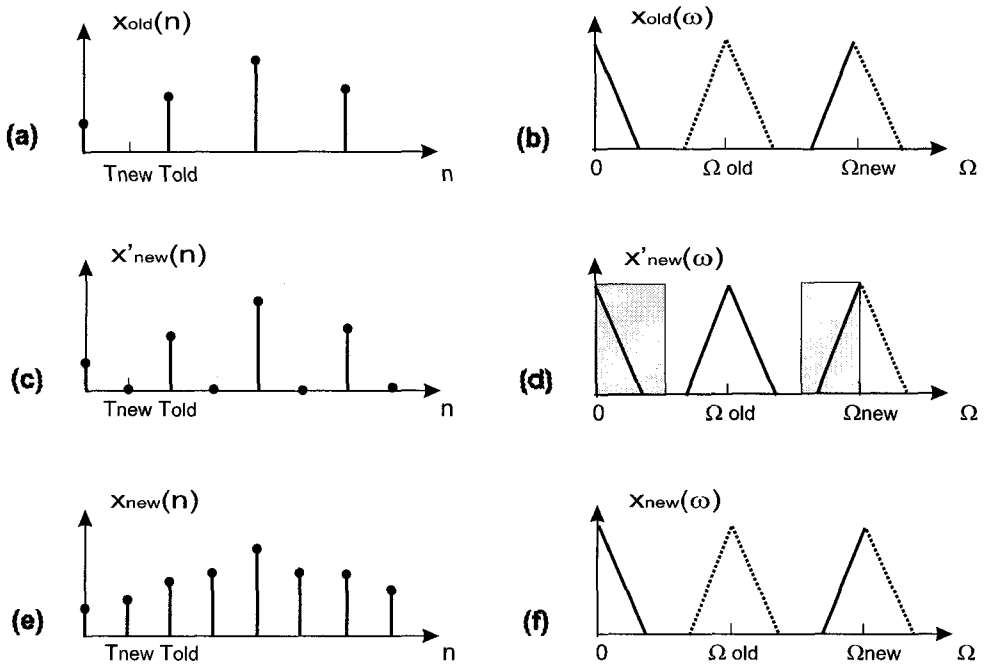

Figure 2.4: Interpolation by a factor of two. (a) The original sequence. (b) Spectrum and replications of the original sequence. (c) The new sequence obtained after zero padding. (d) Spectrum of the zero-padded sequence. (e) The interpolated sequence. (f) Spectrum of the interpolated sequence obtained by low-pass (shaded area) filtering the spectrum shown in (d).

2.2 Sampling and reconstruction of multi-dimensional signals

A multi-dimensional signal can be modeled as a function of $M \geq 2$ independent variables. Many theoretical results discussed in this section can be viewed as a straightforward extensions of the 1-D case discussed in section 2.1. However, there are many other important issues that do not appear in the 1-D case (Dudgeon and Mersereau, 1984). For simplicity, the sampling and reconstruction problems for 2-D signals are discussed; a generalization to higher dimensions is straightforward.

2.2.1 Periodic sampling with rectangular geometry

Analogous to the 1-D case, a 2-D discrete sequence can be obtained through periodic sampling of the 2-D continuous signal. If we assume periodic sampling with rectangular

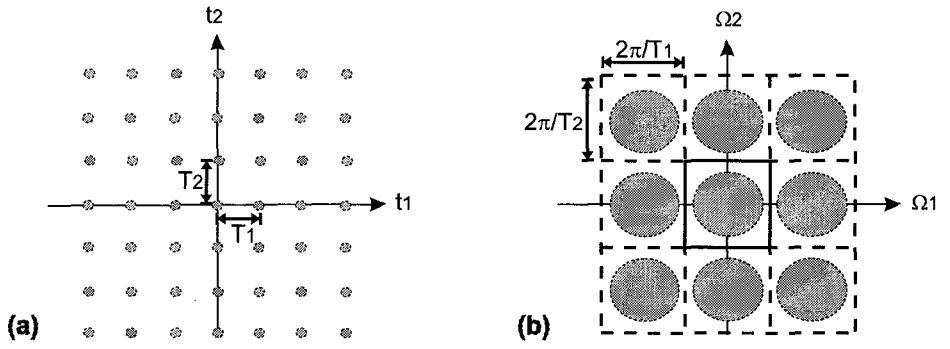

Figure 2.5: Periodic sampling of a 2-D continuous signal with rectangular geometry. (a) Sampling locations on the 2-D plane. (b) Replication of the original spectrum after periodic sampling.

geometry, we need to multiply the continuous signal $x_c(t_1, t_2)$ by a 2-D periodic impulse train of the form:

$$s(t_1, t_2) = \sum_{n_2=-\infty}^{\infty} \sum_{n_1=-\infty}^{\infty} \delta(t_1 - n_1 T_1, t_2 - n_2 T_2)\,,$$

where $\delta(t_1, t_2)$ is the 2-D unit impulse function and T_1 and T_2 indicate the horizontal and vertical sampling intervals. The 2-D sampled signal is now given by

$$x_s(t_1, t_2) = x_c(t_1, t_2) \sum_{n_2=-\infty}^{\infty} \sum_{n_1=-\infty}^{\infty} \delta(t_1 - n_1 T_1, t_2 - n_2 T_2) \tag{2.2.1}$$

$$= \sum_{n_2=-\infty}^{\infty} \sum_{n_1=-\infty}^{\infty} x_c(n_1 T_1, n_2 T_2)\, \delta(t_1 - n_1 T_1, t_2 - n_2 T_2)\,. \tag{2.2.2}$$

The result of applying the periodic sampling operator to the continuous signal is $x_s(t)$. The latter can be converted to a discrete 2-D sequence $x(n_1, n_2)$

$$x(n_1, n_2) = x_c(n_1 T_1, n_2 T_2)\,, \quad -\infty < n1, n2 < \infty\,. \tag{2.2.3}$$

The sampling grid for this particular problem is depicted in Figure 2.5a.
Now, we define the 2-D Fourier transform of the continuous signal as:

$$X_c(\Omega_1, \Omega_2) = \int_{-\infty}^{\infty}\int_{-\infty}^{\infty} x_c(t_1, t_2)\exp(-j\Omega_1 t_1 - j\Omega_2 t_2)dt_1 dt_2 \,. \tag{2.2.4}$$

in addition, the 2-D inverse Fourier transform is given by

$$x_c(t_1, t_2) = \frac{1}{2\pi}\int_{-\infty}^{\infty}\int_{-\infty}^{\infty} X_c(\Omega_1, \Omega_2)\exp(j\Omega_1 t_1 + j\Omega_2 t_2)d\Omega_1 d\Omega_2 \,. \tag{2.2.5}$$

The 2-D Fourier transform of the 2-D periodic impulse train is

$$S(\Omega_1, \Omega_2) = \Omega_{s1}\Omega_{s2}\sum_{k_2=-\infty}^{\infty}\sum_{k_1=-\infty}^{\infty}\delta(\Omega_1 - k_1\Omega_{s1}, \Omega_2 - k_2\Omega_{s2}) \tag{2.2.6}$$

where $\Omega_{s1} = 2\pi/T_1$ and $\Omega_{s2} = 2\pi/T_2$ are horizontal and vertical sampling frequencies. The Fourier transform of $x_s(t_1, t_2)$ can be written as a convolution of $X_c(\Omega_1, \Omega_2)$ with $S(\Omega_1, \Omega_2)$. Consequently,

$$X_s(\Omega_1, \Omega_2) = \frac{1}{T_1}\frac{1}{T_2}\sum_{k_2=-\infty}^{\infty}\sum_{k_1=-\infty}^{\infty} X_c(\Omega_1 - k_1\Omega_{s1}, \Omega_2 - k_2\Omega_{s2}) \,. \tag{2.2.7}$$

We now write down the Fourier transform of the discrete signal:

$$X(\omega_1, \omega_2) = \sum_{n_2=-\infty}^{\infty}\sum_{n_1=-\infty}^{\infty} x(n_1, n_2)\exp(-j\omega_1 n_1 - j\omega_2 n_2) \,. \tag{2.2.8}$$

It can be shown that

$$X_s(\Omega_1, \Omega_2) = X(\omega_1, \omega_2)|_{\omega_1=\Omega_1 T_1, \omega_2=\Omega_2 T_2} \,. \tag{2.2.9}$$

Substituting equation (2.2.9) into (2.2.7) results in

$$X(\omega_1, \omega_2) = \frac{1}{T_1}\frac{1}{T_2}\sum_{k_2=-\infty}^{\infty}\sum_{k_1=-\infty}^{\infty} X_c(\frac{\omega_1 - 2\pi k_1}{T_1}, \frac{\omega_2 - 2\pi k_2}{T_2}) \,. \tag{2.2.10}$$

Equation (2.2.7) shows that 2-D rectangular sampling of a continues signal, yields a discrete signal with a Fourier spectrum that is a periodic extension of the spectrum of the continuous signal. This is illustrated in Figure 2.5b where the continuous signal is band limited:

$$X_c(\Omega_1, \Omega_2) = 0 \quad \text{for} \quad |\Omega_{N1}| \geq \frac{\pi}{T_1}, |\Omega_{N2}| \geq \frac{\pi}{T_2} \,. \tag{2.2.11}$$

The band limited spectrum is replicated by the sampling frequencies. Note that when the bandwidth of the signal is less than half the sampling frequency, each replicated spectrum is separated by horizontal and vertical sampling frequencies without overlap. Consequently, it is possible in this case to recover the continuous signal from the discrete signal. This leads to the 2-D sampling theorem which states that a band limited continuous signal may be reconstructed from its sample values if the sampling periods T_1 and T_2 are small enough to ensure that the condition given by expression (2.2.11) is true.

To demonstrate this, first, the discrete signal is converted into a weighted 2-D impulse train

$$x_s(t_1, t_2) = \sum_{n_2=-\infty}^{\infty} \sum_{n_1=-\infty}^{\infty} x(n_1, n_2)\delta(t_1 - n_1T_1, t_2 - n_2T_2)\,. \tag{2.2.12}$$

Then, $x_s(t_1, t_2)$ is filtered through a 2-D ideal low-pass filter, e.g. with cutoff frequencies at half the sampling frequency:

$$H(\Omega_1, \Omega_2) = \begin{cases} T_1T_2, & |\Omega_1| < \pi/T_1,\ |\Omega_2| < \pi/T_2 \\ 0, & \text{otherwise} \end{cases}\,. \tag{2.2.13}$$

Note that the filter has a gain of $T_1\,T_2$ to compensate for the factor $1/(T_1\,T_2)$ in equation (2.2.7). The filtering process can be done by convolving $x_s(t_1, t_2)$ with the inverse Fourier transform of the low-pass filter:

$$h(t_1, t_2) = \frac{T_1T_2}{4\pi^2} \int_{-\infty}^{\infty} \int_{-\infty}^{\infty} \exp(-j\Omega_1t_1 - j\Omega_2t_2)dt_1dt_2 \tag{2.2.14}$$

$$= \frac{sin(\pi t_1/T_1)}{\pi t_1/T_1} \frac{sin(\pi t_2/T_2)}{\pi t_2/T_2} \tag{2.2.15}$$

$$= \text{sinc}(\frac{t_1}{T_1})\text{sinc}(\frac{t_2}{T_2})\,. \tag{2.2.16}$$

Finally, the reconstructed signal $x_r(t_1, t_2)$ can be expressed in terms of $x(n_1, n_2)$:

$$x_r(t_1, t_2) = \sum_{n_2=-\infty}^{\infty} \sum_{n_1=-\infty}^{\infty} x(n_1, n_2)\text{sinc}(\frac{t_1 - n_1T_1}{T_1})\text{sinc}(\frac{t_2 - n_2T_2}{T_2})\,. \tag{2.2.17}$$

In general, the 2-D low-pass filter can be chosen with the cutoff frequency Ω_{c1} greater than Ω_{N1} and less than $\Omega_{s1} - \Omega_{N1}$, Ω_{c2} greater than Ω_{N2} and less than $\Omega_{s2} - \Omega_{N2}$, in which case, the filter impulse response can be written as

$$h(t_1, t_2) = T_1 T_2 \frac{\Omega_{c1}\Omega_{c2}}{\pi^2} \text{sinc}(\frac{\Omega_{c1} t_1}{\pi}) \text{sinc}(\frac{\Omega_{c2} t_2}{\pi}), \tag{2.2.18}$$

and the reconstructed signal can be expressed as

$$x_r(t_1, t_2) = \sum_{n_2=-\infty}^{\infty} \sum_{n_1=-\infty}^{\infty} x(n_1, n_2) T_1 T_2 \frac{\Omega_{c1}\Omega_{c2}}{\pi^2} \text{sinc}[\frac{\Omega_{c1}(t_1 - n_1 T_1)}{\pi}] \text{sinc}[\frac{\Omega_{c2}(t_2 - n_2 T_2)}{\pi}]. \tag{2.2.19}$$

Note that if the sampling condition (2.2.11) is not satisfied, aliasing will occur: replicas of $X(\Omega_1, \Omega_2)$ in the periodic extension in (2.2.7) will fold into the region $|\Omega_1 T_1| < \pi$, $|\Omega_2 T_2| < \pi$. In this case, of course, exact (continuous) signals can not be recovered via the reconstruction scheme given by equation (2.2.19).

2.2.2 Periodic sampling with arbitrary sampling geometries

Periodic sampling can be defined with arbitrary sampling geometries. A detailed derivation of periodic sampling of a 2-D continuous signal with arbitrary sampling geometries is given by Dudgeon and Mersereau (1984).

In general, if we define two linearly independent vectors $\mathbf{v}_1 = (v_{11}, v_{12})'$ and $\mathbf{v}_2 = (v_{12}, v_{22})'$, the locations of a doubly periodic set of samples in the (t_1, t_2)-plane can be written as

$$\begin{aligned} t_1 &= v_{11} n_1 + v_{12} n_2 \\ t_2 &= v_{21} n_1 + v_{22} n_2 \end{aligned}. \tag{2.2.20}$$

Using matrix-vector notation, the above equation can be written as

$$\mathbf{t} = \underset{\sim}{\mathbf{V}} \mathbf{n} \tag{2.2.21}$$

where $\underset{\sim}{\mathbf{V}} = [\mathbf{v1}\ \mathbf{v2}]$ is a full rank linear operator and is referred to as the sampling matrix. Discrete samples of a continuous signal can be obtained with periodic sampling with the sampling matrix $\underset{\sim}{\mathbf{V}}$ such that

$$x(\mathbf{n}) = x_c(\underset{\sim}{\mathbf{V}} \mathbf{n}). \tag{2.2.22}$$

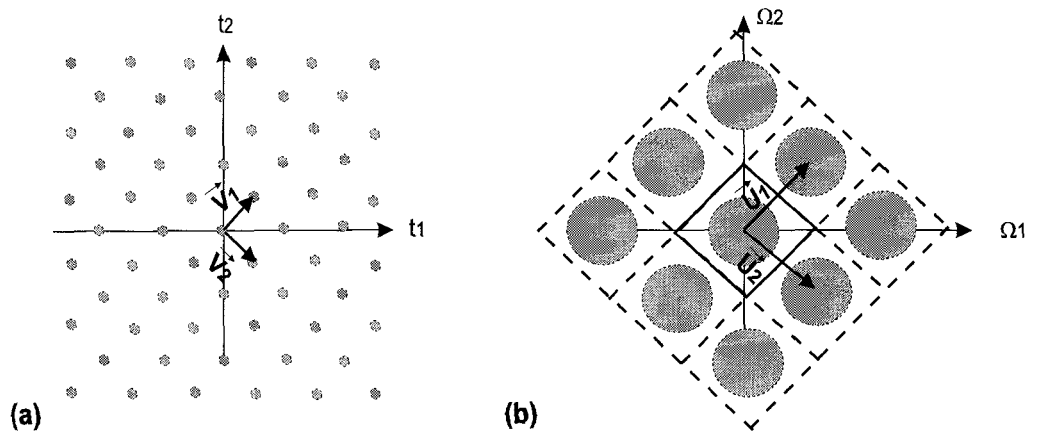

Figure 2.6: Periodic sampling of a 2-D continuous signal with arbitrary geometry. (a) Sampling locations in the (t_1, t_2)-plane determined by the vectors $\mathbf{v}_1$ and $\mathbf{v}_2$ which comprise the sampling matrix $\underset{\sim}{\mathbf{V}}$. (b) Replications of the original spectrum after the periodic sampling.

An example showing the sampling locations in the (t_1, t_2)-plane is provided in Figure 2.6a.

We now define the Fourier transform of a continuous signal x_c in a vector form as

$$X_c(\mathbf{\Omega}) = \int_{-\infty}^{\infty} x_c(\mathbf{t}) \exp(-j\mathbf{\Omega}'\mathbf{t}) d\mathbf{t} \tag{2.2.23}$$

and, similarly, the discrete Fourier transform as

$$X(\boldsymbol{\omega}) = \sum_{\mathbf{n}} x(\mathbf{n}) \exp(-j\boldsymbol{\omega}'\mathbf{n}). \tag{2.2.24}$$

Let $\boldsymbol{\omega} = \underset{\sim}{\mathbf{V}}'\mathbf{\Omega}$, it can be shown (Dudgeon and Mersereau, 1984) that the sampled signal has a spectrum that is the periodic extension of the original spectrum:

$$X(\boldsymbol{\omega}) = \frac{1}{|\det \underset{\sim}{\mathbf{V}}|} \sum_{\mathbf{k}} X_c(\underset{\sim}{\mathbf{V}}'^{-1}(\boldsymbol{\omega} - 2\pi\mathbf{k})) . \tag{2.2.25}$$

or, alternatively

$$X(\underset{\sim}{\mathbf{V}}'\mathbf{\Omega}) = \frac{1}{|\det \underset{\sim}{\mathbf{V}}|} \sum_{\mathbf{k}} X_c(\mathbf{\Omega} - \underset{\sim}{\mathbf{U}}\mathbf{k}) \tag{2.2.26}$$

where $\underset{\sim}{\mathbf{U}}$ is a matrix that satisfies

$$\underset{\sim}{\mathbf{U}}'\underset{\sim}{\mathbf{V}} = 2\pi\underset{\sim}{\mathbf{I}} \tag{2.2.27}$$

and $\underset{\sim}{\mathbf{I}}$ is a 2×2 identity matrix. Note in this case, the periodicity in the Fourier domain is described by the general matrix $\underset{\sim}{\mathbf{U}}$, which can be thought of as a set of two periodic vectors $\mathbf{u_1}$ and $\mathbf{u_2}$ representing the two independent directions in which $X_c(\mathbf{\Omega})$ will replicate. This is illustrated in Figure 2.6b.

At this point, consider the continuous signal $x_c(\mathbf{t})$ band limited to a band $\mathcal{B}$. If there is no aliasing, equation (2.2.26) becomes

$$X(\underset{\sim}{\mathbf{V}}'\mathbf{\Omega}) = \frac{1}{|\det \underset{\sim}{\mathbf{V}}|} X_c(\mathbf{\Omega}) \tag{2.2.28}$$

for values of $\underset{\sim}{\mathbf{V}}'\mathbf{\Omega}$ lying in the square centered on the origin with sides of length 2π. Therefore, $X_c(\mathbf{\Omega})$ can be recovered from the $X(\underset{\sim}{\mathbf{V}}'\mathbf{\Omega})$ and consequently, the band limited continuous signal $x_c(\mathbf{t})$ can be recovered from the sampled sequence $x(\mathbf{n})$. In this case, equation (2.2.28) can be rearranged as

$$X_c(\mathbf{\Omega}) = \begin{cases} |\det \underset{\sim}{\mathbf{V}}| \cdot X(\underset{\sim}{\mathbf{V}}'\mathbf{\Omega}) & \Omega \in \mathcal{B} \\ 0 & \text{otherwise} \end{cases} . \tag{2.2.29}$$

By taking the inverse Fourier transform of both sides of equation (2.2.29) and expressing $X(\underset{\sim}{\mathbf{V}}'\mathbf{\Omega})$ in terms of the sample values $x(n_1, n_2)$, it can be shown that the continuous signal is recovered through the following equation:

$$x_c(\mathbf{t}) = \sum_{\mathbf{n}} x(\mathbf{n}) f(\mathbf{t} - \underset{\sim}{\mathbf{V}}\mathbf{n}) \tag{2.2.30}$$

where

$$f(\mathbf{t}) = \frac{|\det \underset{\sim}{\mathbf{V}}|}{4\pi^2} \int_{\mathcal{B}} \exp(j\mathbf{\Omega}'\mathbf{t}) d\mathbf{\Omega} \tag{2.2.31}$$

is the interpolation function that allows the reconstruction of values of $x_c(\mathbf{t})$ at the points in between the sample locations given by $\mathbf{t} = \underset{\sim}{\mathbf{V}}\mathbf{n}$.

Note that to avoid aliasing $\underset{\sim}{\mathbf{U}}$ should be chosen so that there is no overlap among the replicated versions of $X_c(\Omega)$. The choice of $\underset{\sim}{\mathbf{U}}$ determines the sampling matrix $\underset{\sim}{\mathbf{V}}$ through equation (2.2.27). In general, $\underset{\sim}{\mathbf{U}}$ is not unique and this allows any band limited signal to

be represented with several sampling geometries. However, it is often desirable to use a minimal sampling set for efficient sampling. It can be shown that the density of samples per unit area is given by $1/|\det \mathbf{V}|$. Minimizing this quantity is equivalent to minimizing $|\det \mathbf{U}|$. Consequently, the most efficient sampling scheme for a band limited signal is to choose the periodicity matrix $\mathbf{U}$ which has the smallest value of $|\det \mathbf{U}|$ and which avoids aliasing for the particular shape of the signal's baseband $\mathcal{B}$.

Rectangular sampling and hexagonal sampling are two commonly used sampling strategies. The rectangular sampling strategy has been discussed in section 2.2.1. The details of the hexagonal sampling are discussed by Dudgeon and Mersereau (1984) and Hindriks and Duijndam (2000). Hexagonal sampling poses advantage over the rectangular sampling. It can be shown (Petersen and Middleton, 1962) that there is no more efficient sampling scheme for circularly band limited signals than hexagonal sampling.

2.3 Continuous seismic wavefield sampling and reconstruction

Seismic wavefields are a multi-dimensional continuous signal of time and space. Therefore, the sampling process discussed in section 2.1 and 2.2 can be applied to the seismic wavefield sampling problem. In this section, some of properties of the continuous seismic wavefield are first reviewed. Then, sampling matrices are derived to describe the 2-D seismic wavefield sampling in the shot-receiver and midpoint-offset domain. Finally, the reconstruction of the continuous wavefield is briefly discussed.

2.3.1 Properties of the continuous seismic wavefield

Coordinate transformation

The continuous seismic wavefield can be denoted as $w(t, \mathbf{x}_s, \mathbf{x}_r)$, where $\mathbf{x}_s$ represents the shot vector (x_s, y_s) and $\mathbf{x}_r$ represents the receiver vector (x_r, y_r). Alternatively, it can be described in terms of the midpoint vector $\mathbf{x}_m(x_m, y_m)$ and the offset vector $\mathbf{x}_o(x_o, y_o)$, i.e., $w(t, \mathbf{x}_m, \mathbf{x}_o)$, via the following linear coordinate transformation

$$\begin{array}{rcl} \mathbf{x}_m & = & (\mathbf{x}_s + \mathbf{x}_r)/2 \\ \mathbf{x}_o & = & (\mathbf{x}_s - \mathbf{x}_r) \end{array} . \tag{2.3.1}$$

Considering the 2-D seismic survey for a single seismic line where $y_s = y_r = 0$, the

wavefield can be simplified to a function of three independent variables $w(t, x_s, x_r)$ or $w(t, x_m, x_o)$. The coordinate transformation, in this case, is simplified to

$$\begin{aligned} x_m &= (x_s + x_r)/2 \\ x_o &= x_s - x_r \end{aligned} \tag{2.3.2}$$

and

$$\begin{aligned} x_s &= x_m + x_o/2 \\ x_r &= x_m - x_o/2 \end{aligned} . \tag{2.3.3}$$

The Jacobian determinant of the transformation

$$\begin{vmatrix} \partial x_m/\partial x_s & \partial x_m/\partial x_r \\ \partial x_o/\partial x_s & \partial x_m/\partial x_r \end{vmatrix} = \begin{vmatrix} 1/2 & 1/2 \\ 1 & -1 \end{vmatrix} = 1$$

indicates the area that is invariant under the transformation.

The double Fourier transform of any panel $w(t, x_1)$

$$W(f, k_i) = \int_{-\infty}^{\infty} \int_{-\infty}^{\infty} w(t, x_1) \exp(-j2\pi ft) \exp(-j2\pi k_i x_1)\, dt\, dx_1 \tag{2.3.4}$$

leads to the 2-D f-k spectrum, where k_i, $i = s, r, m, o$ is the wavenumber in source, receiver, midpoint or offset, respectively. The wavefield is now characterized by a 3-D Fourier transform

$$W(f, k_s, k_r) = \int_{-\infty}^{\infty} \int_{-\infty}^{\infty} \int_{-\infty}^{\infty} w(t, x_s, x_r) \exp[-j2\pi(ft + k_s x_s + k_r x_r)]\, dt\, dx_s\, dx_r \tag{2.3.5}$$

or

$$W(f, k_m, k_o) = \int_{-\infty}^{\infty} \int_{-\infty}^{\infty} \int_{-\infty}^{\infty} w(t, x_m, x_o) \exp[-j2\pi(ft + k_m x_m + k_o x_o)]\, dt\, dx_m\, dx_o \tag{2.3.6}$$

leads to the 3-D f-k spectrum in the (f, k_s, k_r) or (f, k_m, k_o) domain. The coordinate transformations defined by equation (2.3.2) and (2.3.3) correspond to the following coordinate transformations in the wavenumber domain:

$$\begin{aligned} k_m &= k_s + k_r \\ k_o &= (k_s - k_r)/2 \end{aligned} \tag{2.3.7}$$

and

$$\begin{aligned} k_s &= k_m/2 + k_o \\ k_r &= k_m/2 - k_o \end{aligned} \quad . \tag{2.3.8}$$

The Jacobian determinants of the transformations (2.3.7) and (2.3.8) are equal to 1. Hence, similar to the transformations defined by equations (2.3.2) and (2.3.3), the area is invariant under the transformations.

Spatial bandwidth limitation

A monochromatic plane wave traveling at apparent velocity V_i along the x_i axis defines a straight line in the frequency-wavenumber (f, k_i) domain:

$$k_i = f/V_i, \qquad i = s, r\,. \tag{2.3.9}$$

Consequently, the energy distribution of the continuous wavefield in the (f, k_i) domain is bounded by lines

$$k_{s,r,o} = \pm f/V_{\min} \quad \text{and} \quad k_m = \pm 2f/V_{\min}\,, \tag{2.3.10}$$

where $V_{\min}$ denotes minimum apparent velocity. This property is also referred to as spatial bandwidth limitation (Berkhout, 1994). If $W(f, k_s, k_r) = 0$ for $f > f_{\max}$, then there exist maximum wavenumbers $|k_{s,r}|_{\max} = f_{\max}/V_{\min}$. Similar reasoning applies to (k_m, k_o). Thus:

$$|k_s|_{\max} = |k_r|_{\max} = |k_o|_{\max} = f_{\max}/V_{\min} \tag{2.3.11}$$

and

$$|k_m|_{\max} = 2f_{\max}/V_{\min}\,. \tag{2.3.12}$$

The energy distribution in the (f, k_i), $i = s$, r, o, m domain is illustrated in Figures 2.7a and 2.7b.

The properties given by (2.3.11) and (2.3.12) also define a square shape of energy distribution in the cross-section (k_s, k_r) or a diamond shape in the cross-section (k_m, k_o) of a common frequency panel. This is illustrated in Figures 2.7c and 2.7d. In particular, waveforms traveling at the minimum apparent velocity $V_{\min}$ have energy only at

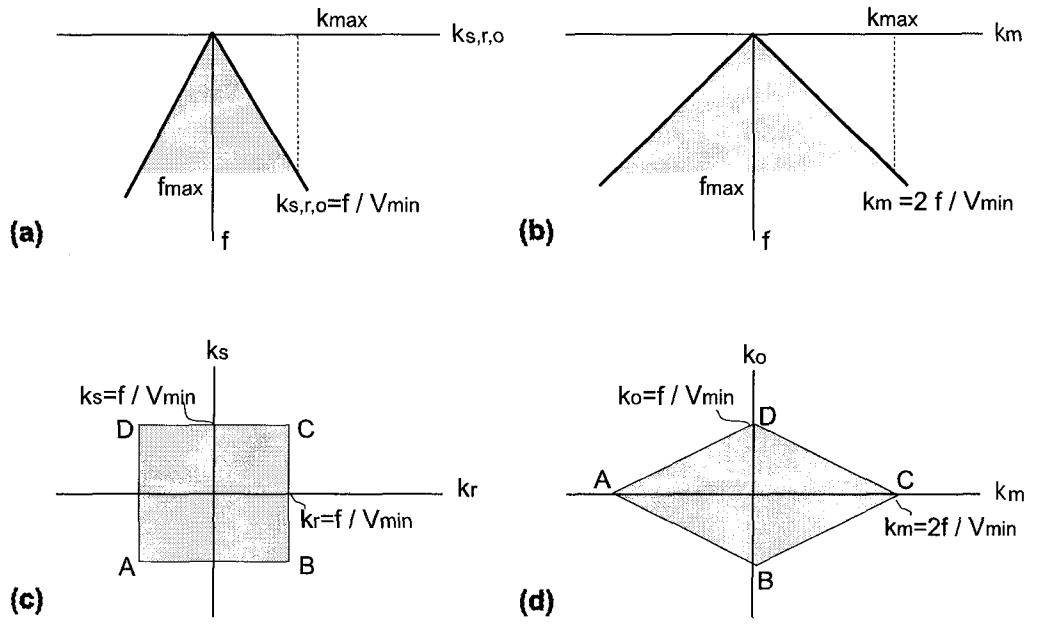

Figure 2.7: (a) Energy distribution in (f, k_s), (f, k_r) and (f, k_o). (b) Energy distribution in (f, k_m). (c) Cross-section (k_s, k_r) of a common frequency panel. (d) Cross-section (k_m, k_o) of a common frequency panel. Modified after Vermeer (1990).

$k_m = 0$, $k_o = \pm f/V_{\min}$, therefore, they correspond to points B and D in Figures 2.7c and 2.7d. Back scattered waves traveling at the minimum velocity $V_{\min}$ has energy only at $k_m = \pm 2f/V_{\min}$, $k_o = 0$, therefore, they correspond to points A and C.

2.3.2 Sampling matrix for the continuous seismic wavefield

Recording the continuous wavefield can be described as a discrete sampling process of the continuous wavefield[3]. The process is analogous to the multi-dimensional sampling process discussed in section 2.2. The sampling theorem states that sampling frequencies should be high enough to ensure aliasing-free sampling, therefore, the continuous wavefield should be sampled with the sampling frequency greater than the Nyquist rate defined by the bandwidth of the continuous wavefield:

[3]Many other effects of recording action are discussed by Vermeer (1990), e.g. receiver response, source wavelet and strength, shot and receiver pattern, additive ambient noise. Only the effects related to the discrete sampling process will be discussed here.

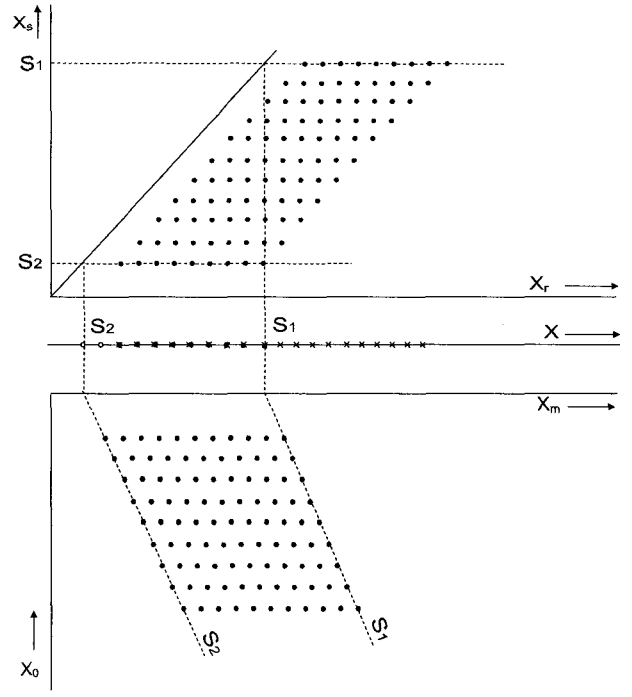

Figure 2.8: Regular off-end shooting geometry, shots moving from right to left. Top:(x_s, x_r) coordinate system, each dot represents a trace in this system, Middle: Shots and receive r positions along seismic line, Bottom: (x_m, x_o) coordinate system, each dot represents a trace in this system. (After Vermeer (1990))

$$\Delta t \leq \frac{1}{f_{\max}},$$

$$\Delta x_s \leq \frac{1}{2|k_s|_{\max}} = \frac{V_{\min}}{f_{\max}},$$

$$\Delta x_r \leq \frac{1}{2|k_r|_{\max}} = \frac{V_{\min}}{f_{\max}},$$

$$\Delta x_o \leq \frac{1}{2|k_o|_{\max}} = \frac{V_{\min}}{f_{\max}},$$

and

$$\Delta x_m \leq \frac{1}{2|k_m|_{\max}} = \frac{V_{\min}}{2f_{\max}}. \tag{2.3.13}$$

Here, Δt denotes the sampling interval in time and Δx_i denotes the sampling period or interval along the x_i axis.

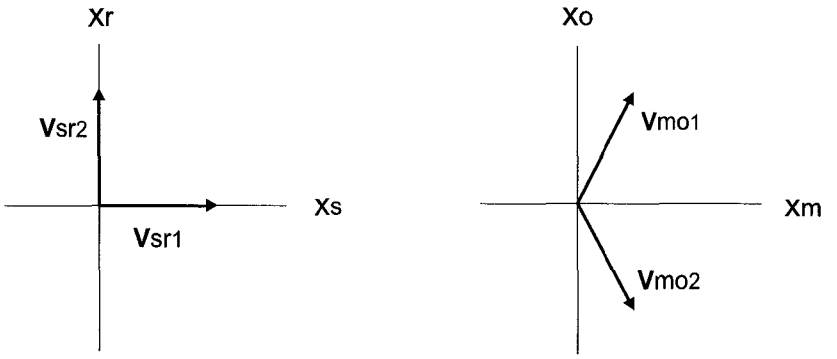

Figure 2.9: The sampling matrices in the shot-receiver domain and midpoint-offset domain. The shot-receiver domain sampling matrix is $\underset{\sim}{\mathbf{V}}_{sr} = [\mathbf{v}_{sr1}\ \mathbf{v}_{sr2}]$ and the midpoint-offset domain sampling matrix is $\underset{\sim}{\mathbf{V}}_{mo} = [\mathbf{v}_{mo1}\ \mathbf{v}_{mo2}]$.

Sampling naturally happens in the shot-receiver domain, and can be transformed into the midpoint-offset domain via coordinate transformations. The wavefield in the shot receiver and midpoint offset domain is illustrated in Figure 2.8. Figure 2.9 depicts sampling matrices in the shot-receiver domain $\underset{\sim}{\mathbf{V}}_{sr} = [\mathbf{v}_{sr1}\ \mathbf{v}_{sr2}]$ and midpoint-offset domain $\underset{\sim}{\mathbf{V}}_{mo} = [\mathbf{v}_{mo1}\ \mathbf{v}_{mo2}]$. According to equation (2.2.20), locations of the 2-D periodic sampling in the (x_s, x_r) plane can be written as

$$\begin{array}{rcl} x_s & = & \frac{V_{\min}}{f_{\max}} n_1 + 0 \\ x_r & = & 0 + \frac{V_{\min}}{f_{\max}} n_2 \end{array} . \tag{2.3.14}$$

In equation (2.3.14), note that the sampling periods along the x_s and x_r axises are chosen to be the maximum aliasing-free sampling periods. The sampling matrix, therefore, is

$$\underset{\sim}{\mathbf{V}}_{sr} = \left[\begin{array}{cc} \mathbf{v}_{sr1} & \mathbf{v}_{sr2} \end{array} \right] \tag{2.3.15}$$

$$= \left[\begin{array}{cc} V_{\min}/f_{\max} & 0 \\ 0 & V_{\min}/f_{\max} \end{array} \right] . \tag{2.3.16}$$

In the midpoint-offset domain, 2-D sampling is defined on the (x_m, x_o) plane. Substituting equation (2.3.14) into equation (2.3.2),

$$x_m = \frac{1}{2}\frac{V_{\min}}{f_{\max}} n_1 + \frac{1}{2}\frac{V_{\min}}{f_{\max}} n_2 \tag{2.3.17}$$

$$x_o = \frac{V_{\min}}{f_{\max}} n_1 - \frac{V_{\min}}{f_{\max}} n_2 . \tag{2.3.18}$$

Therefore, the sampling matrix in the midpoint/offset domain can be written as

$$\underset{\sim}{\mathbf{V}}_{mo} = \left[\begin{array}{cc} \mathbf{v}_{mo1} & \mathbf{v}_{mo2} \end{array} \right] \tag{2.3.19}$$

$$= \left[\begin{array}{cc} V_{\min}/2f_{\max} & V_{\min}/2f_{\max} \\ V_{\min}/f_{\max} & -V_{\min}/f_{\max} \end{array} \right] . \tag{2.3.20}$$

According to equation (2.2.27), with the sampling matrices $\underset{\sim}{\mathbf{V}}_{sr}$ and $\underset{\sim}{\mathbf{V}}_{mo}$, the general matrices $\underset{\sim}{\mathbf{U}}_{sr}$ and $\underset{\sim}{\mathbf{U}}_{mo}$ can be written as (Appendix B):

$$\underset{\sim}{\mathbf{U}}_{sr} = \left[\begin{array}{cc} \mathbf{u}_{sr1} & \mathbf{u}_{sr2} \end{array} \right] \tag{2.3.21}$$

$$= 2\pi \left[\begin{array}{cc} f_{\max}/V_{\min} & 0 \\ 0 & f_{\max}/V_{\min} \end{array} \right] \tag{2.3.22}$$

and

$$\underset{\sim}{\mathbf{U}}_{mo} = \left[\begin{array}{cc} \mathbf{u}_{mo1} & \mathbf{u}_{mo2} \end{array} \right] \tag{2.3.23}$$

$$= 2\pi \left[\begin{array}{cc} f_{\max}/V_{\min} & f_{\max}/V_{\min} \\ f_{\max}/2V_{\min} & -f_{\max}/2V_{\min} \end{array} \right] . \tag{2.3.24}$$

Therefore, the periodicity of the spectrum of the sampled wavefield is described by the general matrix $\underset{\sim}{\mathbf{U}}_{sr}$ in the (k_s, k_r) domain and $\underset{\sim}{\mathbf{U}}_{mo}$ in the (k_m, k_o) domain. This is illustrated in Figure 2.10. In particular, Figure 2.10a shows the spectrum of the sampled wavefield in the cross-section (k_s, k_r) of the common frequency panel at $f = f_{\max}$. The shaded square area indicates the spectrum of the original continuous wavefield and it is separated by two periodicity vectors $\mathbf{u}_s$ and $\mathbf{u}_r$ without overlapping with its replicas. Figure 2.10b shows the spectrum of the sampled wavefield in the cross-section (k_m, k_o) of the common frequency panel at $f = f_{\max}$. The shaded diamond area indicates the spectrum of the original continuous wavefield and it is separated by two periodicity vectors $\mathbf{u}_m$ and $\mathbf{u}_o$ without overlapping with its replicas. Note that although the spectrum of the

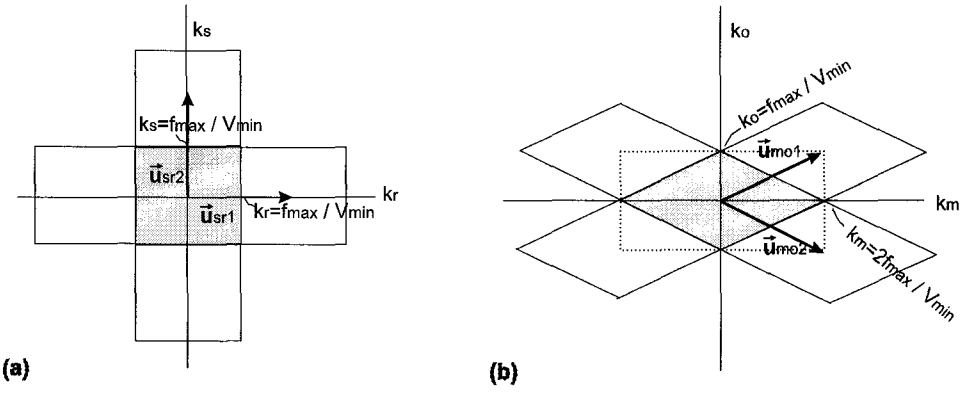

Figure 2.10: The periodicity of the spectrum of the sampled wavefield in the (k_s, k_r) domain and (k_m, k_o) domain. (a) The cross-section (k_s, k_r) of the common frequency panel at $f = f_{\max}$. The shaded square area indicates the spectrum of the original continuous wavefield and it is separated by the two periodicity vectors $\mathbf{u}_{sr1}$ and $\mathbf{u}_{sr2}$. (b) The cross-section (k_m, k_o) of the common frequency panel at $f = f_{\max}$. The shaded diamond area indicates the spectrum of the original continuous wavefield and it is separated by the two periodicity vectors $\mathbf{u}_{mo1}$ and $\mathbf{u}_{mo2}$.

original continuous wavefield is not aliased by its replicas, the (k_m, k_o) spectrum inside the dash-line box is composed of the spectrum of the original continuous wavefield and its replicas. Consequently, the properly sampled data in the shot-receiver domain may appear to be aliased in the midpoint-offset domain depending on the bandwidth of the original spectrum. This leads to a sampling paradox discussed in (Vermeer, 1990).

2.3.3 Reconstruction of the continuous seismic wavefield

The reconstruction of the continuous seismic wavefield can be done in a way analogous to the reconstruction of multi-dimensional signals discussed in section 2.2. In particular, the reconstruction of the original continuous wavefield can be done in both the shot-receiver domain and midpoint-offset domain. If the Nyquist sampling rate is satisfied, the reconstruction result from two different domains should be the same. In other words, the continuous wavefield can be reconstructed exactly from the sampling data in both the shot-receiver domain and midpoint-offset domain. Obviously, 2-D low-pass filters used for the shot-receiver domain and midpoint-offset domain data reconstruction may have

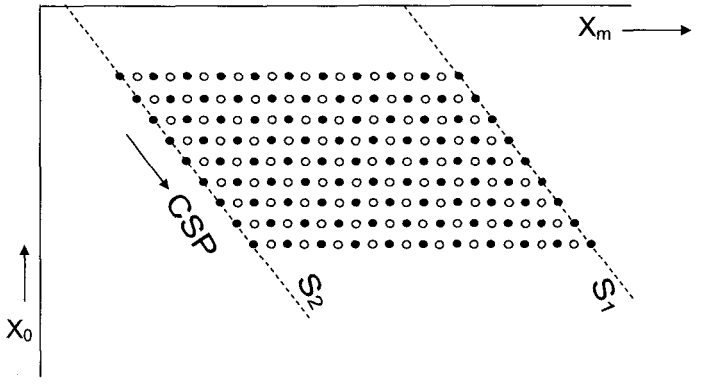

Figure 2.11: To de-aliasing in CMPs and COPs, the new traces marked with small circles need to be interpolated. The interpolation can be done in the shot-receiver domain with a horizontal (shot direction) low-pass filter or in the midpoint-offset domain with a diamond shape low-pass filter as shown in Figure 2.10.

different shapes (i.e. a square shape or a diamond shape).

It is important to stress that the 2-D reconstruction of the continuous wavefield should not be affected by the sampling paradox. As long as the original spectrum is not overlapped by its replicas (i.e. as the case shown in Figure 2.10), the total wavefield is properly sampled in (t, x_s, x_r) and therefore also in (t, x_m, x_o). The 2-D reconstruction can then be used to obtain the continuous wavefield. However, the fact remains that even if the total wavefield is properly sampled, any individual common offset pannels (COP) and common midpoint pannels (CMP) may be undersampled. To achieve proper sampling in any one of the individual gathers, the missing data in the midpoint-offset domain needs to be reconstructed. An example is shown in Figure 2.11 where the original data (denoted with black dots) are properly sampled in the shot and receiver domain. The small circle mark indicates the new traces that one needs to generate to avoid aliasing in common-offset or common-midpoint individual gathers; this can be simply done by applying a diamond shape interpolation filter (as shown in Figure 2.10) in the midpoint-offset domain or a horizontal (shot direction) low-pass filter in the shot-receiver domain.

2.4 Summary

This chapter reviews periodic sampling of a continuous signal and band limited reconstruction of a continuous signal from its discrete representation (sampling). In particular, the recorded seismic data can be regarded as a discrete representation of a continuous wavefield. It is possible to uniquely reconstruct a band limited continuous wavefield from the discrete sampling if the continuous wavefield is sampled with the sampling frequency greater than the Nyquist sampling rate defined by the bandwidth of the continuous wavefield. In other words, the continuous wavefield can be fully reconstructed if the sampled wavefield is not aliased. For 2-D wavefield reconstruction, the reconstruction can be done in both the shot-receiver and midpoint-offset domain. It is important to stress that a multi-dimensional wavefield may be properly sampled in the multi-dimensional domain but poorly sampled (aliased) in individual domains which lead to a sampling paradox. A multi-dimensional band limited reconstruction scheme will not be affected by the sampling paradox.

Chapter 3

MWNI of seismic data

3.1 Introduction

The goal of the geophysical exploration is to reconstruct a subsurface image of Earth from the seismic data recorded on the acquisition at the surface. A continuous seismic wavefield is a multi-dimensional signal of time and space. To uniquely represent the continuous wavefield from recorded data, the wavefield should be sampled at a rate higher than its Nyquist rate. However, recorded seismic data are always spatially incomplete to some degree: The receiver coverage is necessarily limited in areal extent; sparse sampling often happens in 3-D surveys due to economic reasons; irregular gaps are often present in recorded data due to field obstacles and other reasons. In addition, recorded data will contain addictive noise. In this case, the problem of reconstruction of the continuous wavefield has no unique solution and can only be dealt with in discrete time or space. The inverse theory provides a formalism to deal with these problems. In fact, inverse theory is also used in many seismic data reconstruction methods, for example, prediction error filtering interpolation (Spitz, 1991; Claerbout, 1992), wave equation based interpolation (Ronen, 1987). Similarly, the band limited data interpolation/extrapolation problem can also be posed as an inverse problem where from inadequate and incomplete data one attempts to recover the band limited seismic wavefield (Cary, 1997; Hindriks et al., 1997; Duijndam et al., 1999; Schonewille, 2000).

The inverse problem is often ill-posed and, as it is well known, it can be honored by many solutions. In this case, a regularization strategy can be used to retrieve a unique and stable solution. Criteria to choose a suitable regularization strategy in the context of

interpolation and extrapolation have been discussed by several researchers (Cabrera and Parks, 1991; Sacchi and Ulrych, 1996; Hindriks et al., 1997; Sacchi et al., 1998; Duijndam et al., 1999; Zwartjes and Duijndam, 2000). For example, minimum norm spectral regularization can be used when seismic data are assumed to be bandlimited in the spatial wavenumber domain (Duijndam et al., 1999). Similarly, a regularization derived using the Cauchy criterion can be used to obtain a high resolution (sparse) discrete Fourier transform that can be used to perform the synthesis of data at new spatial positions (Sacchi and Ulrych, 1996; Sacchi et al., 1998; Zwartjes and Duijndam, 2000). Liu and Sacchi (2001; 2003) have proposed a MWNI algorithm where band limited interpolation is formulated as a minimum-norm least-squares problem where an adaptive discrete Fourier transform (DFT)-weighted norm regularization term is used to constrain the solution. The method permits one to incorporate the a priori spectral signature of the unknown wavefield.

In this chapter, the MWNI algorithm (Liu and Sacchi, 2001; Liu and Sacchi, 2003) is developed to perform multi-dimensional reconstruction of seismic wavefields. Numerical examples with synthetic and field data are used to demonstrate the merits of the proposed interpolation scheme.

The 1-D interpolation problem is analyzed first. The extension to higher dimensions is proposed in section 3.3 of this chapter. By 1-D interpolation, interpolation is understood in the f-x domain along the spatial dimension x. In other words, a seismic gather in the t-x domain is first transformed to the frequency domain and, then, interpolation is carried out along the spatial dimension x for each temporal frequency f. This thesis addresses the reconstruction problem along spatial dimensions since reflection seismic data are nearly always adequately sampled in time.

3.2 Interpolation of band limited data

3.2.1 Basic definitions and problems set up

The discrete-time or space problem of interpolation/extrapolation involves an infinite length signal $x(n)$ indexed on integer variable $-\infty < n < \infty$; for which its Fourier transform can be defined as

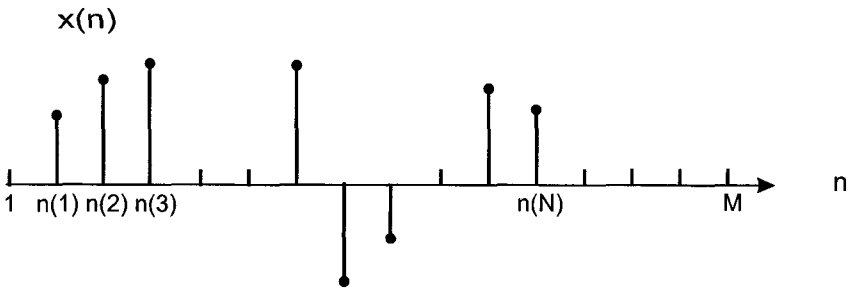

Figure 3.1: The band limited interpolation/extrapolation problem: the given time samples are $x_{n(1)}, x_{n(2)}, x_{n(3)}, \ldots, x_{n(N)}$ and are located in the interval $[1, M]$. The remaining samples in this interval are to be estimated.

$$X(f) = \sum_{n=-\infty}^{\infty} x(n) e^{-j2\pi fn} \tag{3.2.1}$$

and the inverse Fourier transform is defined as

$$x(n) = \frac{1}{2\pi} \int_{2\pi} X(f) e^{j2\pi fn} df\,, \tag{3.2.2}$$

where $f =\in [-0.5, 0.5]$ denotes the normalized frequency in Hz. The sequence is band limited to a support region β (a subset of $[-0.5, 0.5]$) if $X(f) = 0$ for those frequencies that do not belong to β. Note that β may consist of a series of intervals. Figure 3.1 shows the typical situation in the discrete-time, band limited interpolation/extrapolation problem. Only finite number of samples of $x(n)$: $x_{n(1)}, x_{n(2)}, x_{n(3)}, \ldots, x_{n(N)}$ are known and their locations are indicated by $n(1), n(2), n(3), \ldots, n(N)$. The rest of samples are to be estimated.

If the given samples of interest are included in the range $1 - M$ as shown in Figure 3.1, the problem of estimating these M values (samples) can be expressed using finite dimensional vectors and matrices.

We will denote $\mathbf{x}$ the length-M vector of data sampled on a regular grid $x_1, x_2, x_3, \ldots, x_M$. The observations are given by the elements of the vector $\mathbf{y} = [x_{n(1)}, x_{n(2)}, x_{n(3)}, \ldots, x_{n(N)}]^T$ where the set $\mathcal{N} = \{n(1), n(2), n(3), \ldots, n(N)\}$ is used to indicate the position of the known samples or observations. We now define the sampling matrix $\underset{\sim}{\mathbf{T}}$ with elements $T_{i,j} = \delta_{n(i),j}$, where δ indicates the Kronecker operator. It is quite simple to show that

the complete data and the observations are connected by the following linear system

$$\mathbf{y} = \underset{\sim}{\mathbf{T}}\mathbf{x}. \tag{3.2.3}$$

For example, if we assume that the complete data consist of $M = 5$ consecutive samples $\mathbf{x} = [x_1, x_2, x_3, x_4, x_5]^T$, whereas the observations (available data) are given by samples at positions $\mathcal{N} = \{2, 3, 5\}$, that is $\mathbf{y} = [x_2, x_3, x_5]^T$. Then, equation (3.2.3) becomes

$$\begin{pmatrix} x_2 \\ x_3 \\ x_5 \end{pmatrix} = \begin{pmatrix} 0 & 1 & 0 & 0 & 0 \\ 0 & 0 & 1 & 0 & 0 \\ 0 & 0 & 0 & 0 & 1 \end{pmatrix} \begin{pmatrix} x_1 \\ x_2 \\ x_3 \\ x_4 \\ x_5 \end{pmatrix}. \tag{3.2.4}$$

Note that the sampling operator $\mathbf{T}$ has the following property:

$$\underset{\sim}{\mathbf{T}}\underset{\sim}{\mathbf{T}}^T = \underset{\sim}{\mathbf{I}}_N, \tag{3.2.5}$$

where $\underset{\sim}{\mathbf{I}}_N$ denotes the $N \times N$ identity matrix. It can also be shown that $\underset{\sim}{\mathbf{T}}^T\underset{\sim}{\mathbf{T}} \neq \underset{\sim}{\mathbf{I}}_M$.

Define the Discrete Fourier Transform (DFT) and the Inverse Discrete Fourier Transform (IDFT) as follows:

$$X_k = \frac{1}{\sqrt{M}} \sum_{m=1}^{M} x_m \, e^{-i\,2\pi\,(m-1)\,(k-1)/M}, \quad k = 1, \ldots, M \tag{3.2.6}$$

$$x_m = \frac{1}{\sqrt{M}} \sum_{k=1}^{M} X_k \, e^{i\,2\pi\,(m-1)\,(k-1)/M}, \quad m = 1, \ldots, M. \tag{3.2.7}$$

The following compact notation will be used for the DFT and IDFT, respectively:

$$\mathbf{X} = \underset{\sim}{\mathbf{F}}\mathbf{x} \tag{3.2.8}$$

$$\mathbf{x} = \underset{\sim}{\mathbf{F}}^H\mathbf{X} \tag{3.2.9}$$

where the superscript ^{H} is used to denote the Hermitian transpose. Notice that $\underset{\sim}{\mathbf{F}}$ is the DFT unitary matrix with inverse given by $\underset{\sim}{\mathbf{F}}^{-1} = \underset{\sim}{\mathbf{F}}^H$.

The length-M signal will be said to be band limited (or DFT-limited) if its DFT vanishes outside of the support $\mathcal{K}$, a set of integer index $\{k_1, k_2, k_3, \cdots, k_J\}$, which is a

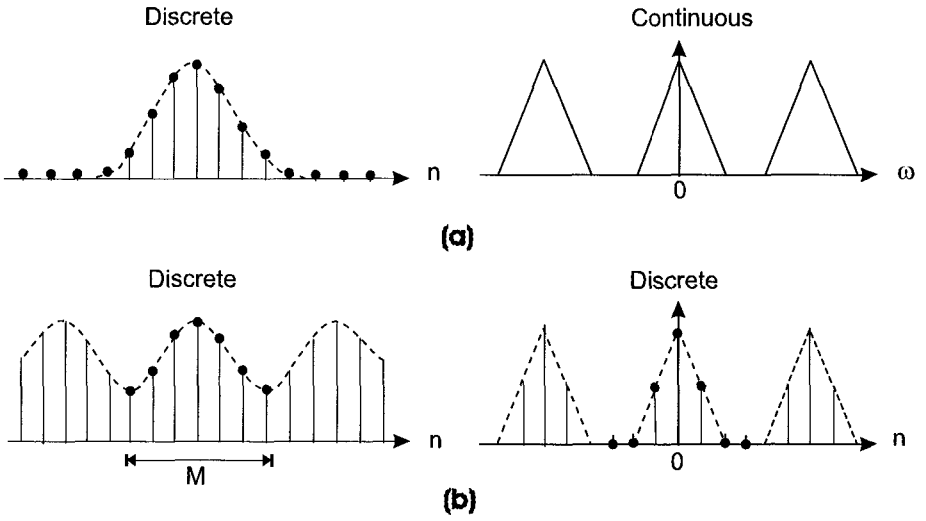

Figure 3.2: (a) An infinite sequence and its discrete time Fourier transform spectrum. (b) A finite sequence and its DFT spectrum.

subset of $[1, M]$. Figure 3.2b depicts a finite sequence and its DFT. Unlike an infinite sequence which has continuous frequencies (shown in Figure 3.2a), the DFT of an finite sequence has discrete frequencies. Applying an M-point DFT to M values of $x(n)$ means that it is considered as a sequence that is periodic with period M so that $x(n) = x(n+rM)$ for any integer value of r.

3.2.2 Minimum weighted norm inversion of the sampling operator

The signal reconstruction or interpolation problem given by equation (3.2.3) entails the solution of an under-determined system of equations (more unknowns than observations). It is clear that the problem does not have a unique solution. In general, one way of solving this type of problems is by restricting the class of solutions by providing suitable prior information. For example, a solution can be sought such that the model norm is minimum among all the possible solutions. In the absence of errors, the inversion can be reduced to solving the following constrained minimization problem:

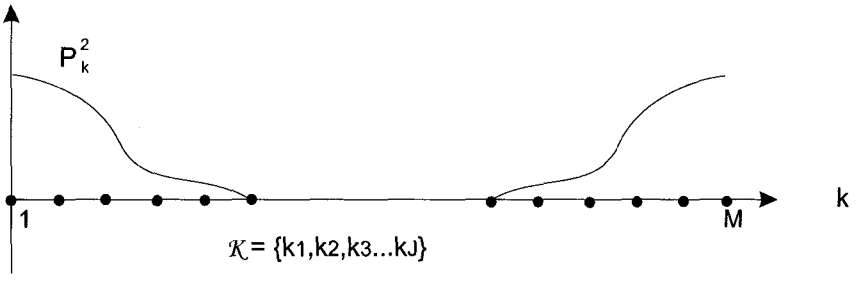

Figure 3.3: The weighting function P_k^2 is defined with the same support and similar shape as the DFT-limited sequence which also defines the weighted norm

$$\begin{aligned} &\text{Minimize} && ||\mathbf{x}||_{\mathcal{W}}^2 ||\mathbf{x}||_{\mathcal{W}}^2 \\ &\text{Subject to} && \underset{\sim}{\mathbf{T}}\mathbf{x} = \mathbf{y}\,, \end{aligned}$$

where $||.||_{\mathcal{W}}$ is used to indicate a weighted norm. Following Cabrera and Parks (1991), the following wavenumber domain norm is selected:

$$||\mathbf{x}||_{\mathcal{W}}^2 = \sum_{k \in \mathcal{K}} \frac{X_k^* X_k}{P_k^2} \tag{3.2.10}$$

where P_k^2 are spectral domain weights with support and shape similar to those of the signal to interpolate; the set of indexes $\mathcal{K}$ are used to indicate the region of spectral support of the signal. This is illustrated in Figure 3.3. It is understood that the $P_k \neq 0$ for $k \in \mathcal{K}$. The coefficient P_k represents the spectral power at wavenumber index k.

Now introduce the following diagonal matrix $\underset{\sim}{\mathbf{\Lambda}}$ with elements given by

$$\Lambda_k = \begin{cases} P_k^2 & k \in \mathcal{K} \\ 0 & k \notin \mathcal{K} \end{cases} . \tag{3.2.11}$$

Similarly, define the pseudoinverse of the diagonal matrix $\underset{\sim}{\mathbf{\Lambda}}$, as the matrix $\underset{\sim}{\mathbf{\Lambda}}^{\dagger}$ with elements given by

$$\Lambda^{\dagger}{}_k = \begin{cases} P_k^{-2} & k \in \mathcal{K} \\ 0 & k \notin \mathcal{K} \end{cases} . \tag{3.2.12}$$

The wavenumber domain norm can now be expressed as

$$||\mathbf{x}||_{\mathcal{W}}^2 = \mathbf{X}^H \underset{\sim}{\Lambda}^\dagger \mathbf{X}. \tag{3.2.13}$$

After combining equations (3.2.8) and (3.2.13), the following expression can be arrived:

$$\begin{aligned} ||\mathbf{x}||_{\mathcal{W}}^2 &= \mathbf{x}^H \underset{\sim}{\mathbf{F}}^H \underset{\sim}{\Lambda}^\dagger \underset{\sim}{\mathbf{F}}\, \mathbf{x} \\ &= \mathbf{x}^H \underset{\sim}{\mathbf{Q}}^\dagger \mathbf{x} \end{aligned} \tag{3.2.14}$$

where the matrix $\underset{\sim}{\mathbf{Q}}^\dagger = \underset{\sim}{\mathbf{F}}^H \underset{\sim}{\Lambda}^\dagger \underset{\sim}{\mathbf{F}}$ is a circulant matrix (Strang, 1986). The pseudoinverse of the matrix $\underset{\sim}{\mathbf{Q}}^\dagger$ is also a circulant matrix $\underset{\sim}{\mathbf{Q}} = \underset{\sim}{\mathbf{F}}^H \underset{\sim}{\Lambda} \underset{\sim}{\mathbf{F}}$. For example, let c_m be the inverse DFT of the diagonal elements of the matrix $\underset{\sim}{\Lambda}$, $\underset{\sim}{\mathbf{Q}}$ is a circular convolution filtering matrix

$$\underset{\sim}{\mathbf{Q}} = \begin{bmatrix} c_1 & c_M & c_{M-1} & \cdots & c_2 \\ c_2 & c_1 & c_M & \cdots & c_3 \\ c_3 & c_2 & \cdot & \cdots & \cdot \\ \vdots & \vdots & \cdot & \cdots & \cdot \\ c_M & c_{M-1} & \cdot & \cdots & c_1 \end{bmatrix}.$$

Both $\underset{\sim}{\mathbf{Q}}$ and $\underset{\sim}{\mathbf{Q}}^\dagger$ are band limiting operators. In other words, they annihilate any spectral component $k \notin \mathcal{K}$.

The minimum norm solution is found by minimizing the following cost function:

$$J = \boldsymbol{\lambda}^T(\underset{\sim}{\mathbf{T}}\mathbf{x} - \mathbf{y}) + ||\mathbf{x}||_{\mathcal{W}}^2.$$

In the above equation $\boldsymbol{\lambda}$ denotes the vector of Lagrange multipliers. Minimizing J with respect to $\mathbf{x}$ subject to $\underset{\sim}{\mathbf{T}}\mathbf{x} - \mathbf{y} = \mathbf{0}$ leads to the following solution (see Appendix C):

$$\hat{\mathbf{x}} = \underset{\sim}{\mathbf{Q}}\underset{\sim}{\mathbf{T}}^T (\underset{\sim}{\mathbf{T}}\underset{\sim}{\mathbf{Q}}\underset{\sim}{\mathbf{T}}^T)^{-1} \mathbf{y}. \tag{3.2.15}$$

In the previous derivation the matrix $(\underset{\sim}{\mathbf{T}}\underset{\sim}{\mathbf{Q}}\underset{\sim}{\mathbf{T}}^T)$ is assumed to be invertible. If this is not the case, the inverse can be replaced by the Moore-Penrose pseudoinverse (Cabrera and Parks, 1991).

The above solution is designated as Minimum Weighted Norm Interpolation (MWNI). We will reserve the name Minimum Norm Interpolation (MNI) for the case where $\underset{\sim}{\mathbf{Q}}$ is a band-pass filter with spectral weights $P_k^2 = 1, k \in \mathcal{K}$. In other words, we constrain the solution to the class of band limited signals with spectral components in $k \in \mathcal{K}$, and we made no attempt to impose an a priori spectral shape.

Consider the special case when $\underset{\sim}{\mathbf{Q}}$ is an all-pass filtering matrix with DFT coefficients $\Lambda_k = 1$ for all $k = 1, \ldots M$. In this case, $\underset{\sim}{\mathbf{\Lambda}} = \underset{\sim}{\mathbf{I}}$, and after invoking the orthonormality of the DFT operator we obtain the following expression:

$$\hat{\mathbf{x}} = \underset{\sim}{\mathbf{T}}^T(\underset{\sim}{\mathbf{T}}\underset{\sim}{\mathbf{T}}^T)^{-1}\mathbf{y} = \underset{\sim}{\mathbf{T}}^T\mathbf{y}\,. \tag{3.2.16}$$

In the example provided by equation (3.2.4), the minimum norm solution becomes:

$$\hat{\mathbf{x}} = \underset{\sim}{\mathbf{T}}^T\mathbf{y} = \begin{pmatrix} 0 \\ x_2 \\ x_3 \\ 0 \\ x_5 \end{pmatrix}. \tag{3.2.17}$$

In other words, missing samples were filled in with zeros. This proves that without any constraints, the minimum norm type of method yields a solution with minimum energy.

3.2.3 Inversion of T in the presence of noise

When the observations contain additive noise rather than trying to fit exactly all the observations, the observations can be fit in the least-squares sense. In this case a cost function that combines a data misfit function in conjunction with the model norm is minimized:

$$J = ||\underset{\sim}{\mathbf{T}}\mathbf{x} - \mathbf{y}||^2 + \rho^2||\mathbf{x}||^2_{\mathcal{W}}\,, \tag{3.2.18}$$

where ρ^2 is the trade-off parameter of the problem. Notice that minimizing J is equivalent to find the least-squares solution of the following over-determined system of equations

$$\begin{pmatrix} \underset{\sim}{\mathbf{T}} \\ \rho\underset{\sim}{\mathbf{W}} \end{pmatrix}\mathbf{x} \approx \begin{pmatrix} \mathbf{y} \\ \mathbf{0} \end{pmatrix} \tag{3.2.19}$$

where according to our previous definitions, the matrix of weights $\underset{\sim}{\mathbf{W}}$ is given by

$$\underset{\sim}{\mathbf{W}} = \underset{\sim}{\mathbf{\Lambda}}^{\dagger 1/2}\underset{\sim}{\mathbf{F}}\,. \tag{3.2.20}$$

Unfortunately, the augmented matrix of the problem is rank deficient, and, therefore, equation (3.2.19) does not have a unique solution. The latter can be solved by choosing, among all possible least-squares solutions, the one with minimum Euclidean norm. This can be done with the aid of the Singular Value Decomposition (SVD) (Golub and Reinsch, 1970) of the augmented matrix. In particular, the $(N + M) \times M$ augmented matrix

$$\underset{\sim}{\mathbf{L}} = \begin{pmatrix} \underset{\sim}{\mathbf{T}} \\ \rho \underset{\sim}{\mathbf{W}} \end{pmatrix}$$

is decomposed into the product of three matrices: $\underset{\sim}{\mathbf{L}} = \underset{\sim}{\mathbf{V}}\underset{\sim}{\mathbf{D}}\underset{\sim}{\mathbf{U}}^T$, where $\underset{\sim}{\mathbf{V}}$ is an orthogonal $(N+M) \times (N+M)$ matrix of left singular vectors, $\underset{\sim}{\mathbf{U}}$ is an orthogonal $M \times M$ matrix of right singular vectors, and $\underset{\sim}{\mathbf{D}}$ is a diagonal $(N+M) \times M$ matrix of singular values. The least-squares solution to equation (3.2.19) is then

$$\hat{\mathbf{x}} = \underset{\sim}{\mathbf{U}}\underset{\sim}{\mathbf{D}}^{-1}\underset{\sim}{\mathbf{V}}\mathbf{d} \tag{3.2.21}$$

where

$$\mathbf{d} = \begin{pmatrix} \mathbf{y} \\ \mathbf{0} \end{pmatrix}. \tag{3.2.22}$$

The matrix $\underset{\sim}{\mathbf{U}}\underset{\sim}{\mathbf{D}}^{-1}\underset{\sim}{\mathbf{V}}$ is the generalized inverse of the rectangular matrix $\underset{\sim}{\mathbf{L}}$. Since $\underset{\sim}{\mathbf{L}}$ is rank deficient, the SVD will give the least-squares solution whose Euclidean norm is smaller than all other least-squares solutions (Campell and Meyer, 1979). Alternatively, the method of CG can be used. For rank-deficient problems, the solution to which the CG method converges depends upon the initial approximation adopted. If the initial approximation is chosen to be $\mathbf{x} = \mathbf{0}$, then CG converges to the minimum-norm least-squares solution (Hestenes, 1975). One advantage of using the CG method is that the computational cost of the algorithm heavily depends on matrix times vector operations. These operations can be efficiently performed using the FFT.

In the numerical implementation, equation (3.2.19) is modified with the following change of variable: $\mathbf{z} = \underset{\sim}{\mathbf{W}}\mathbf{x}$. The augmented system becomes

$$\begin{pmatrix} \underset{\sim}{\mathbf{T}}\underset{\sim}{\mathbf{W}}^{\dagger} \\ \rho \end{pmatrix} \mathbf{z} \approx \begin{pmatrix} \mathbf{y} \\ \mathbf{0} \end{pmatrix}. \tag{3.2.23}$$

The trade-off parameter can be set to $\rho = 0$ and the number of iterations in the CG method play the role of regularization parameter (Hansen, 1998). Finally,

$$\underset{\sim}{\mathbf{T}}\underset{\sim}{\mathbf{W}}^{\dagger}\mathbf{z} \approx \mathbf{y} \tag{3.2.24}$$

is solved with CG and and the algorithm is stopped when a maximum number of iterations is reached or a desired misfit is achieved. The CG method often converges in less than 20 iterations.

$\mathbf{z}_0 = \mathbf{0}$;
$\mathbf{s}_0 = \mathbf{y} - \hat{\underset{\sim}{\mathbf{T}}}\mathbf{z}_0 = \mathbf{y}$;
$\mathbf{r}_0 = \mathbf{p}_0 = \hat{\underset{\sim}{\mathbf{T}}}^*(\mathbf{y} - \hat{\underset{\sim}{\mathbf{T}}}\mathbf{z}_0) = \hat{\underset{\sim}{\mathbf{T}}}^*\mathbf{y}$;
$\mathbf{q}_0 = \hat{\underset{\sim}{\mathbf{T}}}\mathbf{p}_0$;
$\gamma_0 = (\mathbf{r}_0, \mathbf{r}_0)$;

for $i = 0 : niter$
  $\alpha_{i+1} = \gamma_0/(\mathbf{q}_i, \mathbf{q}_i)$;
  $\mathbf{z}_{i+1} = \mathbf{z}_i + \alpha_{i+1}\mathbf{p}_i$;
  $\mathbf{s}_{i+1} = \mathbf{s}_i - \alpha_{i+1}\mathbf{q}_i$;
  $\mathbf{r}_{i+1} = \hat{\underset{\sim}{\mathbf{T}}}^*\mathbf{s}_{i+1}$;
  $\gamma_{i+1} = (\mathbf{r}_{i+1}, \mathbf{r}_{i+1})$;
  if $\gamma_{i+1} < tol * \|\mathbf{y}\|_2^2$
    break;
  end;
  $\beta_{i+1} = \gamma_{i+1}/\gamma_i$;
  $\mathbf{p}_{i+1} = \mathbf{r}_i + \beta_{i+1}\mathbf{p}_i$;
  $\mathbf{q}_{i+1} = \hat{\underset{\sim}{\mathbf{T}}}\mathbf{p}_{i+1}$;
end

Table 3.1: Conjugate gradient algorithm for non-square matrix.

A CG algorithm for non-square matrix is shown in Table 3.1 (Hestenes and Stiefel, 1952). Where $\hat{\underset{\sim}{\mathbf{T}}}$ and $\hat{\underset{\sim}{\mathbf{T}}}^*$ are forward and adjoint operators respectively:

$$\hat{\underset{\sim}{\mathbf{T}}} = \underset{\sim}{\mathbf{T}}\underset{\sim}{\mathbf{\Lambda}}^{\dagger 1/2}\underset{\sim}{\mathbf{F}} \tag{3.2.25}$$

and

$$\hat{\underset{\sim}{\mathbf{T}}}^* = \underset{\sim}{\mathbf{F}}^H\underset{\sim}{\mathbf{\Lambda}}^{\dagger 1/2}\underset{\sim}{\mathbf{T}}^T. \tag{3.2.26}$$

As discussed before, the main computational burden of CG methods is the matrix-vector products with the system matrix. For the MWNI algorithm, matrix-vector operations involving operators $\hat{\underset{\sim}{\mathbf{T}}}$ and $\hat{\underset{\sim}{\mathbf{T}}}^*$ can be done very efficiently: The forward operation (applying $\hat{\underset{\sim}{\mathbf{T}}}$) is to apply the FFT, multiply by diagonal weights and truncate; The adjoint operation (applying $\hat{\underset{\sim}{\mathbf{T}}}^*$) is to pad with zero, multiply by diagonal weights and apply the inverse FFT. Note that when coding the CG algorithm, it's important to test if $\hat{\underset{\sim}{\mathbf{T}}}$ and $\hat{\underset{\sim}{\mathbf{T}}}^*$ are indeed an adjoint operator pair. According to the definition of the adjoint operator, the operator and its adjoint satisfy

$$< \mathbf{d}, \hat{\underset{\sim}{\mathbf{T}}}^*\mathbf{f} > = < \hat{\underset{\sim}{\mathbf{T}}}\mathbf{d}, \mathbf{f} >, \tag{3.2.27}$$

for any vector **d** and **f**. A dot product test (Claerbout, 1992) can be carried by loading **d** and **f** with random numbers. If $\hat{\underset{\sim}{\mathbf{T}}}^*$ and $\hat{\underset{\sim}{\mathbf{T}}}$ has been properly implemented, equation (3.2.27) should be satisfied down to the least significant digit.

At this point a few comments are in order. The transition from equation (3.2.19) to (3.2.23) is only valid for a full rank matrix $\underset{\sim}{\mathbf{W}}$. Solving for a band limited solution ($k \in \mathcal{K}$), however, permits one to claim that solving equation (3.2.23) is equivalent to solving equation (3.2.19) even when the rank of $\underset{\sim}{\mathbf{W}}$ is not full (see Appendix D).

3.2.4 A comparison of high resolution Fourier transform approach and MWNI

There is certain similarity between the MWNI method and the high resolution Fourier transform (HRFT) approach proposed by Sacchi and Ulrych (Sacchi and Ulrych, 1996). This section compares the MWNI and HRFT methods.

In HRFT method, one estimates DFT coefficients based on the available data:

$$y_n = \frac{1}{\sqrt{M}} \sum_{k=1}^{M} X_k \, e^{i\,2\pi\,(n-1)\,(k-1)/M}, \quad n = 1, \ldots, N \tag{3.2.28}$$

where $M > N$. Note that the IDFT of the estimated DFT coefficients gives the unknown data x_m. The above equation gives rise to a linear system of equations:

$$\mathbf{y} = \hat{\underset{\sim}{\mathbf{F}}}^H \mathbf{X} \tag{3.2.29}$$

where $\hat{\underset{\sim}{\mathbf{F}}}^H$ is a $N \times M$ matrix, as opposed to the $M \times M$ matrix $\underset{\sim}{\mathbf{F}}^H$ in equation (3.2.9). The linear equation in (3.2.29) is inverted using the Bayesian approach (e.g. Tarantola (1987)) by seeking the maximum of the posteriori probability density function (pdf):

$$p(\mathbf{X}|\mathbf{y}) \propto p(\mathbf{y}|\mathbf{X}) p(\mathbf{X}) \tag{3.2.30}$$

where the data likelihood is given by

$$p(\mathbf{y}|\mathbf{X}) \propto \exp(-\frac{1}{2} (\hat{\underset{\sim}{\mathbf{F}}}^H \mathbf{X} - \mathbf{y})^H \sigma_n^{-2} \mathbf{y} (\hat{\underset{\sim}{\mathbf{F}}}^H \mathbf{X} - \mathbf{y})) \tag{3.2.31}$$

and a prior distribution of the model is given by the Cauchy pdf

$$p(\mathbf{X}) \propto \frac{1}{1 + \frac{X_k X_k^*}{2\sigma_c^2}}. \tag{3.2.32}$$

The MAP (maximum a posteriori) solution that maximizes the posteriori probability $\ln(p(\mathbf{X}|\mathbf{y})$ also minimizes the following cost function

$$J_{cg}(\mathbf{X}) = ||\mathbf{X}||_c + \frac{1}{\sigma_n^2}||\mathbf{y} - \hat{\underset{\sim}{\mathbf{F}}}^H\mathbf{X}||_2^2, \tag{3.2.33}$$

where

$$||\mathbf{X}||_c = \sum_k \ln(1 + \frac{X_k X_k^*}{2\sigma_c^2}). \tag{3.2.34}$$

The regularizer $||\mathbf{X}||_c$ imposed by the 'long tailed' Cauchy distribution is a measure of the sparseness of spectral powers. The constant σ_c controls the amount of sparseness that can be attained by the inversion. Taking derivative of $J_{cg}(\mathbf{X})$ and equating to zero yields the following result

$$\hat{\mathbf{X}} = (\lambda\hat{\underset{\sim}{\mathbf{Q}}}^{-1} + \hat{\underset{\sim}{\mathbf{F}}}\hat{\underset{\sim}{\mathbf{F}}}^H)^{-1}\hat{\underset{\sim}{\mathbf{F}}}\mathbf{y} \tag{3.2.35}$$

which is equivalent to

$$\hat{\mathbf{X}} = \hat{\underset{\sim}{\mathbf{Q}}}\hat{\underset{\sim}{\mathbf{F}}}(\lambda\underset{\sim}{\mathbf{I}} + \hat{\underset{\sim}{\mathbf{F}}}^H\hat{\underset{\sim}{\mathbf{Q}}}\hat{\underset{\sim}{\mathbf{F}}})^{-1}\mathbf{y}, \tag{3.2.36}$$

where $\lambda = \sigma_n^2/\sigma_c^2$ and $\hat{\underset{\sim}{\mathbf{Q}}}$ is a $M \times M$ diagonal matrix with elements given by

$$Q_{ii} = 1 + \frac{X_k X_k^*}{2\sigma_c^2}, \quad i = 1, \cdots, M. \tag{3.2.37}$$

The Cauchy-Gauss model leads to a algorithm that resembles the minimum norm solution of equation (3.2.29) when σ_c is large compared to spectrum amplitudes we are seeking. In the contrary case, when σ_c is small, the algorithm will seek a DFT with a sparse distribution of spectral amplitudes, leading to an enhancement of the spectral perks and reducing windowing effects or sidelobes (Sacchi and Ulrych, 1996).

The proposed MWNI algorithm is different than the HRFT approach using sparseness constraints. First of all, our new algorithm does not assume a sparse distribution of spectral amplitudes. The latter is only valid for estimating the DFT of a process that consists of a finite number of spectral lines (Sacchi et al., 1998). The norm in equation (3.2.34) and the norm utilized in this thesis (equation (3.2.10)) are different. The Cauchy criterion was proposed as a mean of estimating sparse (high resolution) spectral estimators for waveforms that can be approximated by plane waves. In this case, a sparse spectrum is the appropriate model for data that consists of a superposition of a few plane waves. In this thesis, however, we have proposed a more general norm that is capable

of handling non-sparse spectral models. This is important at the time of dealing with multi-dimensional seismic data. In this scenario, the common assumption of a superposition of a few plane waves is doomed to failure. Windowing can be used as a way of validating the aforementioned model. However, we have preferred an alternative procedure where sparseness is not invoked. It is true that both the MWNI and HRFT lead to very similar algorithms. However, in the HRFT approach, the amplitude of the Fourier Transform, $|X_k|^2$, plays the role of a data dependent diagonal regularization matrix as shown in equation (3.2.37). In the present formulation (MWNI), on the other hand, an estimator of the power spectrum of the data is used to capture the spectral variability of the unknown signal. In the next section we propose a procedure to estimate the power spectrum of the unknown data.

The present work does not attempt to invert the non-uniform DFT (Hindriks et. al., 1997). The MWNI implementation utilizes FFTs and therefore an important gain in efficiency is achieved when interpolating data that depends on more than one spatial dimension. For irregularly sample data, data should be regularized first, For example, binning data with smaller bin size; assuming regularly spaced traces and ignoring variations in their true location.

3.2.5 Adaptive estimation of the weighting operator

To obtain the matrix of weights $\mathbf{W}$, in practice, one should know the power spectrum of the complete data P_k^2. Unfortunately, the complete data $\mathbf{x}$ is the unknown of the problem. The latter can be overcome by defining an iterative scheme to *bootstrap* the spectral weights from the data. The numerical implementation uses the modified periodogram of the data (Bingham et al., 1967) so that only the broad shape of the estimated spectrum is kept from the previous iteration. The process can be implemented in both the time domain and the frequency domain. In frequency domain, the estimated DFT coefficient is convolved with DFT of a standard positive and even window w_m (e.g. a hanning window). The result is then squared to obtain the weighting function:

$$P_k^2 = |W_k \circledast \hat{X}_k|^2 \tag{3.2.38}$$

where $\circledast$ denotes the circular convolution. Alternatively, the same end can be reached by

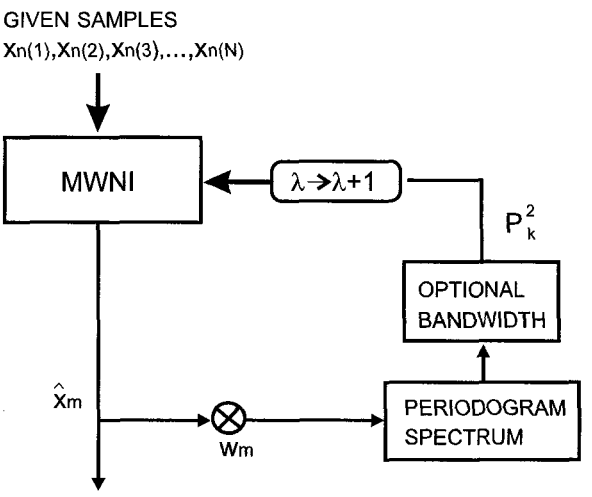

Figure 3.4: Modified periodogram is used to iteratively *bootstrap* the spectral weights from the data.

multiplying the estimated $\hat{\mathbf{x}}$ by the window function

$$h_m = w_m \hat{x}_m \tag{3.2.39}$$

and the weighting function in this case is

$$P_k^2 = |H_k|^2 . \tag{3.2.40}$$

The algorithm is initialized with the band limiting operator with spectral weights $P_k^2 = 1, k \in \mathcal{K}$, once $\mathbf{x}$ is solved the solution is used to recompute P_k^2 using equation (3.2.38) or (3.2.40). Figure 3.4 shows a block diagram of the system describe here.

Alternatively, it is possible to adopt a non-iterative strategy similar to the one proposed by Herrmann (2000) for the computation of the high resolution parabolic Radon transform. The method is well documented in Hugonnet et. al (2001). The power spectrum P_k^2 required to interpolate spatial data at a temporal frequency f can be estimated from the already interpolated data at frequency $f - \Delta f$. Figure 3.5 shows a block diagram illustrate this scheme. Such a scheme is often effective in dealing with situations where the data exhibit a mild degree of spatial alias at high frequencies.

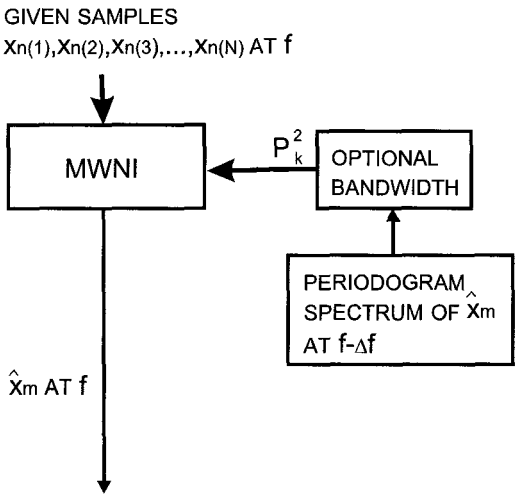

Figure 3.5: The power spectrum P_k^2 required to interpolate spatial data at a temporal frequency f can be estimated from the already interpolated data at the frequency $f - \Delta f$.

In particular, in situations with aliasing produced by non-conflicting dips, the weighting operator computed from the non-aliased low frequencies serves to attenuate the aliasing that might arise at high frequency. The assumption at the time of adopting such a scheme is that the power spectrum of the data at frequency $f - \Delta f$ is similar in shape to the power spectrum of the data at frequency f. This assumption is often valid when Δf is small. This is achieved, in general, by padding the data with zeros before applying the Fourier transform.

3.2.6 1-D reconstruction examples

Reconstruction along one spatial coordinate is illustrated with a synthetic shot gather. Figure 3.6a shows a complete shot gather with 46 traces. The synthetic data were modeled with a ray tracing algorithm for laterally invariant media; the AVO (Variation of Amplitude with Offset) effect is added using Shuey's equation (Shuey, 1985). A total of 18 traces were removed from the original data including some near-offset traces (Figure 3.6b). The incomplete data set is used as the input to our reconstruction algorithm. The data set is first transformed to the temporal frequency domain. The reconstruction is then performed along the spatial coordinate (receiver position) for each temporal fre-

quency. Figure 3.6c shows the reconstruction using the MWNI algorithm introduced in this paper. The modified periodogram was used to iteratively estimate the matrix of weights. The reconstruction fills all gaps including near offset traces. The reconstruction error is portrayed in Figure 3.6d. For comparison, we also tried to reconstruct the data using the Minimum Norm Interpolation (MNI) algorithm. The reconstructed data and the reconstruction error panel are shown in Figures 3.6e and 3.6f. Numerical experiments have found that the MNI algorithm has difficulties at the time of interpolating large gaps. For the MNI method a frequency dependent bandwidth is utilized. The maximum wavenumber at frequency f is estimated using the formula $k_{\max} = f/V_{\min}$, where $V_{\min}$ is the minimum apparent velocity in the data (Duijndam et al., 1999).

Figure 3.7 shows the comparison of spectral weights P_k^2 at the temporal frequency component $f = 23\,\text{Hz}$ for both methods (MNI and MWNI). Figure 3.7a shows the constant weighting function used by the MNI method. Figure 3.7b portrays the power spectrum of the incomplete data (zeros were placed at missing positions). These are also initial weights utilized in the MWNI method. Figures 3.7c and 3.7d show the spectral weights after the second iteration and the sixth (final) iteration, respectively. The spectrum of the final estimate of the interpolated data is portrayed in Figure 3.7e. Finally, the power spectrum of true (complete) data is displayed in Figure 3.7f. There is good agreement of the spectral signatures of the interpolated and original data.

Figure 3.8 shows a 1-D synthetic example of MWNI, HRFT and MNI methods in presence of noise. Figure 3.8a shows a synthetic ray tracing modeled shot gather with a small amount of random noise. Total 18 traces are removed from the shot and the incomplete shot gather (Figure 3.8b) is used to test reconstruction algorithms. Figure 3.8c shows the reconstruction using the MWNI algorithm. The modified periodogram (equation 3.2.38) was used to iteratively estimate the matrix of weights. The reconstruction error is portrayed in Figure 3.8d. For comparison, we also tried to reconstruct the data using the HRFT algorithm and the MNI algorithm. The MNI algorithm has difficulties when interpolating large gaps. The MWNI and HRFT algorithms both managed to retrieve comparable interpolation results. However, numerical experiments have shown that the HRFT tends to produce spectral models that are too sparse and tends to produce large interpolation errors when dealing with data that do not fit the sparse spectral model

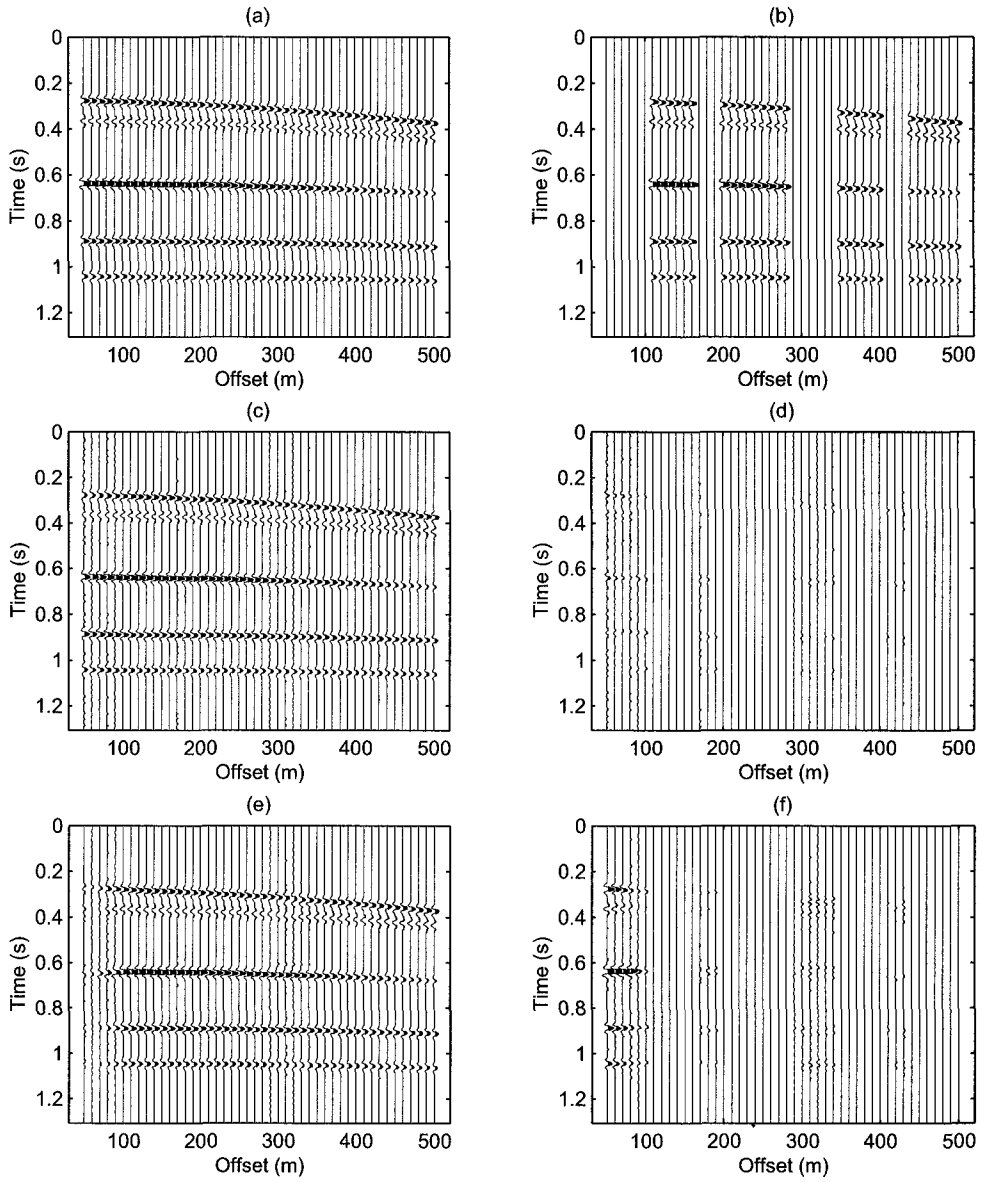

Figure 3.6: 1-D synthetic example of MWNI and MNI methods. (a) Original synthetic shot gather. (b) Incomplete shot gather obtained by removing 19 traces from the complete shot gather in (a). (c) Reconstruction using the MWNI algorithm. (d) Reconstruction error after interpolation with the MWNI method. (e) Reconstruction using MNI. (f) Reconstruction error after interpolation with the MNI method.

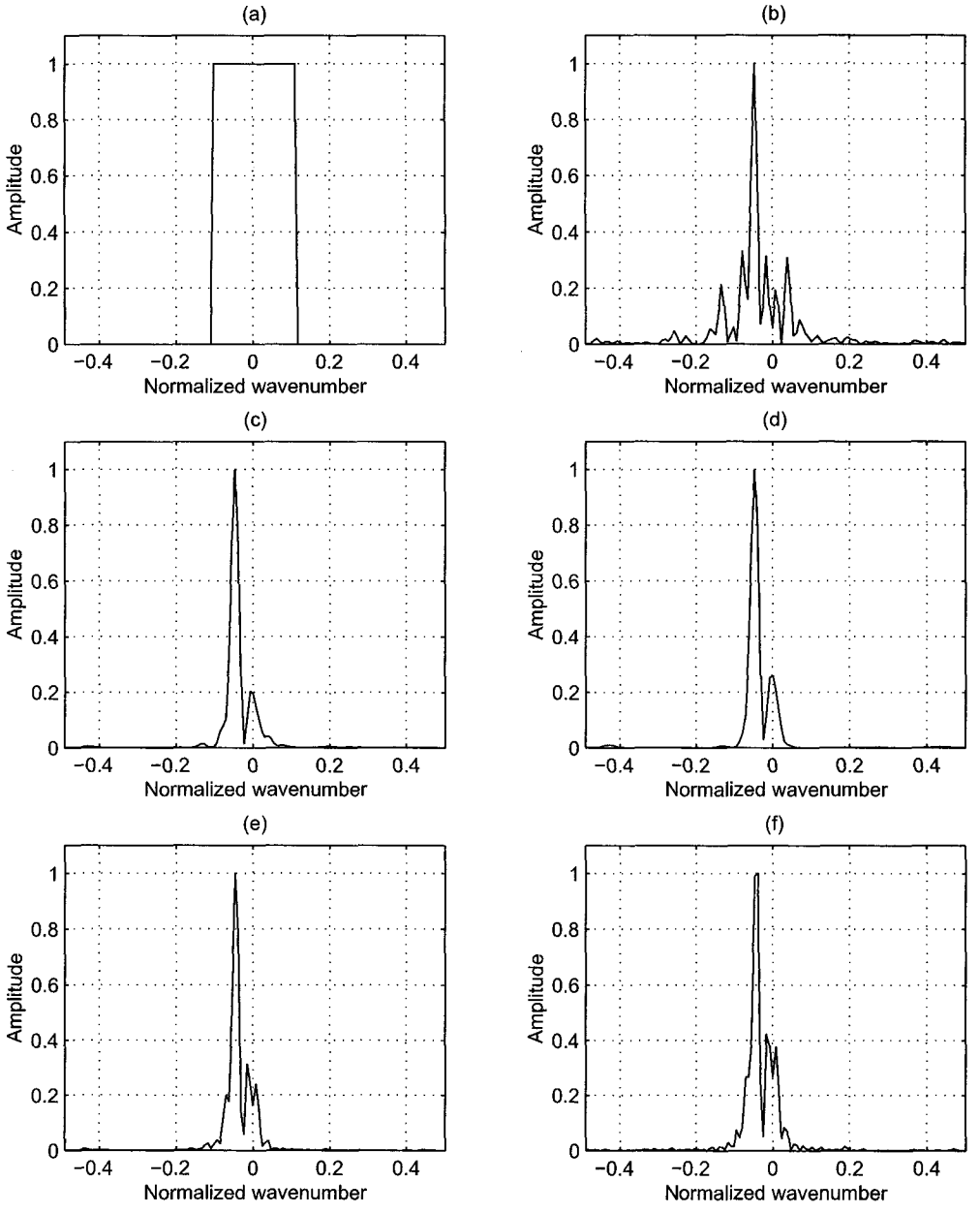

Figure 3.7: Analysis of the spectral weights P_k^2 at frequency component $f = 23$ Hz. (a) Unitary spectral weights used by the MNI method. (b) Power spectrum of the incomplete data, missing samples were filled in with zeros. (c) Spectral weights at the second iteration of the MWNI method. (d) The weighting function at the last iteration of the MWNI method. (e) The spectrum of reconstructed data using MWNI. (f) The spectrum of the original (complete) data.

(seismic events with curvature in $t - x$).

Figure 3.9 compares the reconstructed power spectrum at the temporal frequency component $f = 15.6\,\text{Hz}$ for all the aforementioned methods (MWNI, HRFT and MNI). Figure 3.9a shows the power spectrum of the reconstructed data using the MWNI method. Figure 3.9b portrays the power spectrum of the reconstructed data using the HRFT approach. The spectrum of the reconstructed data using MNI method is portrayed in Figure 3.9c. Finally, the power spectrum of the true (complete) data is displayed in Figure 3.9d. There is good agreement of the spectral signatures of the interpolated and original data in Figures 3.9a and 3.9d. The spectrum obtained using the HRFT approach (Figure 3.9b) is better than the spectrum obtained using the MNI method (Figure 3.9c), however, as mentioned before interpolation with the HRFT tends to produce spectral estimates that are too sparse.

The interpolation of a real marine shot gather using the MWNI method is portrayed in Figure 3.10. Figure 3.10a shows a window of incomplete data from the original shot gather. The interpolated data at twice the original sample rate is portrayed in Figure 3.10b. In this example, spectral weights are determined using the non-iterative scheme described in section (3.2.5). The same scheme is utilized in all remaining examples.

3.3 Multi-dimensional MWNI

3.3.1 N-D MWNI algorithm

The 1-D MWNI algorithm (Liu and Sacchi, 2001; Liu and Sacchi, 2003) can be extended to higher dimensional algorithms using the properties of Kronecker product of matrices (Davis, 1979). Let $\underset{\sim}{\mathbf{A}}$, $\underset{\sim}{\mathbf{B}}$, $\underset{\sim}{\mathbf{C}}$, $\underset{\sim}{\mathbf{D}}$ be $n \times n$ matrices and let $\otimes$ denote the kronecker product. Then

$$(\underset{\sim}{\mathbf{A}} \otimes \underset{\sim}{\mathbf{B}})^T = \underset{\sim}{\mathbf{A}}^T \otimes \underset{\sim}{\mathbf{B}}^T \tag{3.3.1}$$

$$(\underset{\sim}{\mathbf{A}} \otimes \underset{\sim}{\mathbf{B}})(\underset{\sim}{\mathbf{C}} \otimes \underset{\sim}{\mathbf{D}}) = \underset{\sim}{\mathbf{A}}\underset{\sim}{\mathbf{C}} \otimes \underset{\sim}{\mathbf{B}}\underset{\sim}{\mathbf{D}} \tag{3.3.2}$$

$$(\underset{\sim}{\mathbf{A}} \otimes \underset{\sim}{\mathbf{B}})^{-1} = \underset{\sim}{\mathbf{A}}^{-1} \otimes \underset{\sim}{\mathbf{B}}^{-1}. \tag{3.3.3}$$

If $\mathbf{a}$ denotes lexicographic ordering of the elements of $\underset{\sim}{\mathbf{A}}$ into a vector and $\underset{\sim}{\mathbf{D}} = \underset{\sim}{\mathbf{B}}\underset{\sim}{\mathbf{A}}\underset{\sim}{\mathbf{C}}$, then

$$\mathbf{d} = (\underset{\sim}{\mathbf{C}}^T \otimes \underset{\sim}{\mathbf{B}})\mathbf{a}. \tag{3.3.4}$$

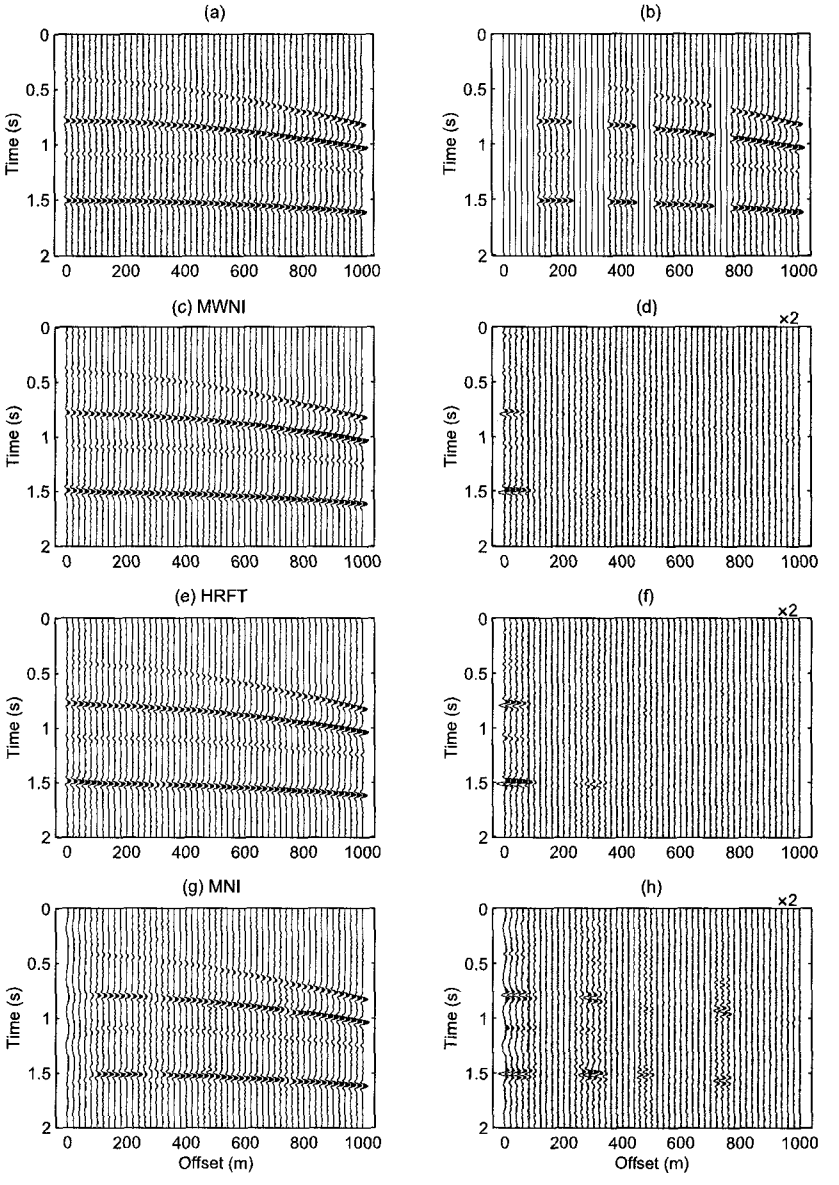

Figure 3.8: 1-D synthetic example of MWNI, HRFT, and MNI methods in the presence of noise(a) Original synthetic shot gather. (b) Incomplete shot gather obtained by removing 18 traces from the complete shot gather in (a). (c) Reconstruction using the MWNI algorithm. (d) Reconstruction error after interpolation with the MWNI method. (e) Reconstruction using the HRFT approach. (f) Reconstruction error after interpolation with the HRFT method. (g) Reconstruction using MNI. (h) Reconstruction error after interpolation with the MNI method. Error panels were multiplied by 2 for better visualize differences.

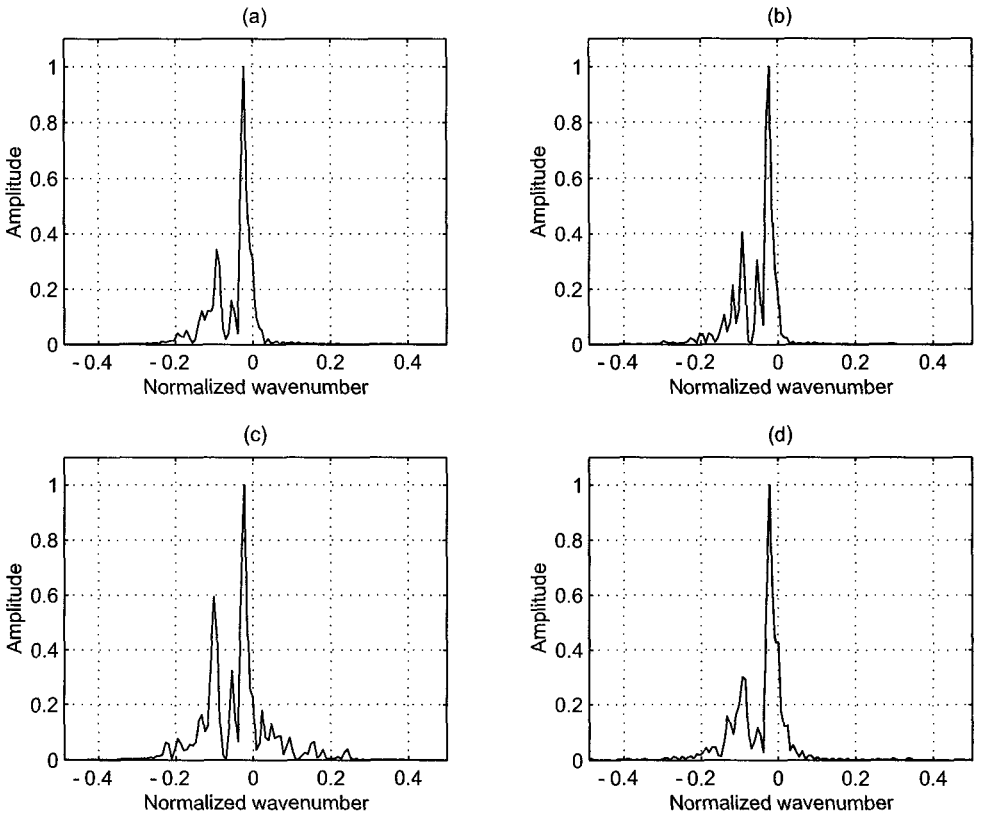

Figure 3.9: Comparison of the reconstructed power spectrum at frequency component $f = 15.6$ Hz for MWNI, HRFT and MNI Methods. (a) Power spectrum of the reconstructed data using the MWNI method. (b) Power spectrum of the reconstructed data using the HRFT approach. (c) Power spectrum of the reconstructed data using the MNI method. (d) Power spectrum of the original (complete) data.

For example, we assume that the matrix $\underset{\sim}{\mathbf{A}}$ represents 2-D seismic data with its columns as the first dimension and rows as the second dimension. Applying the 2-D Fourier transform to the matrix is to apply the DFT to both columns and rows of the matrix x, the result is

$$\hat{\underset{\sim}{\mathbf{A}}} = \underset{\sim}{\mathbf{F}}_1 \, \underset{\sim}{\mathbf{A}} \, \underset{\sim}{\mathbf{F}}_2^T \tag{3.3.5}$$

where $\hat{\underset{\sim}{\mathbf{A}}}$ denotes the 2-D Fourier transform of $\underset{\sim}{\mathbf{A}}$, $\underset{\sim}{\mathbf{F}}_1$ and $\underset{\sim}{\mathbf{F}}_2$ denotes DFT matrices along the first and the second dimensions respectively. According to equation (3.3.4) and (3.3.5), if let we denote $\mathbf{a}$ lexicographic ordering of the elements of $\underset{\sim}{\mathbf{A}}$, then

$$\hat{\mathbf{a}} = (\underset{\sim}{\mathbf{F}}_2 \otimes \underset{\sim}{\mathbf{F}}_1)\, \mathbf{a}, \tag{3.3.6}$$

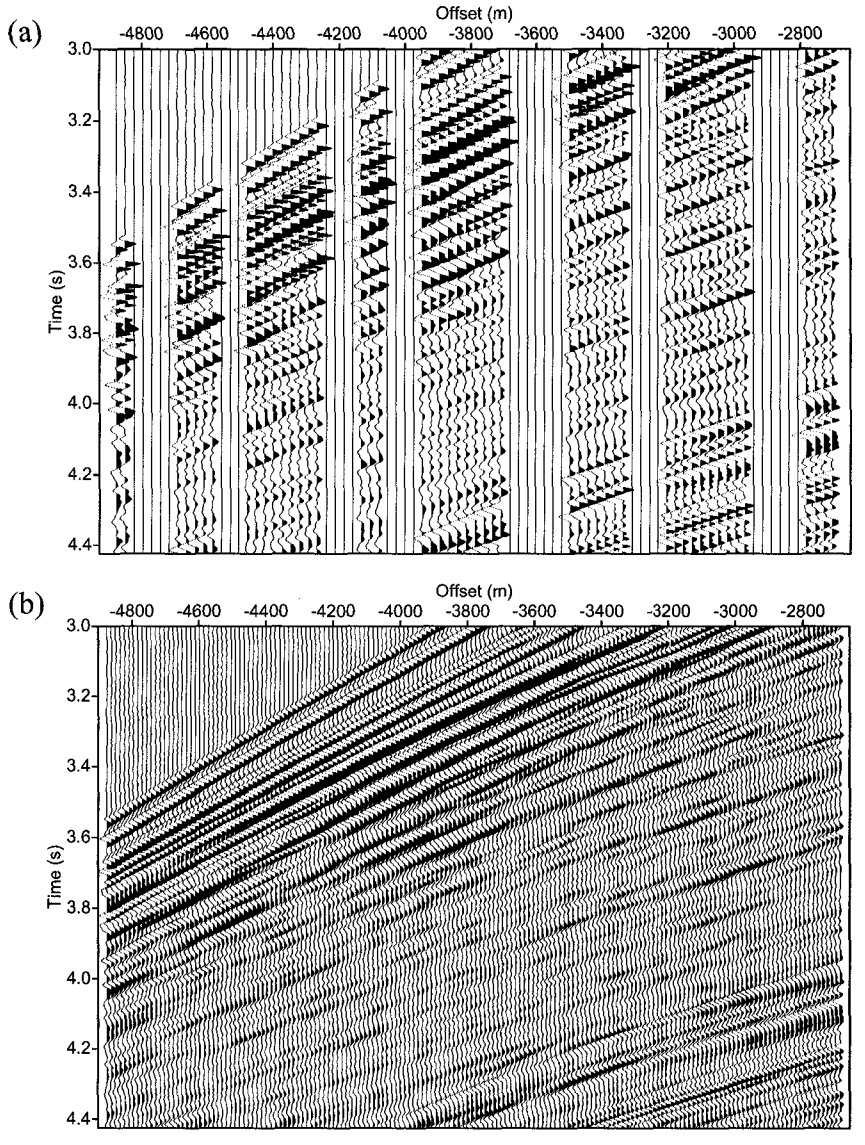

Figure 3.10: 1-D interpolation of a real marine shot gather. (a) Incomplete data from a real marine shot gather. (b) Interpolated data using the MWNI method. Sampling rate is doubled and all gaps has been filled.

where $\hat{\mathbf{a}}$ is lexicographic ordering of the elements of 2-D DFT of $\mathbf{a}$.

Similar to 1-D interpolation, the N-D interpolation is also carried out along the spatial dimensions for each temporal frequency f. We will denote $\mathbf{x}$ the length-M lexicographic ordering of the elements of N-D regularly sampled data $x_1, x_2, x_3, \ldots x_M$. The lexicographic ordering of the elements of N-D observations are given by the length-N vector $\mathbf{y} = [x_{n(1)}, x_{n(2)}, x_{n(3)}, \ldots x_{n(N)}]^T$ where the set $\mathcal{N} = \{n(1), n(2), n(3), \ldots, n(N)\}$ is used to indicate the position of the known samples or observations. We now define the sampling matrix $\underset{\sim}{\mathbf{T}}$ with elements $T_{i,j} = \delta_{n(i),j}$, where δ indicates the Kronecker operator. The N-D sampling problem, therefore, can be represented as a linear system of equations

$$\mathbf{y} = \underset{\sim}{\mathbf{T}}\,\mathbf{x}\,. \tag{3.3.7}$$

The reconstruction/interpolation problem is an inverse problem where from incomplete data $\mathbf{y}$ we attempt to recover the well sampled data $\mathbf{x}$. The MWNI solution of the problem can be obtained by minimizing following objective function

$$J = ||\underset{\sim}{\mathbf{T}}\,\mathbf{x} - \mathbf{y}||^2 + \rho^2 ||\mathbf{x}||^2_{\mathcal{W}}\,, \tag{3.3.8}$$

where $||\cdot||$ stands l_2 norm, ρ^2 is a specified weighting factor controlling the trade off between the data misfit and model norm, and $||\mathbf{x}||_{\mathcal{W}}$ is the DFT-domain weighted norm

$$||\mathbf{x}||^2_{\mathcal{W}} = \underset{\sim}{\mathbf{F}}^H_{ND}\,\underset{\sim}{\mathbf{\Lambda}}^{\dagger}\,\underset{\sim}{\mathbf{F}}_{ND}\,. \tag{3.3.9}$$

where $\underset{\sim}{\mathbf{F}}_{ND} = \underset{\sim}{\mathbf{F}}_N \otimes \underset{\sim}{\mathbf{F}}_{N-1} \cdots \otimes \underset{\sim}{\mathbf{F}}_1$ is the compact notation for the N-D DFT, $\underset{\sim}{\mathbf{F}}^H_{ND} = \underset{\sim}{\mathbf{F}}^H_N \otimes \ldots \underset{\sim}{\mathbf{F}}^H_2 \otimes \underset{\sim}{\mathbf{F}}^H_1$ is the compact notation for the N-D IDFT, and $\underset{\sim}{\mathbf{\Lambda}}^{\dagger}$ is the Moore-Penrose inverse of $\underset{\sim}{\mathbf{\Lambda}}$. Matrices $\underset{\sim}{\mathbf{\Lambda}}^{\dagger}$ and $\underset{\sim}{\mathbf{\Lambda}}$ are diagonal matrices with entries

$$\Lambda_k = \begin{cases} P_k^2 & k \in \mathcal{K}_{ND} \\ 0 & k \notin \mathcal{K}_{ND} \end{cases} \tag{3.3.10}$$

and

$$\Lambda^{\dagger}{}_k = \begin{cases} P_k^{-2} & k \in \mathcal{K}_{ND} \\ 0 & k \notin \mathcal{K}_{ND} \end{cases}\,, \tag{3.3.11}$$

where ${P_k}^2$ are spectral domain weights with support and shape similar to the lexicographic ordering of the elements of N-D power spectrum of the data to interpolate and

$\mathcal{K}_{ND}$ denotes indexes of pass-band of the data. It can be show that solution of minimizing the cost function in (3.3.8) can be numerically achieved by using the CG method to solve

$$\underset{\sim}{\mathbf{T}}\,\underset{\sim}{\mathbf{F}}_{ND}^{H}\,\underset{\sim}{\Lambda}^{1/2}\,\mathbf{z} \approx \mathbf{y} \tag{3.3.12}$$

where

$$\mathbf{z} = \underset{\sim}{\Lambda}^{\dagger 1/2}\,\underset{\sim}{\mathbf{F}}_{ND}\,\mathbf{x} \tag{3.3.13}$$

and stop the algorithm when a maximum number of iterations is reached or a desired misfit is achieved.

3.3.2 Multi-dimensional MWNI of seismic wavefield

The MWNI method is similar to band limited data reconstruction that makes assumption that seismic data to be reconstructed is band limited in the wavenumber domain. In the 2-D seismic survey, any seismic trace in the prestack volume is a member of CSP (common shot panel), CRP (common receiver panel), CMP (common midpoint panel), and COP (common offset panel) as depicted in Figure 2.8 and prestack seismic data are often band limited in multiple domains. A 2-D MWNI algorithm can be used for reconstruction of 2-D seismic data in the shot-receiver or midpoint-offset domain. Indeed, it can be shown that any two coordinates from x_s, x_r, x_m, x_o form a pair of independent vectors $\mathbf{v}_1$, $\mathbf{v}_2$ for the 2-D sampling matrix $\underset{\sim}{\mathbf{V}}$ in equation (2.2.21). Therefore any two coordinates can be chosen as the domain for MWNI interpolation. Obviously, seismic data in the different domains should show different band limited properties, as shown in Figure 2.10, spectrum patterns are different in the shot-receiver and midpoint-offset domain. However, the support of the bandwidth of the spectrum is invariant in the different domains. Of course, 2-D wavefield can be processed by a 1-D reconstruction. For 1-D, band limiting filtering in the shot domain (or the midpoint domain) does not lead to the same results as the application of the band limiting filter in the receiver domain (or the offset domain) (Vermeer, 1990). In addition, 2-D reconstruction of the complete wavefield often yields a better reconstruction compared to 1-D reconstruction. 1-D reconstruction processes each dimension (plane) separately and does not know anything about continuation of structures in the neighboring dimension (plane). Thus 1-D reconstruction can not detect weak

structures that cross different dimensions and there fore is often inadequate for the 2-D wavefield. The idea also applies to higher dimension reconstruction. In general, an N-D reconstruction algorithm should be used to reconstruct N-D wavefield.

The situation is more complicated for 3-D surveys due to additional dimensionality. The poststack 3-D wavefield is a function of time, inline and crossline. The 2-D MWNI algorithm can therefore be used to reconstruct the wavefield along inline and crossline directions. The prestack 3-D wavefield can be represented as a function dependent upon traveltime t and source and receiver locations, i.e. x_s, x_s, x_r, y_r (Vermeer, 1998). There are many types of 3-D field layout (i.e. swath, orthogonal, Flexi-Bin or Bin Fractionation, and Mega-Bin) (Cordsen et al., 2000). In general, 3-D surveys record only a portion of a 5-D wavefield with line spacings that are greater than station spacings. Many different 3-D subsets can be extracted from the acquired under-sampled wavefield such as common source and receiver gathers, common midpoint and offset gathers, common azimuth gather, cross spreads, etc. Figure 3.11 illustrates some of different 3-D subsets. The trace at midpoint M equals the distance to the center O of the cross-spread. The trace at M is a part of a common source, common receiver, common offset, and common azimuth gather.

Therefore, multi-dimensional MWNI can be used to interpolate a 3-D prestack volume in multiple domains which are results of sampling of independent vectors, i.e. x_s, y_s, x_r, y_r. One of the simplest case is a 3-D common azimuth survey. In this case, a 3-D MWNI algorithm can be used for seismic data reconstruction in the common crossline-midpoint, inline-midpoint and offset domain.

In the next section, 2-D MWNI reconstruction examples are shown for both synthetic and real data sets. More synthetic examples are shown in the next chapter where MWNI algorithm is used to reconstruct prestack seismic wavefield for AVA imaging. In chapter 5, 3-D and 4-D reconstruction algorithms are used in field data examples.

3.3.3 2-D reconstruction examples

The effectiveness of the 2-D MWNI method is first demonstrated using the Marmousi data set. The spatial dimensions to interpolate are source and receiver positions. It is important to stress that similar results could be obtained by interpolating in midpoint-offset

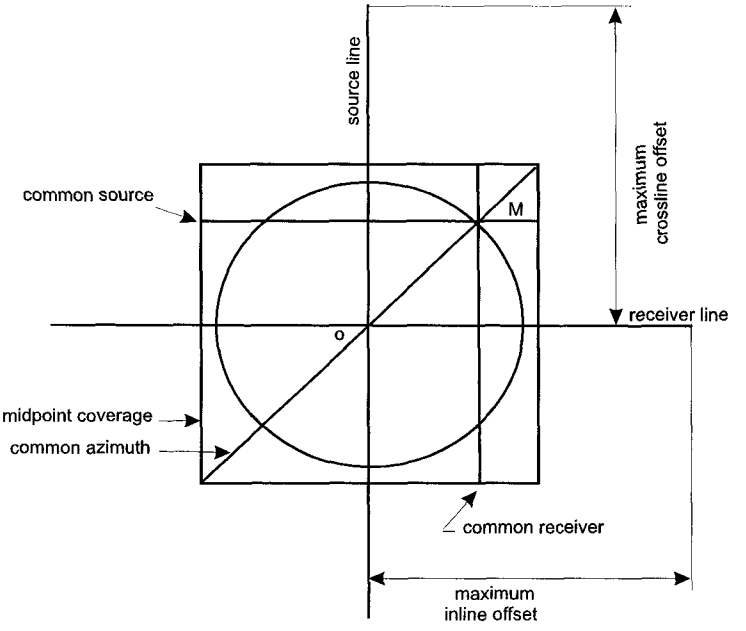

Figure 3.11: Properties of the cross-spread (after Vermeer (1998)). The trace at midpoint M equals the distance to the center O of the cross-spread. The trace at M is a part of a common-source, common-receiver, common offset, and common-azimuth gather.

coordinates. Marmousi data set consists of total 240 shots with 96 receiver positions per shot. The original shots and receivers were sampled every 25 meters. We simulate a survey with shot and receiver intervals of 75 meters such that only 80 shots with 36 traces per shot are assumed to be known and the rest are to be interpolated. The comparison of part of the original and new sampling geometry is shown in Figure 3.12 where the x-marks indicate the positions of the available traces, whereas the dots indicate the positions of the traces to be interpolated. The seismic traces from the new survey are inputs to our interpolation algorithm. We first perform the Fourier transform along the time axis. Reconstruction is then carried at temporal frequencies along two spatial (shot and receiver) coordinates simultaneously. The reconstruction of 240 shots took 41 minutes on a 1 GHz Pentium III computer. All missing traces have been reconstructed. The details of the reconstruction at shot positions 3075 m, 3100 m and 3125 m are shown in Figure 3.13-3.16. Figure 3.13 portrays the complete shots, Figure 3.14 portrays incomplete shots, Figure 3.15 and Figure 3.16 show the reconstructed shot records and reconstruction errors, respectively. The f-k spectra of original, decimated and reconstructed shot gather

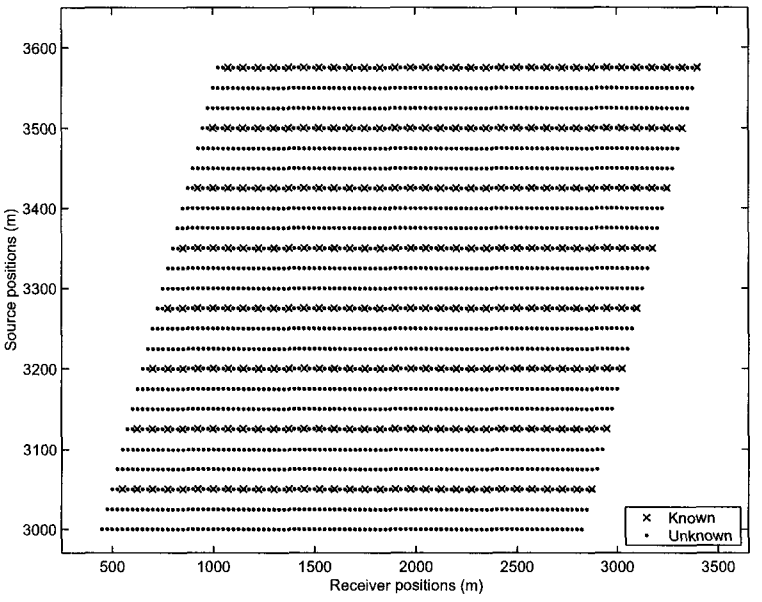

Figure 3.12: Source and receiver position map where the ×-marks indicate the positions of the available traces; the dots indicate the positions to be interpolated.

at 3125 m are shown in Figure 3.17a-3.17c respectively. The decimated shot gather has been filled with zero traces at the missing trace positions. This results in replicas of the spectrum.

We also simulate a survey where 80% traces are randomly removed from the original Marmousi shot records. The comparison of part of the original and new sampling geometry is shown in Figure 3.18 where the x-marks indicate the positions of the available traces, whereas the dots indicate the positions of the traces to be interpolated. 2-D MWNI are carried at temporal frequencies along two spatial (shot and receiver) coordinates simultaneously. All missing traces have been reconstructed. The details of the reconstruction at shot positions 3075 m, 3100 m and 3125 m are shown in Figure 3.19-3.21. Figure 3.19 portrays incomplete shots, Figure 3.20 and Figure 3.21 show the reconstructed shot records and reconstruction errors, respectively. The f-k spectra of original, decimated and reconstructed shot gather at 3125 m are shown in Figure 3.22a, 3.22b and 3.22c, respectively.

We also illustrate the reconstruction of a real 3-D poststack data cube using the 2-D MWNI algorithm. In this case the interpolation is carried out along inline and crossline

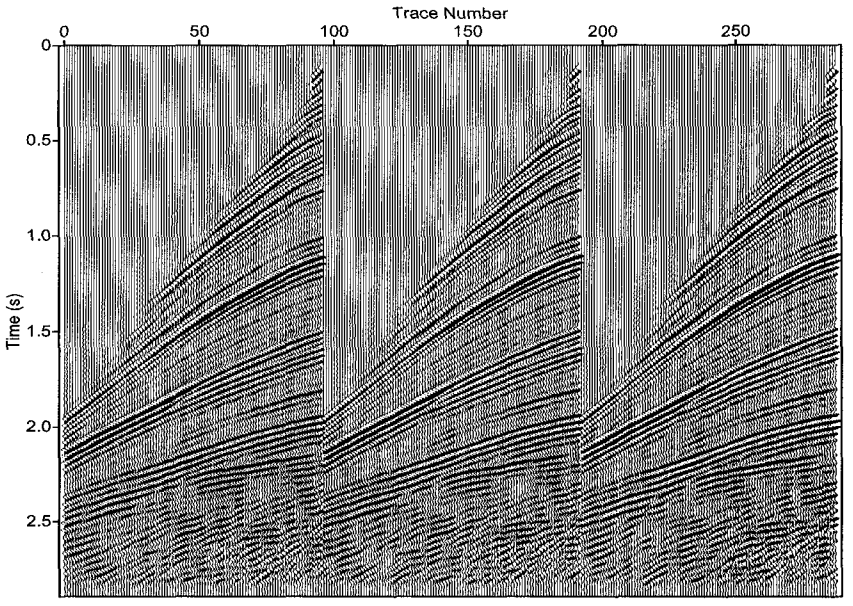

Figure 3.13: Three shots at 3075 m, 3100 m and 3125 m are extracted from the Marmousi data set.

coordinates. Figure 3.23a shows a complete 3-D poststack data cube that consists of 51 inlines and 31 crosslines. The decimated poststack data cube (Figure 3.23b) is obtained by removing every second trace along both inline and crossline directions. The incomplete data cube is used as the input to the MWNI reconstruction algorithm. Figure 3.23c shows the cube after reconstruction. Detailed panels showing true complete data, reconstructed data and reconstruction errors for inline No. 39 and crossline No. 19 are provided in Figures 3.24 and 3.25, respectively. Notice that the proposed interpolation has also attenuated the random noise. The degree of noise attenuation versus fidelity of the reconstruction is regulated by the number of iterations of the CG solver.

3.4 Summary

The seismic data reconstruction problem can be posed as an inverse problem where from incomplete data one seeks the complete wavefield. The problem, however, is ill posed and a prior information should be used to constrain the solution. In this chapter, we have formulated a band limited data reconstruction algorithm that is capable of incorporating

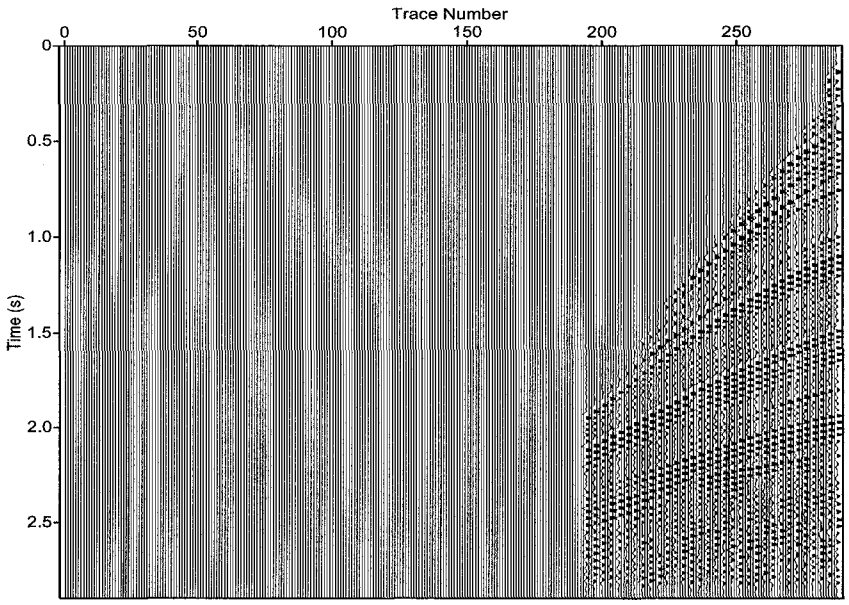

Figure 3.14: Marmousi shots at 3075 m, 3100 m and 3125 m after decimation. The original sampling rates along shot and receiver directions are decimated by a factor of 3.

a priori spectral weights to control the bandwidth and, in addition, the spectral shape of the reconstructed data. The minimum weighted norm interpolation method can be used to interpolate (including increasing sampling rate and gap filling) and extrapolate the multi-dimensional wavefield. The method has been shown to perform better than the standard MNI.

In the presence of additive noise, we have found that a minimum weighted norm, least-squares solution can be efficiently computed using the method of conjugate gradients. It is important to stress that the computational cost of the CG method heavily depends on matrix times vector operations. These operations can be efficiently implemented using the Fast Fourier Transform (FFT). Additional efficiency can be obtained by truncating the number of CG iterations. As pointed out by Hansen (1998) the number of iterations plays a role similar to a trade-off parameter. Consequently, by truncating the number of iterations, additive noise can be attenuated.

The computational cost of the method makes the MWNI attractive for multi-dimensional interpolation.

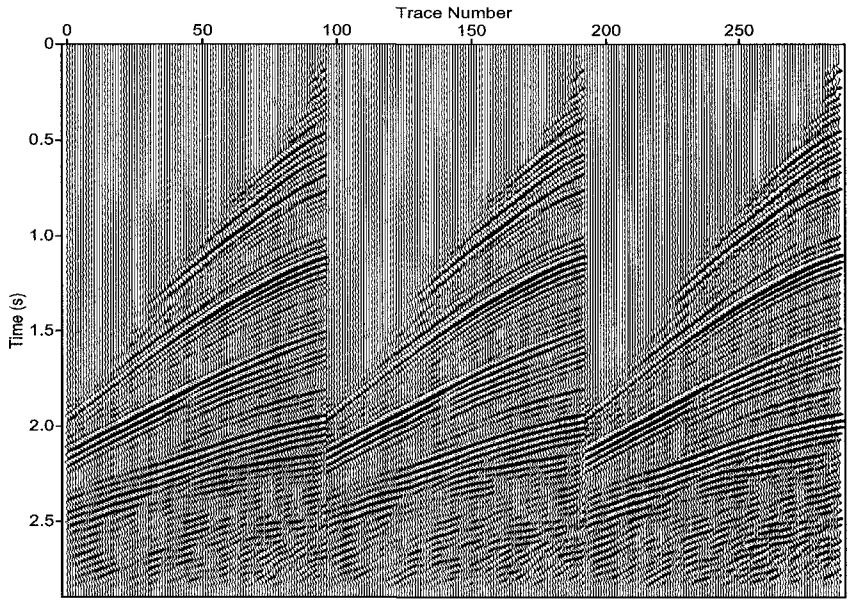

Figure 3.15: Reconstructed shot records at 3075 m, 3100 m and 3125 m using the 2-D MWNI algorithm.

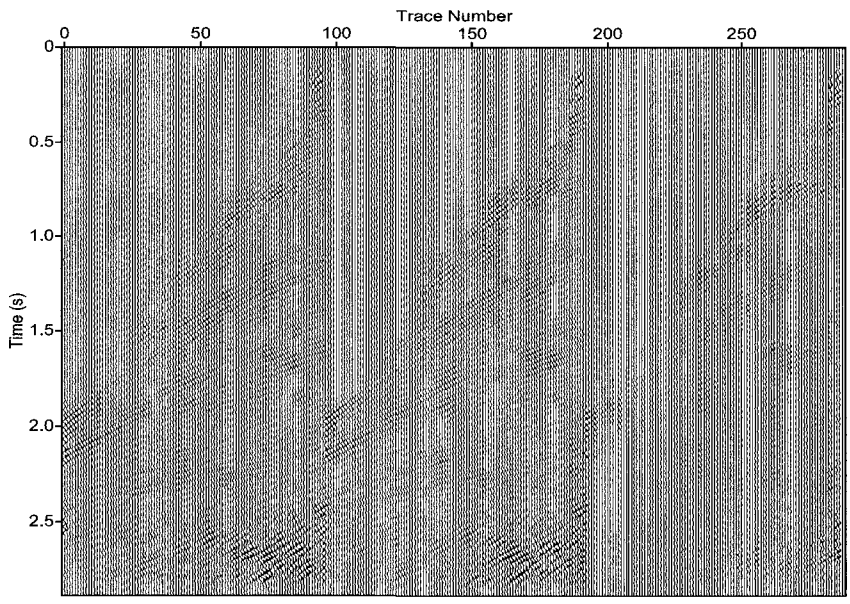

Figure 3.16: Reconstruction errors of the three shot records at 3075 m, 3100 m and 3125 m.

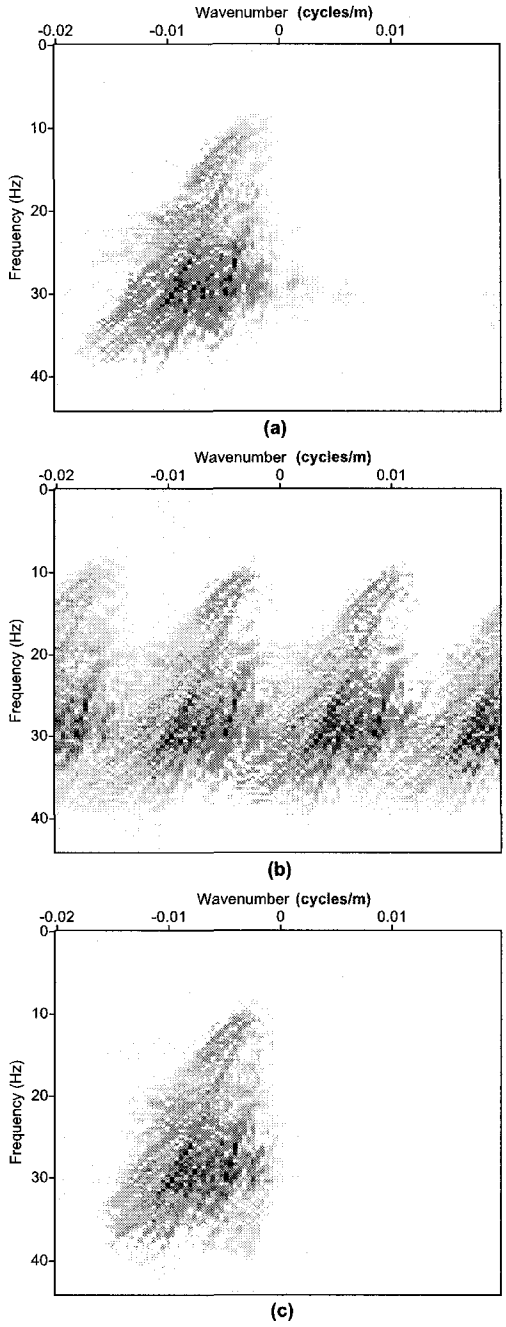

Figure 3.17: (a) The f-k spectrum of the original shot gather at 3125 m. (b) The f-k spectrum of the same shot gather after decimation (Notes the decimated shot data has been filled with zero traces in the missing trace positions). (c) The f-k spectrum of the same shot gather after interpolation.

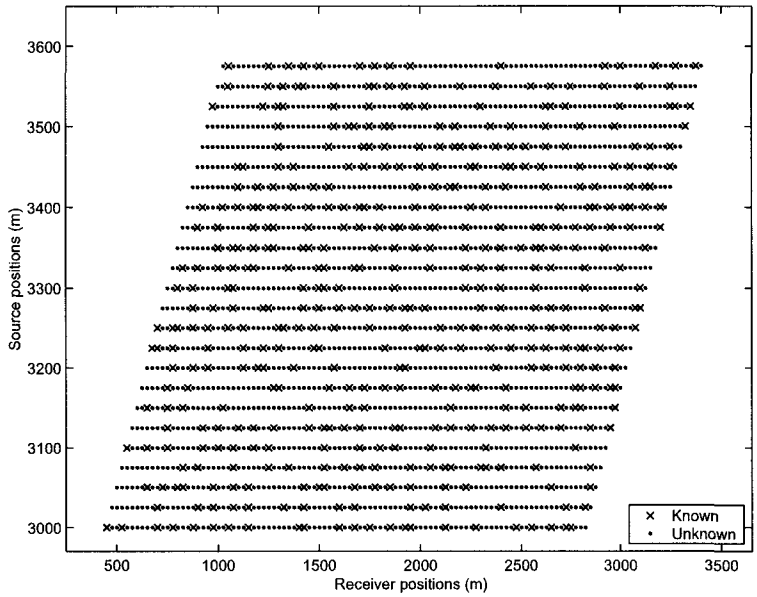

Figure 3.18: Source and receiver position map where the ×-marks indicate the positions of the available traces; the dots indicate the positions to be interpolated.

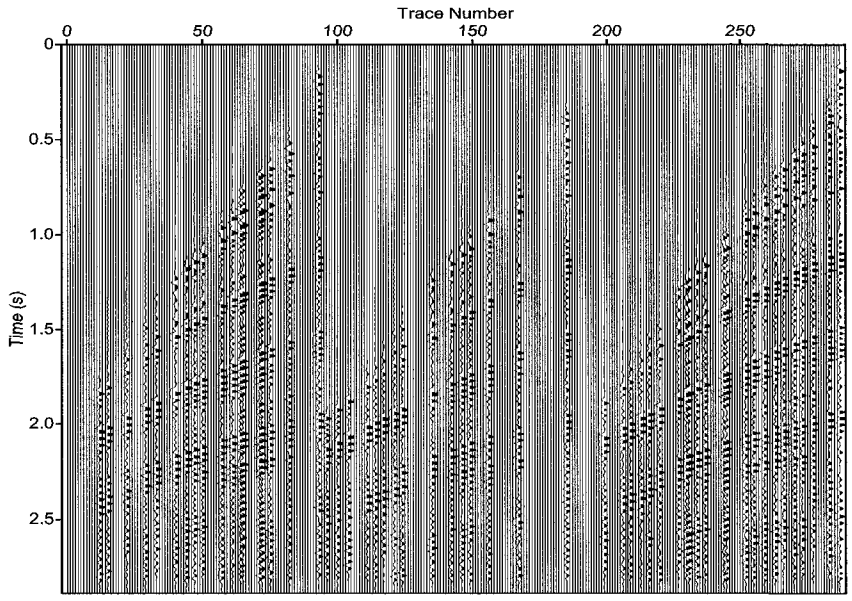

Figure 3.19: Incomplete shots at 3075 m, 3100 m and 3125 m. Total 80% traces have been randomly removed from the original shots (in Figure 3.13).

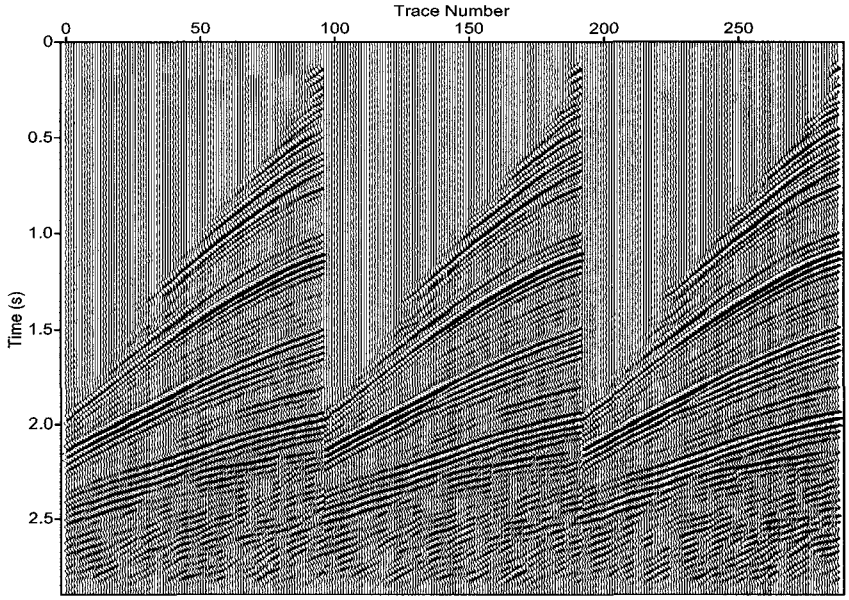

Figure 3.20: Reconstructed shot records at the shot positions of 3075 m, 3100 m and 3125 m using the 2-D MWNI algorithm.

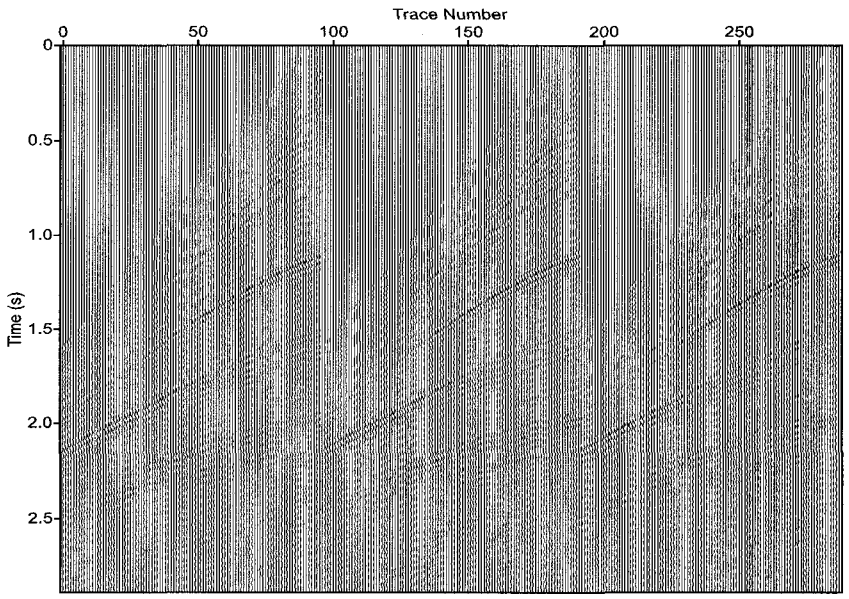

Figure 3.21: Reconstruction errors at the shot positions of 3075 m, 3100 m and 3125 m.

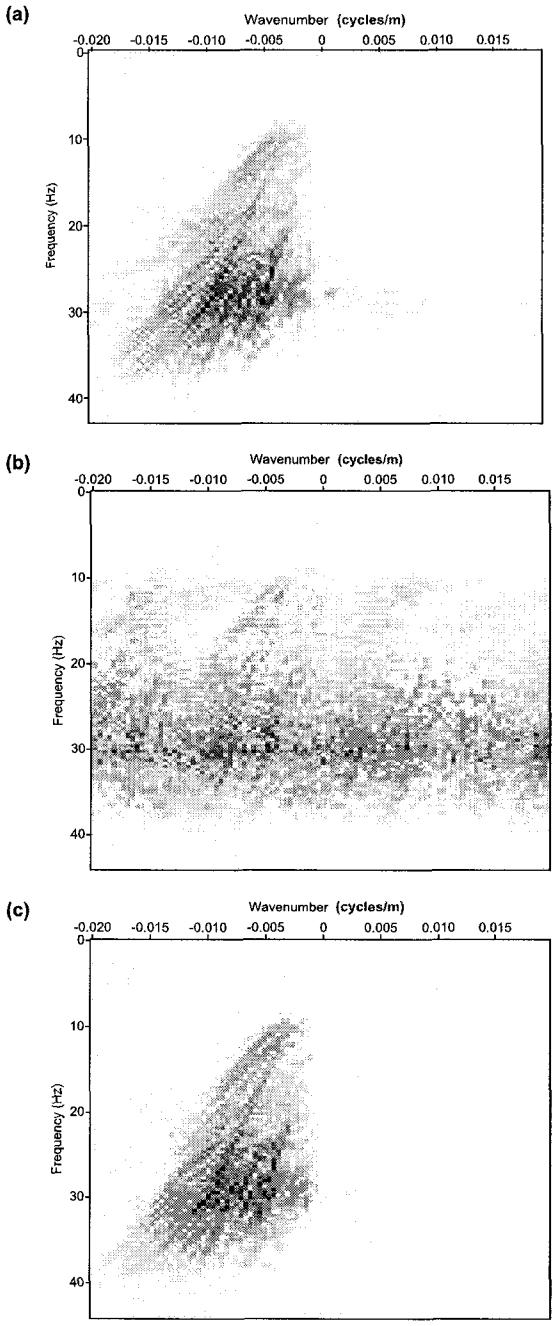

Figure 3.22: (a) The f-k spectrum of the original shot gather at 3125 m. (b) The f-k spectrum of the same shot gather after removing 80% traces. (c) The f-k spectrum of the same shot gather after interpolation.

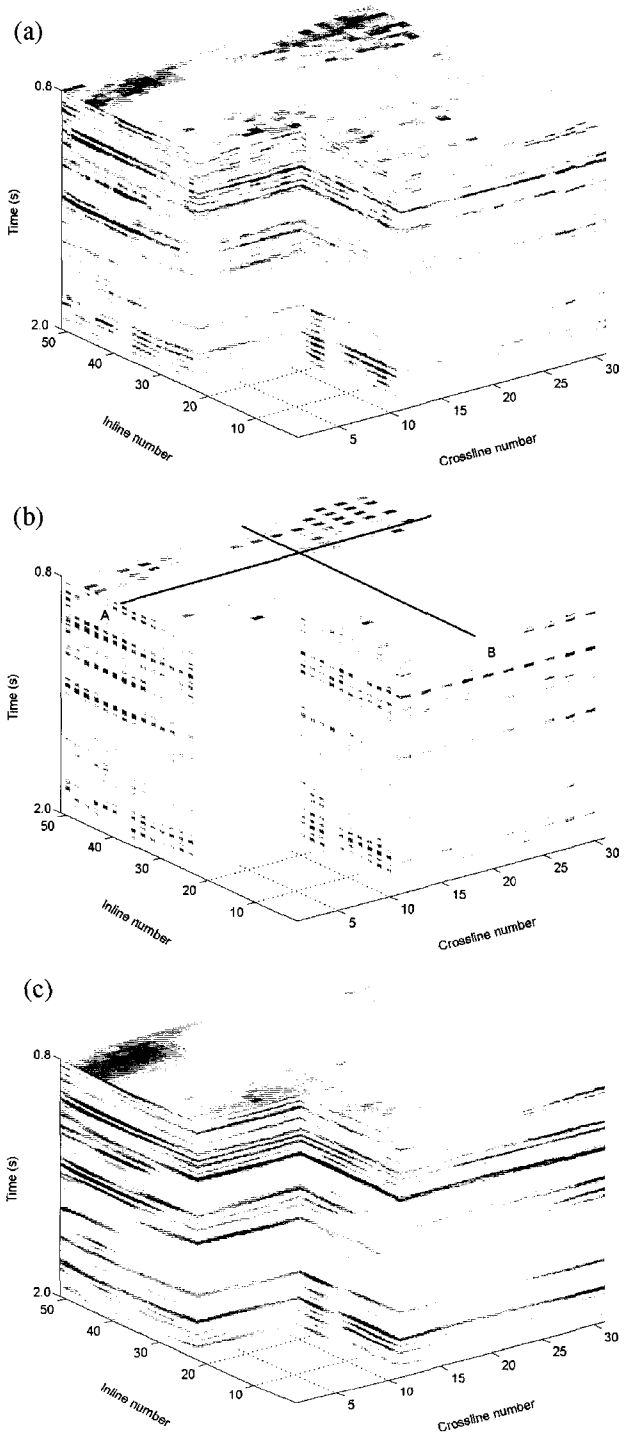

Figure 3.23: (a) A complete 3-D poststack data cube. (b) Decimated cube; every second line is removed. (c) Reconstructed cube using the MWNI method.

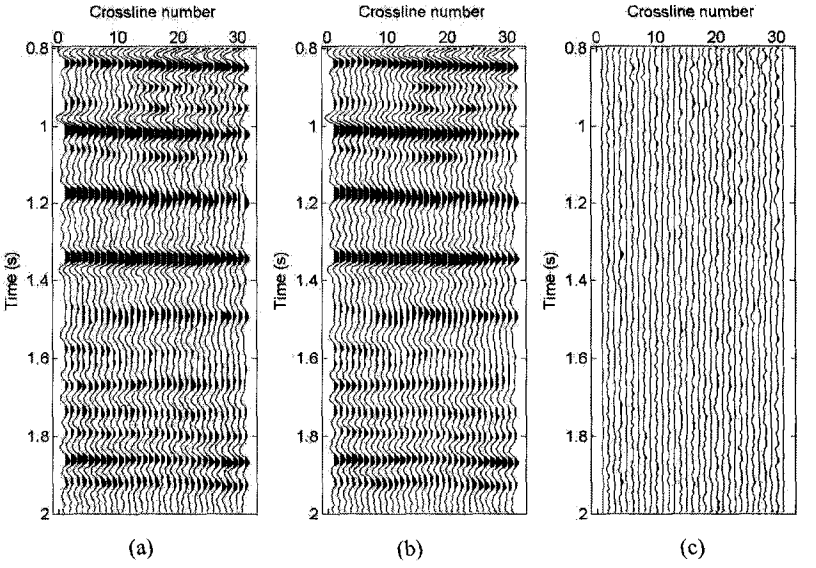

Figure 3.24: (a) Original data along the inline No. 39 (marked as line A in Figure 3.23). (b) Reconstructed data using the MWNI method. (c) Reconstruction error.

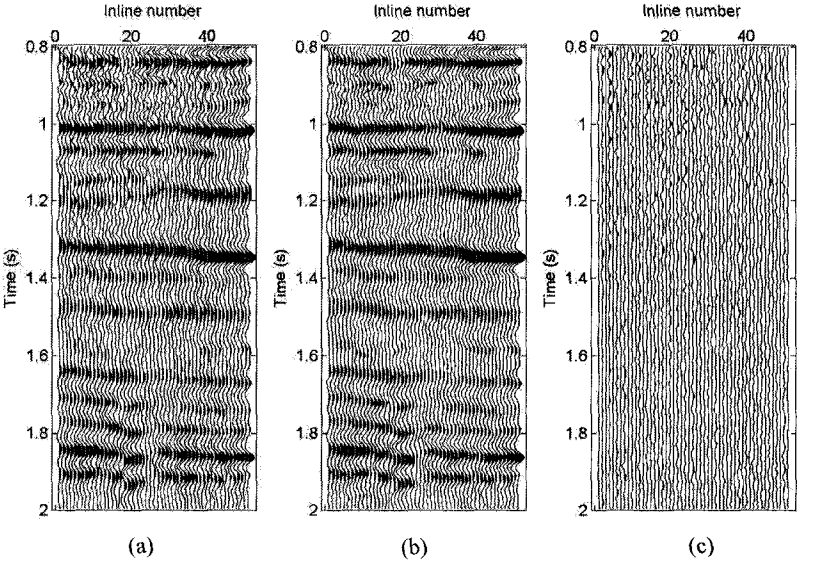

Figure 3.25: (a) Original data along crossline No. 19 (marked as line B in Figure 3.23). (b) Reconstructed data using the MWNI method. (c) Reconstruction error.

Chapter 4

2-D/3-D wavefield reconstruction for AVA imaging

Seismic data are often sparsely and irregularly sampled along spatial coordinates. This produces problems for multi-channel processing techniques which often require regular and dense sampling. Imaging for AVO or AVA analysis is a motivating example to demonstrate the problem. One way to solve this problem is to interpolate prestack seismic wavefield before AVA imaging as discussed in the introduction chapter of this thesis. In this chapter, some aspects of AVA imaging is briefly discussed. The effectiveness of MWNI interpolation strategy is then tested at the time of reconstructing data for 2-D/3-D wave equation AVA imaging (Mosher et al., 1997; Prucha et al., 1999).

4.1 Wave equation AVA imaging

4.1.1 Introduction

Wave equation AVA imaging can be seen as one of the steps in the process of prestack seismic inversion. Seismic inversion has the goal of prediction of rock and fluid properties from seismic data. It is an essential tool in the petroleum industry for hydrocarbon detection. Traditional poststack inversion methods involve stack followed by inversion, allowing only the estimation of acoustic impedance, which is not sufficient for estimating fluid content (Russell, 2003). The AVO method allows us to simultaneously estimate V_p, V_s, and ρ, thus inferring fluid and/or lithology indicators. The AVO/AVA method is traditionally applied to NMO corrected prestack CDP gathers. To apply AVO/AVA tech-

nique to the case where reflectors have dips or structural complexity, prestack migration (i.e. the wave equation AVA imaging method) can be used to produce migrated data for AVA analysis .

A step-wised inversion strategy based on the primary wavefield representation has been proposed by Berkhout and Wapenaar (Berkhout and Wapenaar, 1990) to invert for subsurface properties. The inversion process consists of three stages:

- Surface related preprocessing
- Reflectivity imaging
- Target-related postprocessing

The first stage involves the surface related preprocessing, the output of which can be considered as deconvolved 'primary' data that have been recorded on a non-reflecting, homogeneous data acquisition surface. For example, non-primary reflection events such as surface related multiple and surface wave are considered to be noise and will be suppressed during this stage.

The second stage requires knowledge of a subsurface macro model which may be inferred from preprocessed data or some heuristic relations. The process involves back-propagating the multi-offset surface wavefield into the subsurface reflector where the angle dependent reflectivity is estimated. Wave equation AVA imaging can be used to produce the angle dependent reflectivity (Prucha et al., 1999). Traditionally, seismic imaging by (time or depth) migration aims at producing a subsurface reflector map by back-propagating the surface wavefield. The amplitude information in the reflector map does not necessarily provide quantitative information about the reflection strength. The objective of seismic imaging for AVA analysis is both structure imaging and recovery of angle-dependent reflection coefficients. In other words, in addition to a structure map of subsurface, the amplitude information of the output of seismic imaging by migration should carry qualitative information about relative reflection strength which is related to the incidence angle and physics parameters at reflecting interface. These type of migration methods are often referred to as true-amplitude migration.

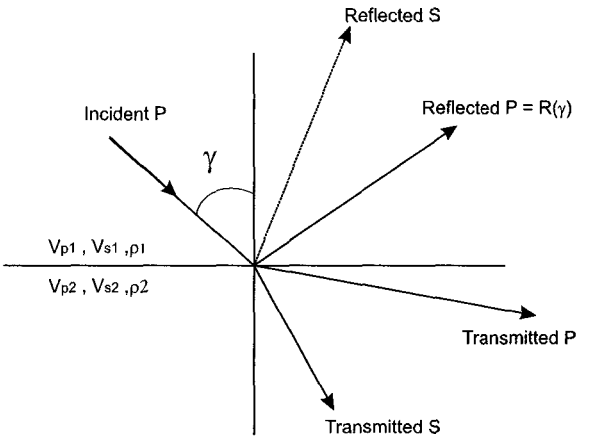

Figure 4.1: Energy partition for a compressional wave (P wave) impinging on a plane interface in an elastic continuum at angle γ. Both reflected and transmitted compressional and shear waves result.

In the last stage, the angle dependent reflectivity is inverted to P- and S-velocity and density information (V_p,V_s,ρ) using expression for the angle-dependent reflection coefficients, trend information from the macro model and, if available, crossplots between V_p,V_s,ρ in the target zone. The expression for the angle-dependent reflection coefficients is, in practice, an approximated version of Zoeppritz's equations through various linearization methods, i.e. Shuey linearized equations (Shuey, 1985). Zoeppritz's equations (Aki and Richards, 1980) satisfy boundary conditions for the continuity of normal and tangential stresses and displacements of plane waves at a plane interface between two elastic media halfspaces. Figure 4.1 depicts the energy partition at such an interface. The elastic model conversions between compressional (P) and shear (S) as waves undergo scattering at an interface is the main derive for AVA phenomena. Finally, the velocity and density information in the target zone is then used for estimation of local rock and fluid properties.

The three step procedure is an acoustic version of the seismic inversion scheme (Berkhout and Wapenaar, 1990). For accurate estimation of the shear velocity, elastic inversion (Berkhout and Wapenaar, 1990) has to be carried out which requires seismic data sets that contain both P and S-wave data, such as those acquired with multi-component sources and receivers. However, the majority of seismic data is often recorded simply as a single

component pressure wave. So in practice, P-wave reflection coefficients are used in the vast majority of cases.

4.1.2 Angle domain common image gathers by wave equation methods

This section concerns wave equation migration of compressional waves for angle dependent subsurface reflectivity. The methodology of estimating angle-domain common image gathers will be discussed. In the wave equation migration, the recorded 2-D and 3-D data are first organized in the midpoint-offset ($\mathbf{m} - \mathbf{h}$) domain. The measured data at the surface ($z = 0$) are recursively downward continued using the DSR (double square root) operator (Claerbout, 1985). Once the complete wavefield has been reconstructed within the target volume, an imaging condition is applied to compute the subsurface *structural image* [1]. The aforementioned procedure can be summarized with the following working flow

$$\textbf{Downward Continuation: } P(\omega, \mathbf{m}, \mathbf{h}, z + \Delta z) = \mathcal{DSR}P(\omega, \mathbf{m}, \mathbf{h}, z)$$

$$\textbf{Imaging: } I(\mathbf{m}, z) = \mathcal{I}P(\omega, \mathbf{m}, \mathbf{h}, z)$$

where $\mathcal{I}$ synthesizes the imaging condition as an operator that entails integration over the frequency and offset. The application of the aforementioned method to 3-D migration involves a quite demanding computational task. It is also clear that regularly sampled data along offset and midpoint vectors ($\mathbf{m} = (m_x, m_y)$, and $\mathbf{h} = (h_x, h_y)$) are required. Biondi and Palacharla (1996) presented a reformulation of the DSR operator that is valid for common azimuth data. This method permits to handle 3-D data in a more efficient manner. In this case, the DSR downward operator requires 3-D FFTs rather than 4-D FFTs per frequency slice like the more demanding full DSR operator.

The procedure outlined above is only valid for computing structural images of the subsurface. In order to estimate angle dependent gathers we combine common azimuth DSR downward continuation with a ray parameter domain imaging transformation (Mosher et al., 1997; Prucha et al., 1999; Kuehl, 2002; Kuehl and Sacchi, 2002):

[1] This is the angle independent image that defines the boundaries of reflecting interfaces.

Downward Continuation: $P(\omega, \mathbf{m}, h_x, z) = \mathcal{DSR}_{CA} P(\omega, \mathbf{m}, h_x, z - \delta z)$

Imaging: $I(\mathbf{m}, p_{h_x}, z) = \mathcal{A} P(\omega, \mathbf{m}, h_x, z)\,,$

where $\mathcal{A}$ synthesizes the slant stack operator (summation along lines of constant ray parameter $p_{h_x} = k_{h_x}/\omega$). In the offset wavenumber/frequency domain, the process is the radial trace transform that maps (k_{h_x}, ω) to (p_{h_x}, ω). The radial trace transform is depicted in Figure 4.2.

Spatial interpolation is needed to render data to a form that makes Fourier domain downward continuation applicable. In our examples we have adopted the MWNI method proposed by Liu and Sacchi (2001) to resample the data to a regular geometry before DSR (Common Azimuth) AVA imaging. In Wang et al. (2003), rather than attempting to interpolate the data before migration, Least-squares migration is used to *fit* the migrated image to the observations (recorded traces).

The resulting gathers in the midpoint/offset ray parameter domain can be transformed to angle of incidence by a simple expression (Prucha et al., 1999):

$$p_{h_x} = \frac{2\sin(\theta)\,\cos(\phi)}{c(z, \mathbf{m})}\,,$$

where θ is the angle of incidence, ϕ denotes the structural dip in the in-line direction and $c(z, \mathbf{m})$ the migration velocity. With the aid of the above expression $p-$gathers can be converted to angle gather for subsequent AVA analysis.

4.1.3 True amplitude weighting

Amplitude weighting was applied according to Sava et al. (2001). In the frequency wavenumber domain, these weights are well approximated by a diagonal operator and they are computed by evaluating the Jacobian of the transformation from the temporal frequency (ω) to the vertical wavenumber (k_z), that is $d\omega/dk_z$. Since ray parameter imaging is carried out for a constant offset slowness, the dispersion relation for k_z is expressed as a function of $\mathbf{p}_h$ (Kuehl and Sacchi, 2003):

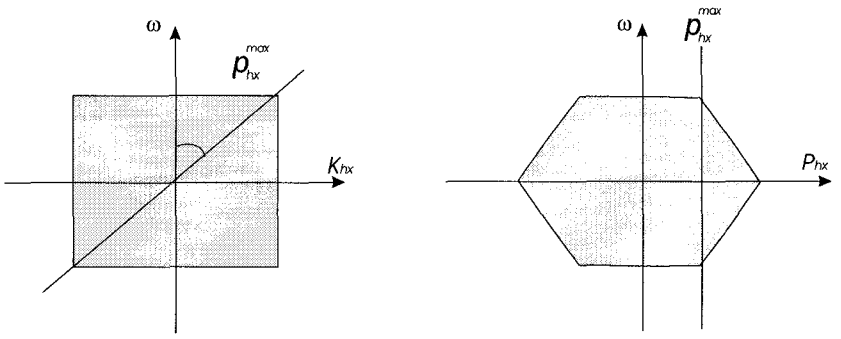

Figure 4.2: The radial trace transform (RTT) maps the $(\mathbf{k}_h, \omega)$ space into the $(\mathbf{p}_h, \omega)$ space (Modified after Kuehl (2002)). Only planes $k_{hy} = 0$ and $p_{hy} = 0$ are shown. The RTT extracts wavefield amplitudes along radial lines in the (k_{hx}, ω) space and maps the result into the (p_{hx}, ω) domain. In practice, the limited offset wavenumber range due to a finite recording aperture and the finite frequency band (shaded area) causes truncation effects in the (p_{hx}, ω) space. The maximum unbiased offset ray parameter is denoted by p_{hx}^{max}. In three dimensions the transformation maps cones in the $(\mathbf{k}_h, \omega)$ space to cylinders in the $(\mathbf{p}_h, \omega)$ domain and vice versa.

$$k_z = k_{sz} + k_{rz} = \sqrt{\left(\frac{\omega}{c}\right)^2 - \frac{|\mathbf{k}_m - \omega \mathbf{p}_h|^2}{4}} + \sqrt{\left(\frac{\omega}{c}\right)^2 - \frac{|\mathbf{k}_m + \omega \mathbf{p}_h|^2}{4}}. \tag{4.1.1}$$

The imaging Jacobian can be shown (Sava et al., 2001) to take the form:

$$\begin{aligned} \mathcal{J} = \left.\frac{d\omega}{dk_z}\right|_{\mathbf{p}_h} &= \left[\frac{dk_z}{d\omega}\right]^{-1}_{\mathbf{p}_h} \\ &= \left[\left(\frac{1}{c} - \frac{c\mathbf{p}_h \cdot \mathbf{p}_h}{4}\right)\left(\frac{\omega}{ck_{sz}} + \frac{\omega}{ck_{rz}}\right) + \frac{c\mathbf{k}_m \cdot \mathbf{p}_h}{4\omega}\left(\frac{\omega}{ck_{sz}} - \frac{\omega}{ck_{rz}}\right)\right]^{-1} \end{aligned} \tag{4.1.2}$$

For horizontal interfaces $k_{sz} = k_{rz} = \frac{\omega \cos\theta}{c}$, where θ is the specular incidence angle, the Jacobian simplifies to (Wapenaar et al., 1999):

$$\mathcal{J} = \left[\left(\frac{1}{c} - \frac{\sin^2\theta}{c}\right)\frac{2}{\cos\theta}\right]^{-1} = \frac{c}{2\cos\theta}. \tag{4.1.3}$$

All involved quantities are understood to be evaluated locally at the target reflector.

4.2 Synthetic examples of MWNI for AVA imaging

In this section, the effectiveness of MWNI strategy is tested at the time of reconstructing data for 2-D/3-D wave equation AVA imaging.

The first example is a 2-D synthetics data set based on a simple, horizontally layered model. As discussed in the introduction of this thesis, for 1-D earth models without any dips, simple techniques, such as geometrical spreading followed by NMO correction, can be used to generate offset (angle) dependent gathers suitable for AVO/AVA analysis. However, the simple data tests provide us more insides on impact of MWNI on migration and AVA analysis on an unevenly sampled data set. The second example is the Marmousi data set. The Marmousi dataset is a quite realistic dataset built on a variable velocity and density model (Marmousi model). However, the complexity of the model makes it difficult to analyse AVA behavior on CIGs. Most of events on CIGs are superpositions of reflection due to many different reflectors. To compare the result with the theoretical AVA, a relatively well-isolated reflector has been picked to demonstrate the benefit of MWNI for migration and AVA imaging. The last example in this section is a common azimuth synthetic dataset based on a simple, horizontally layered model. The data set is used to test the effectiveness of 3-D MWNI algorithm to improve 3-D common azimuth migration or AVA analysis.

4.2.1 2-D Synthetic data examples

Horizontal layered model

We first test our algorithm on a simple, horizontally layered model. The horizontally layered model consists of four reflecting interfaces. The acoustic model parameters in terms of compressional velocities and densities range from 1900 m/s to 2500 m/s and

Velocity (m/s)	Density (g/cm^3)	Thickness (m)
2000	2.25	500
2350	1.6	300
1900	2.3	300
2500	1.7	300
2500	2.0	Half-space

Table 4.1: Parameters for the horizontally layered model with 4 reflecting interfaces. The parameters have been chosen such that the absolute magnitude of the normal incidence reflection coefficient does not exceed 0.1. This model is considered a low contrast medium. Polarity reversals (180° phase changes) in the AVA occur for the first three reflectors. The last reflector exhibits a constant AVA characteristic.

from 1.6 g/cm^3 to 2.25 g/cm^3 , respectively. More details of the model is specified in Table 4.1. All interfaces are well separated. A ray tracing technique is used to generate the synthetic data set. The ray-tracer takes advantage of the fact that, in a stratified medium, the ray parameter is constant for a particular ray. Angle dependent reflection coefficients are modeled with the acoustic reflection coefficients expression:

$$R(\gamma) = \frac{\rho_2 V_2 \cos\gamma - \rho_1 \sqrt{V_1^2 - V_2^2 \sin\gamma}}{\rho_2 V_2 \cos\gamma + \rho_1 \sqrt{V_1^2 - V_2^2 \sin\gamma}}, \tag{4.2.1}$$

where V_1 and V_2 are the velocities, ρ_1 and ρ_2 are the mass densities of the upper and lower half-space, respectively, and γ is the angle of incidence. For interfaces with a change of density only the reflection coefficient is angle independent and equation (4.2.1) is simplified to

$$R(\gamma) = \frac{\rho_2 - \rho_1}{\rho_2 + \rho_1}. \tag{4.2.2}$$

Note that the acoustic reflection coefficients are used in all the synthetic examples in the thesis for mathematic simplicity. However, in dealing with real world data, Zoeppritz's equations or their approximation should be used. The geometrical spreading has been calculated assuming a cylindrical wavefront resulting in a $1/\sqrt{r}$ amplitude scaling, where r is the distance traveled by the ray. Note that transmission losses are neglected in the synthetics.

In Figure 4.3a, we show the CMP data at 750 m which exhibit a clear amplitude variation versus offset (AVO). The offsets for the CMP range from 0 to 1280 m incrementing by 20 m. Figure 4.3b shows the same CMP after randomly removing 90% of the live traces. The incomplete CMPs (total 100) are used as the input for the reconstruction. We first perform the Fourier transform along the time axis. The reconstruction is then carried at temporal frequencies along two spatial (CMP and offset) coordinates simultaneously. The output offset ranges from 0 m to 1200 m for each CMP incrementing by 10 m. Figure 4.3c shows the reconstructed CMP at 750 m using MWNI.

Next, we migrate the complete, incomplete and reconstructed datasets with a wave equation DSR AVA migration algorithm (Prucha et al., 1999). In Figure 4.4a-4.4c, we show migrated ray parameter CIGs at 750 m obtained with the original data, incomplete data and

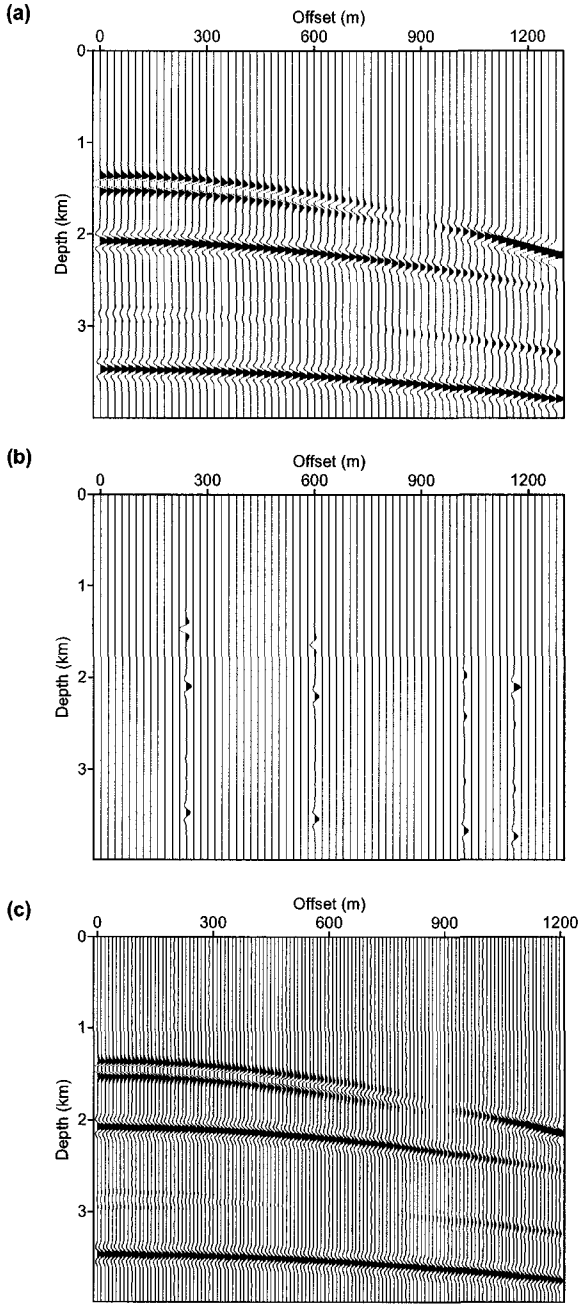

Figure 4.3: (a) CMP gather at 750 m generated by a ray-tracing code. The code models (cylindrical) geometrical spreading but no transmission effects. The offset for the particular CMP ranges from 0 m to 1280 m incrementing by 20 m. (b) The same CMP after randomly removing of 90 % the data. (c) The reconstructed CMP using WMNI, the reconstructed offset ranges from 0 m to 1200 m incrementing by 10 m.

reconstructed data, respectively. In all migrated CIGs, the apparent AVP of the migrated CIG is slightly compromised by finite aperture effects. The wavelet broadening (dispersion) toward high ray parameters seen for the first reflector is explained by the frequency tapering effect inherent in the radial trace transform. In addition, the CIG obtained with the incomplete data appears to be more noisy than the CIGs obtained with the original data and reconstructed data. The latter are overall cleaner and exhibit a smooth AVP.
The AVA curves for the four reflectors from the above CIGs are extracted and portrayed in Figure 4.5a-4.5d. The amplitude picking procedure involves the definition of windows on the CIGs and the determination of the absolute values within these windows. The inverse ray parameter imaging Jacobian $\mathcal{J}^{-1}$ is applied before final AVA plots. Note that since the absolute values have been picked sign changes appear as cusps in the AVA curves. For all four reflectors, AVA curves obtained from the incomplete data is distorted and the AVA curves obtained from the reconstructed data closely match the one obtain ed from the completed data. In addition, AVA curves obtained from the reconstructed and completed data agree with the theoretical AVA trend for a large range of incidence angles except the fact that finite recording aperture effects caused the AVA of all reflectors to eventually taper off to zero.

The above examples demonstrate that when surface wavefield is well sampled, the AVA imaging algorithm gives a reliable AVA estimation in a low contrast layered media. Incomplete sampling (removal of data) introduces errors to both estimated CIGs and pick ed AVA curves. Those errors are often referred to as acquisition footprints noise and can be minimized if a well sampled simulated wavefield (using MWNI algorithm) is used as the input to the migration/inversion algorithm.

4.2.2 The Marmousi data set

In this section, the performance of the 2-D MWNI algorithm is demonstrated with the Marmousi synthetic data set. The Marmousi model is a very realistic and complex model based on a geological profile through the North Quenguela Trough in the Cuanza Basin in Angola (Versteeg, 1993). The model was generated by the French Petroleum Institute, and was released to the public for the purpose of testing migration and velocity estimation techniques.

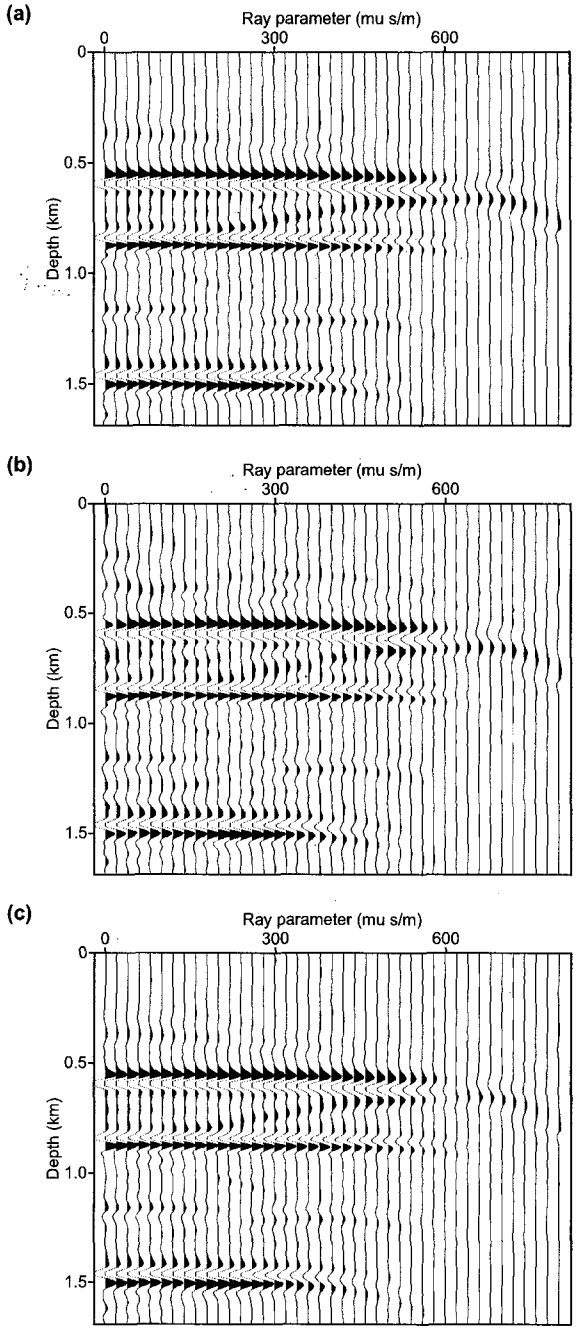

Figure 4.4: (a) Migrated CIG at 750 m of original data. (b) Migrated CIG of incomplete data. (c) Migrated CIG of reconstructed data.

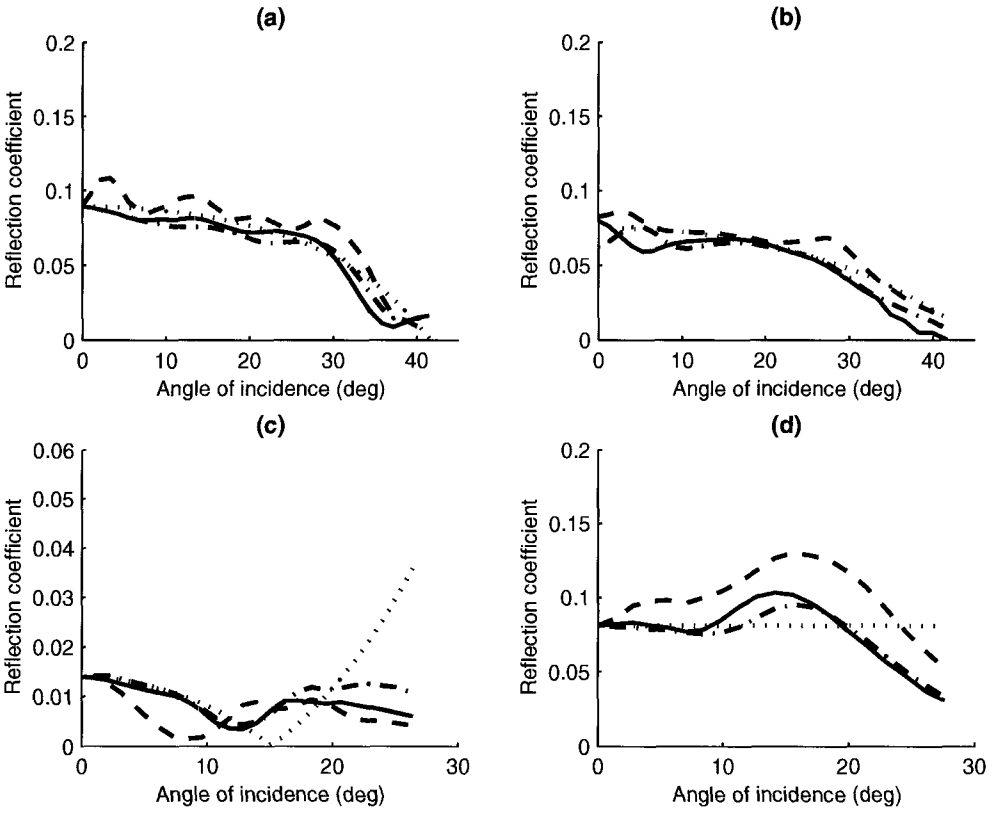

Figure 4.5: (a) Theoretical (Green) and extracted AVA curves from the migrated angle gather for the first reflector (Black: original complete data, Blue: incomplete data, Red: after interpolation). (b) Theoretical and extracted AVA curves for the second reflector. (c) Theoretical and extracted AVA curves for the third reflector. Since the absolute values have been picked sign changes appear as cusps in the AVA curves. (d) Theoretical and extracted AVA curves for the fourth reflector. Note all picked values have been scaled with the inverse of the ray parameter imaging Jacobian for horizontal interfaces.

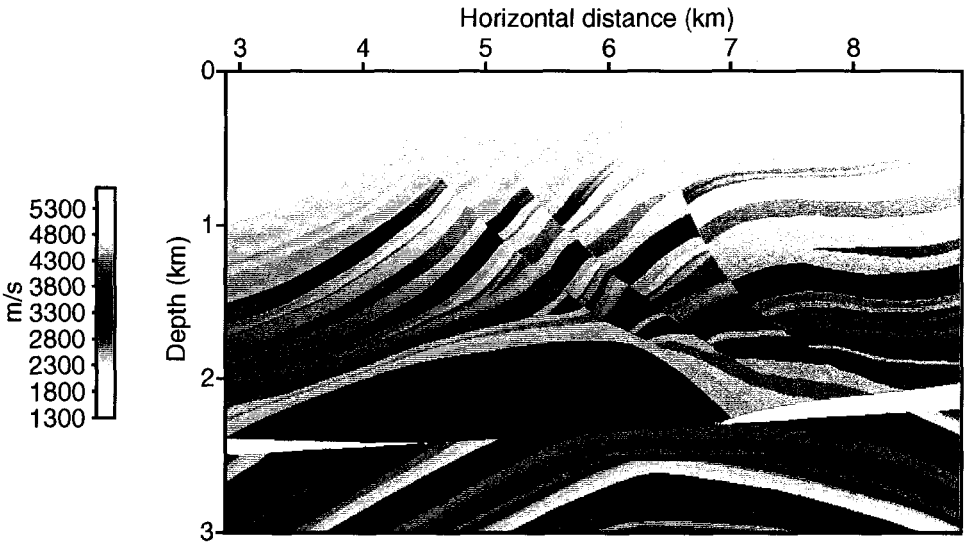

Figure 4.6: The Marmousi compressional velocity field. Velocities range from 1500 to 5500 m/s. The Marmousi model is structurally complex, with many thin layers broken by several major faults and an unconformity surface. The folded carbonate sedimentation series at about 2.5 km form the structural hydrocarbon trap.

According to Versteeg (1994), geologic history underlying the model consists of two distinct phases. The first phase corresponds to a continuous sedimentation of marls and carbonates. These deposits were folded at the end of the sedimentation and then eroded with the erosion surface being flat. The resulting anticlinal structure forms the hydrocarbon trap. The second phase began with the deposition of isopachous saliferous evaporitic series. On this series a clayey-marly series rich in organic matter was deposited and these sediments are followed by deposit of shaly-sandy detrital sediments that are strongly affected by slanting growth faults caused by lateral salt creep due to the overburden pressure. The imaging targets are salt structure related traps and the deeper anticlinal structures.

The Marmousi data set is produced with a marine data acquisition which is simulated using a 2-D acoustic finite-difference modeling, with variations in both acoustic velocity and density (Figure 4.6 and Figure 4.7). The synthetic data set consists of 240 shots with 96 traces/shots. The initial offset is 200 m, the shot and receiver spacing is 25 m. The first shot is at position X = 3000 m, the last shot at X = 8975 m. Two reconstruction examples

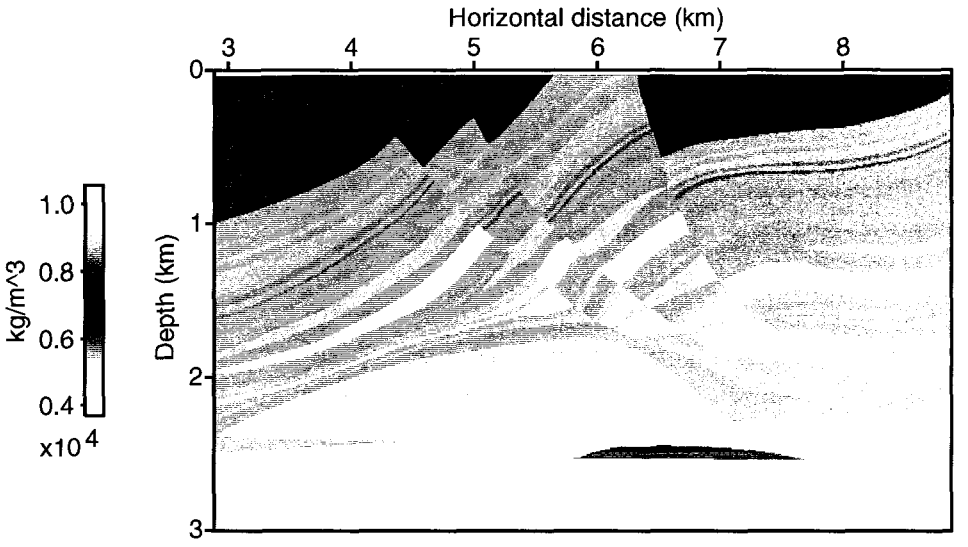

Figure 4.7: The Marmousi density field. The Marmousi data set is based on a variable-velocity and density model making it well suited for acoustic AVP/AVA studies.

on the Marmousi data set are shown in section 3.3.3. In this section, the complete (original), incomplete and reconstructed data sets are further tested with the AVA imaging algorithm. In the first example discussed in the section 3.3.3, a new survey with 75 m shot-receiver sampling interval is simulated. The downsampled (incomplete) wavefield is then used as the input for the MWNI algorithm to reconstruct the complete wavefield. The complete (original), incomplete and reconstructed data sets are migrated with split-step DSR AVA migration algorithm (Prucha et al., 1999). Figures 4.8-4.10 show both the stacked image and migrated CIG at CMP location 7500 m using the three different data sets. The migration with the complete data set yields the stacked image and migrated CIG portrayed in Figure 4.8. The coarse sampling of the decimated wavefield results in severely aliased events in both the stacked image and the CIG (Figure 4.9). In Figure 4.10, we observe that the migration with the reconstructed wavefield yields an overall better stacked image without visible signs of aliasing. The continuity of events in the CIG is also improved.

As discussed before, the complex structure of the Marmousi model makes it difficult to analysis AVA behavior on CIGs. Two criteria are therefore used to guided the process

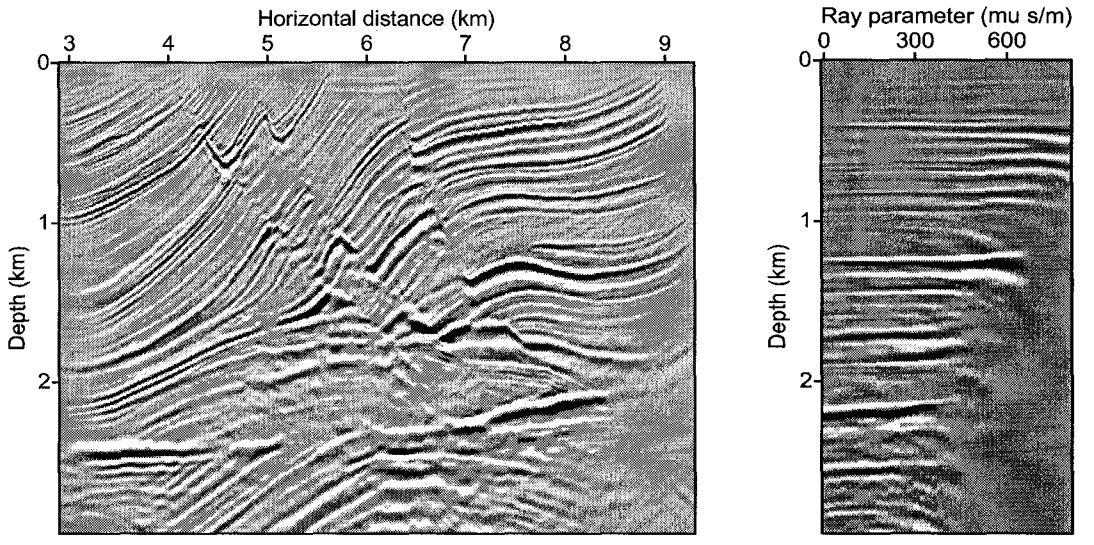

Figure 4.8: Migrated image of the Marmousi model and CIG at CMP location 7500 m. All the data were used in the migration.

of selection of the depth point whose AVA is to be estimated (Kuehl and Sacchi, 2003). First, the depth point should be located in the upper half of the model so as to ensure the sufficiently ray parameter/angle range coverage. Secondly, as events on CIGs are often the superpositions of reflection due to many different reflectors, a relative well isolated reflector should be chosen to compare the inverted AVA to the theoretical AVA of the picked reflection events.

The target reflector is chosen at CMP location 7500 m. The picked target phase in the CIG is the peaks at 880 m depth in Figure 4.8-4.10. In Figure 4.11, the reflection coefficient based on the acoustic approximation shows an increasing trend with the angle of incidence on the theoretical AVA curve. Despite its roughness, the AVA curve picked on the migrated CIGs obtained with the complete data agrees with the theoretical AVA trend. The AVA curve picked on the migrated CIG from the reconstructed wavefield (red) is much closer to the original one (black) when compared to the one picked on the migrated CIG (blue).

In the second example discussed in the section 3.3.3, a new survey is simulated where 80% traces are removed from the original Marmousi shot records. The incomplete wavefield is then used as the input for the MWNI algorithm to reconstruct the complete wave-

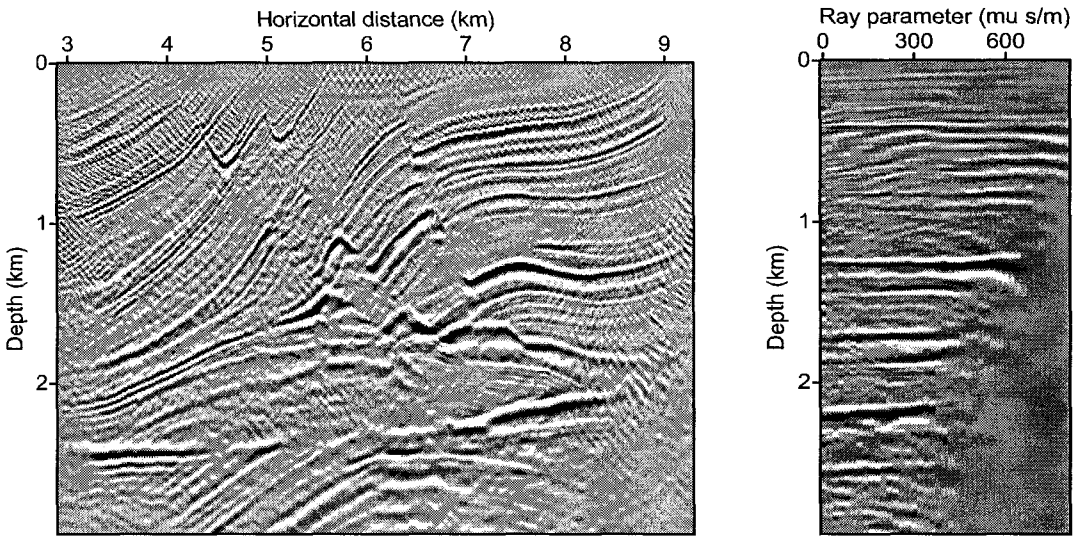

Figure 4.9: Migration of the Marmousi model and CIG at CMP location 7500 m using the decimated data.

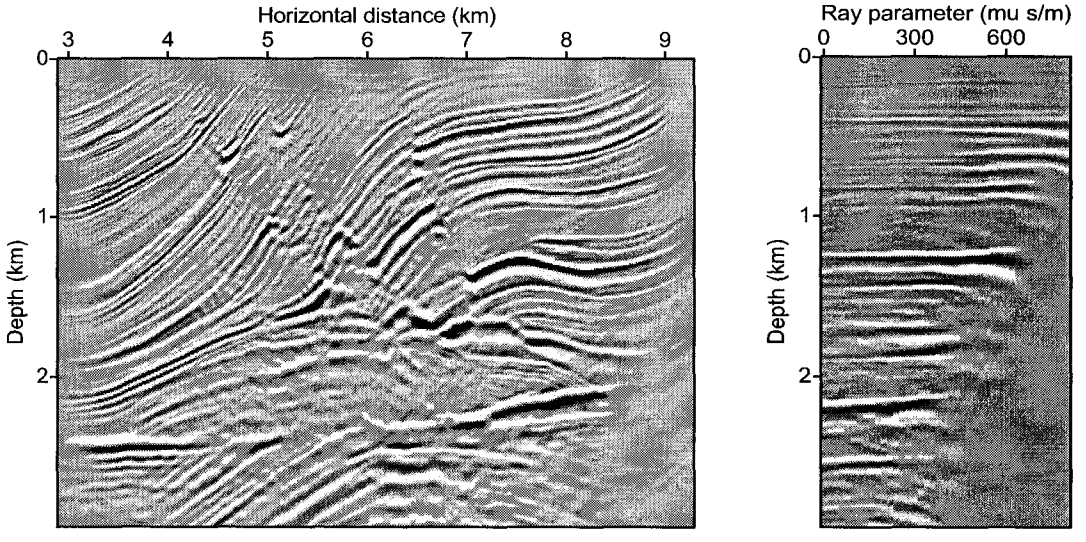

Figure 4.10: Migration of the Marmousi model and CIG at CMP location 7500 m using the reconstructed data.

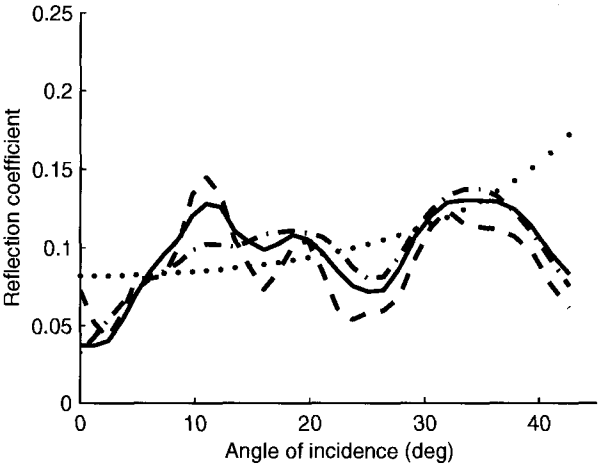

Figure 4.11: Theoretical (Green) and extracted AVA curves from the migrated angle gather (Black: original complete data, Blue: decimated data, Red: after interpolation).

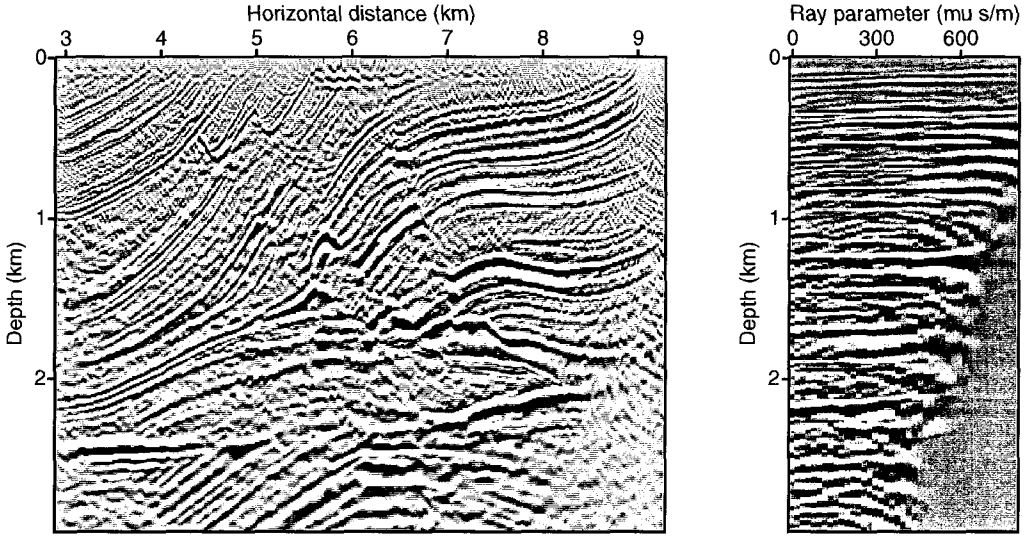

Figure 4.12: Migration of the Marmousi model and CIG at CMP location 7500 m using incomplete data where 80% original traces are removed .

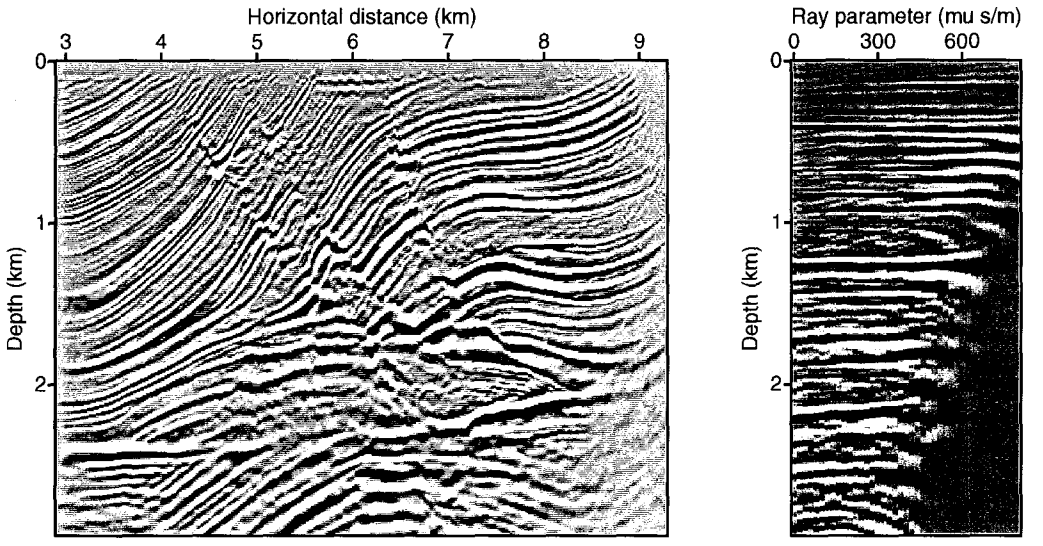

Figure 4.13: Migration of the Marmousi model and CIG at CMP location 7500 m using the reconstructed data.

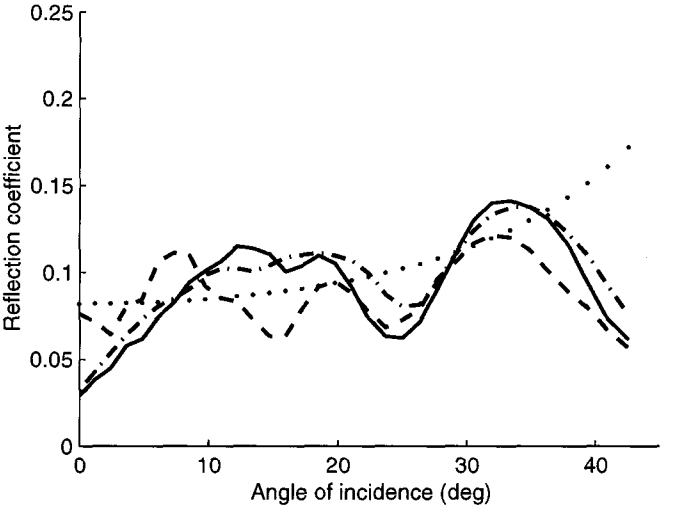

Figure 4.14: Theoretical (Green) and extracted AVA curves from the migrated angle gather (Black: original complete data, Blue: incomplete data, Red: after interpolation).

field and the complete (original), incomplete and reconstructed data sets are further tested with the split-step DSR AVA migration algorithm (Prucha et al., 1999). Figures 4.12-4.13 show both the stacked image and the migrated CIG at CMP location 7500 m using incomplete and reconstructed data sets. The incomplete sampling of the seismic wavefield results in acquisition footprint noises in both the stacked image and the CIG (Figure 4.12). In Figure 4.13, we observe that the migration with the reconstructed wavefield yields an overall cleaner stacked image and migrated CIG. The continuity of events in the CIG is also improved.

In Figure 4.14, the AVA curve picked on the migrated CIG from the reconstructed wavefield (red) is closer to the original one (black) when compared to the one picked on the migrated CIG (blue) of incomplete wavefield.

4.2.3 3-D Common Azimuth Synthetic data set

The 3-D MWNI algorithm is tested on a 3-D common azimuth synthetic data set. The data set is modeled with a constant (compressional) velocity model ($V_1 = 2500\,\mathrm{m/s}$). The density model consists of a single interface where the density above and below the interface are 1.7 $\mathrm{g/cm^3}$ to 2.0 $\mathrm{g/cm^3}$, respectively. Details including the layer thicknesses are specified in Table 4.2. A ray tracing technique is used to generate the synthetic data set. The geometrical spreading has been calculated by assuming a spherical wavefront resulting in a $1/r$ amplitude scaling, where r is the distance traveled by the ray. The synthetic data include total 40 xline CMPs and 301 inline CMPs. The xline and inline CMP intervals are 10 m and 5 m, respectively. The CMPs have a nonuniform number of offsets range from 0 to 1000 m. In Figure 4.16a, we show a CMP at inline 750 m xline 30 m position. The amplitude variation is due to the geometrical spreading effect only. We have randomly removed 90% of the traces in the synthetic data set (The incomplete

Velocity (m/s)	Density ($\mathrm{g/cm^3}$)	Thickness (m)
2500	1.7	100
2500	2.0	Half-space

Table 4.2: Parameters for the horizontally layered model with single reflecting interfaces. The reflector exhibits a constant AVA characteristic.

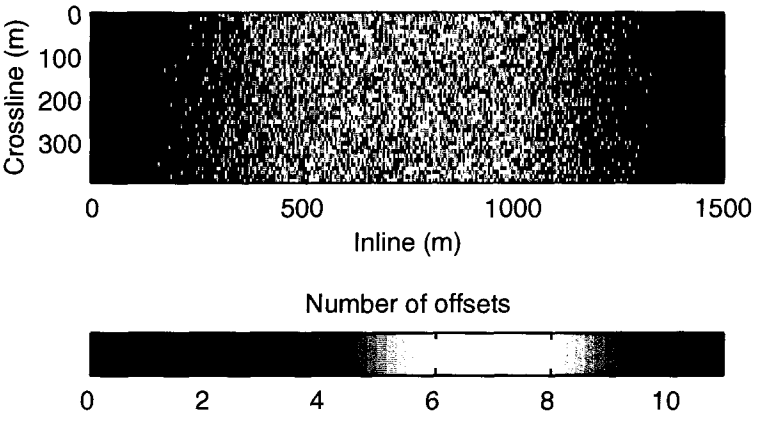

Figure 4.15: Distribution of offsets for the 3-D synthetic data used to test our interpolation algorithm.

CMP at the same position is shown in Figure 4.16b). The offset distribution in each CMP bin of incomplete data is illustrated in Figure 4.15. The incomplete data are used as the input for the reconstruction. We first perform the Fourier transform along the time axis. The reconstruction is then carried at temporal frequencies along three spatial (xline CMP, inline CMP and offset) coordinates simultaneously. The output offset ranges 0 m to 1000 m incrementing by 10 m for each CMP. Figure 4.16c shows the reconstructed CMP at the same position using MWNI.

Next, we migrate the complete, incomplete and reconstructed data sets with a 3-D common azimuth wave equation DSR AVA migration algorithm. The stacked image for xline CMP 30 m (inline CMP ranges from 750 m to 1000 m) obtained with the original data, incomplete data and reconstructed data are shown in Figure 4.17a-4.17c, respectively. Note both Figure 4.17a and 4.17c show uniform reflection strength at the reflector. In Figure 4.18a-4.18c, we show CIGs at inline CMP 750 m xline CMP 30 m position obtained with the original data, incomplete data and the reconstructed data, respectively. Clearly, the migrated CIG of incomplete data (in Figure 4.18b) is bore with acquisition footprint noise. The amplitude is not continuous along the ray parameter axis. On the other hand, the migrated CIG of reconstructed data is significant cleaner and exhibits the smooth AVP. We have extracted AVA curves for the reflector from the above CIGs (Figure 4.19). Note that the AVA curve obtained from the incomplete data (in Figure 4.19b)

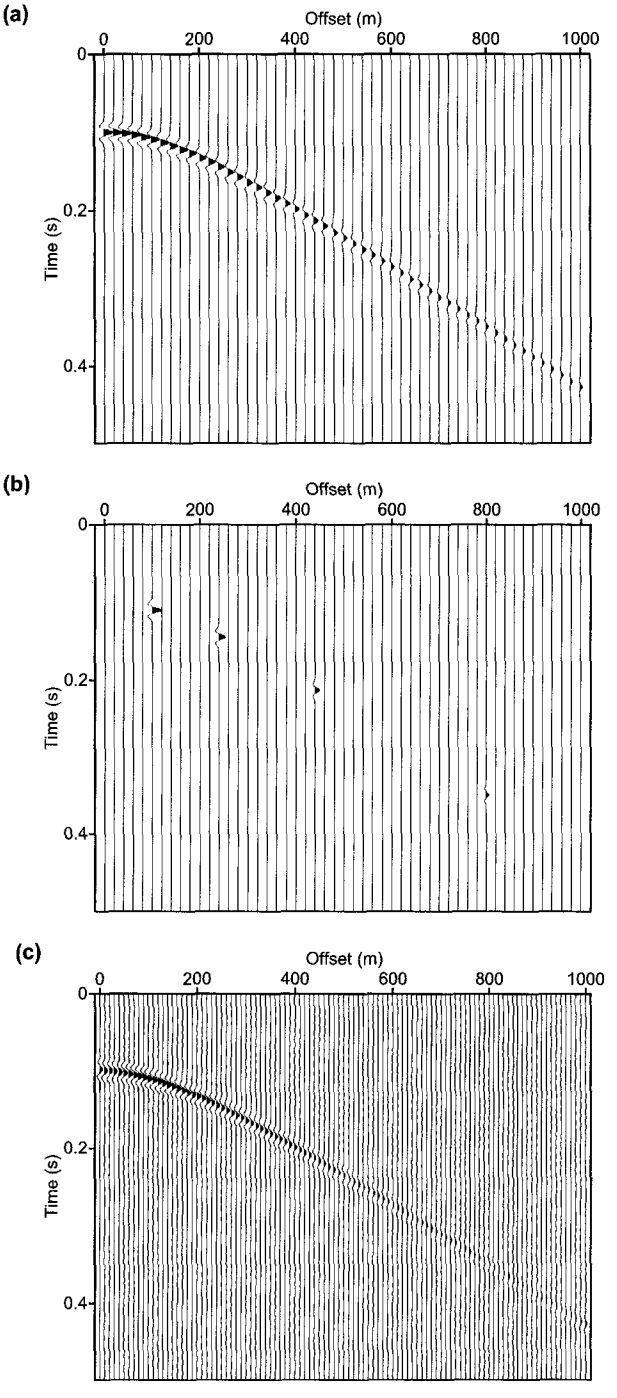

Figure 4.16: The CMP at inline 750 m and xline 30 m position of original data (a), incomplete data (b) and reconstructed data (c).

does not agree with the theoretical AVA trend at all and the AVA curve obtained from reconstructed data (in Figure 4.19c) matches the one obtained from original data (in Figure 4.19a) and agrees with the theoretical AVA trend for a large range of incidence angles.

4.3 Summary

Wave equation AVA imaging can be seen as a preprocessing step for AVA inversion. Wave equation downward continuation makes use of the Fourier transform and thus requires well sampled data as inputs. When seismic data are regularly and densely sampled, the wave equation AVA imaging algorithm yields reliable AVA estimation. On the other hand, an inadequate sampling interval and missing traces (gaps) will result in an incorrect surface wavefield. Examples in this chapter show that the incorrect wavefield introduces noises and aliasing events in both the migrated image and angle domain CIGs. Consequently, the fidelity of AVA analysis on those CIGs is compromised.

MWNI scheme has been successfully applied to 2-D and 3-D synthetic data set for prestack interpolation. MWNI preconditions the surface wavefield for the wavefield AVA imaging. Examples show that with MWNI of prestack wavefield, acquisition artifacts are minimized in both the migrated image and angle domain CIGs, and migrated amplitudes are reliable for further AVA analysis.

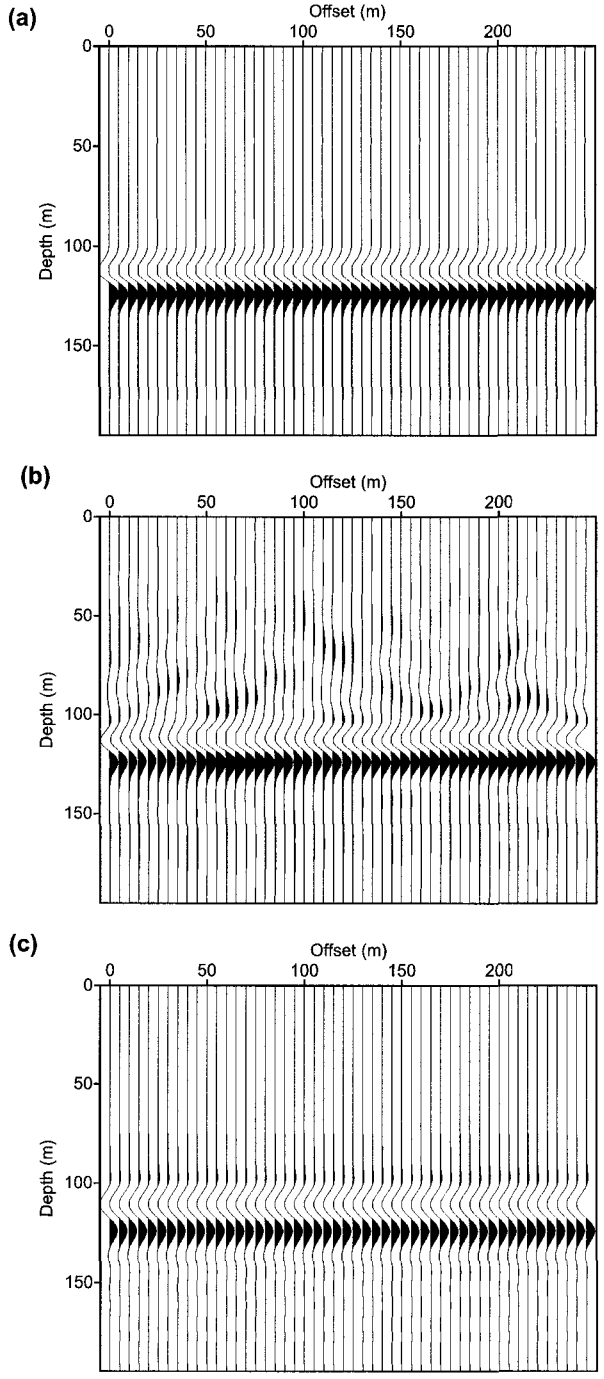

Figure 4.17: The stacked image for xline 30 m obtained with original data (a), incomplete data (b) and reconstructed data (c).

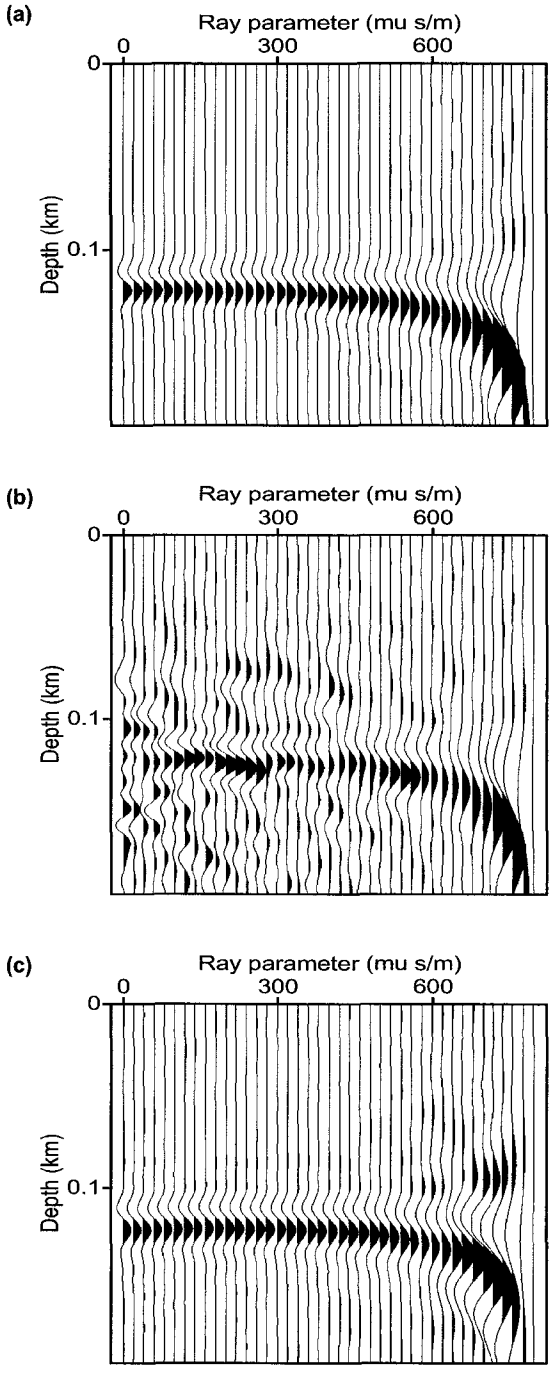

Figure 4.18: The migrated CIG at xline 30 m inline 750 m position obtained with original data (a), incomplete data (b) and reconstructed data (c).

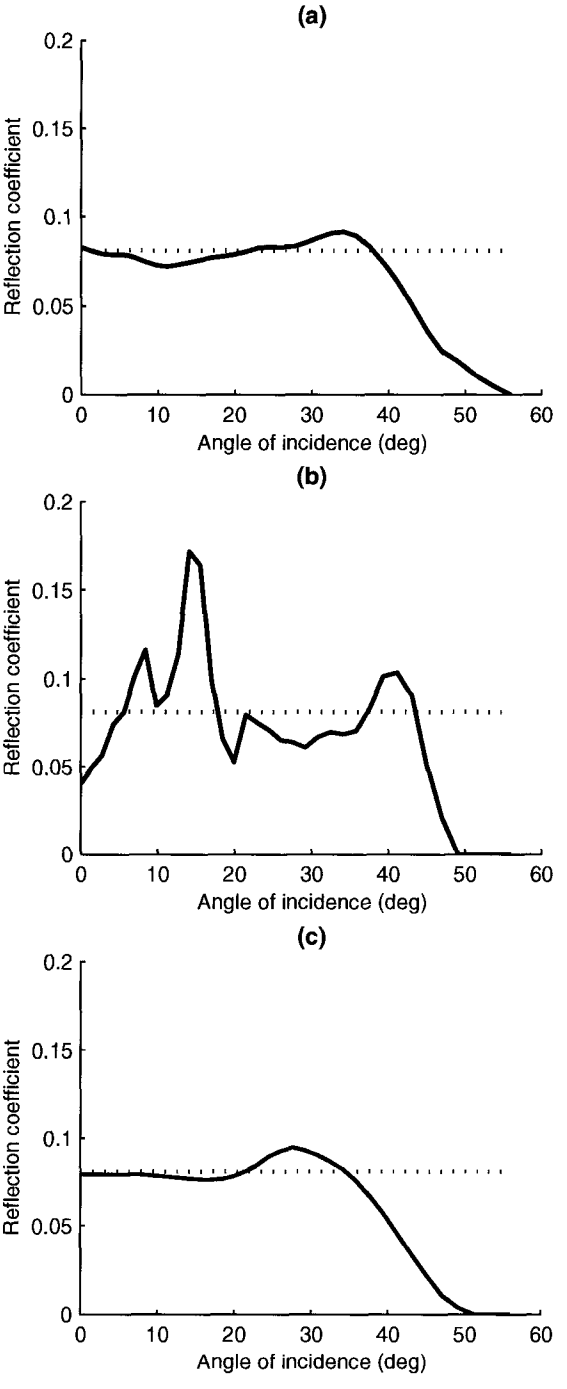

Figure 4.19: The AVA curves extracted from the migrated CIG at xline 30 m inline 750 m position obtained with original data (a), incomplete data (b) and reconstructed data (c).

Chapter 5

Field data example

In Chapters 2 and 3 a reconstruction scheme for band limited seismic data that enables us to precondition seismic data for imaging and, in particular, for the estimation of common image gathers for AVO/AVA analysis was proposed. We have also demonstrated with synthetic examples that MWNI does not alter the amplitude character of the reflections. The latter is an extremely important point to take into consideration when preprocessing with AVO/AVA applications in mind.

In this Chapter we apply MWNI to two field data experiments. In the first case we analysis a 3-D survey from the Erskine area (Alberta, Canada). This is a typical orthogonal 3-D survey from the Western Canadian Sedimentary Basin (WCSB). It depicts quite well the type of problems encountered when imaging seismic data for AVO/AVA analysis in the WCSB.

The second example is a data set from an undisclosed area. This test was carried to analyse the feasibility of using MWNI to reconstruct the full prestack data volume prior to processing as a means to decrease sampling artifacts in the subsequent processing flow.

The 3-D and 4-D interpolation are carried out along the vector of spatial coordinates $\mathbf{u}$ for each temporal frequency ω. In other words, we denote the seismic data at one monochromatic temporal frequency component as $D(\mathbf{u}, \omega)$, where, for instance $\mathbf{u} = [x_m, y_m, x_h]$ defines a constant azimuth 3-D data volume in terms of the two midpoint positions x_m, y_m and the inline offset x_h, similarly, $\mathbf{u} = [x_s, y_s, x_r, y_r]$ denotes a 4-D data volume defined in terms of source and receiver positions. Bear in mind that N-D refers to the number of spatial dimensions of the reconstruction problem. Therefore

we have

$N = 3$ Interpolation of 3-D prestack common azimuth volumes
$N = 4$ Full spatial interpolation (multi-azimuth interpolation)

5.1 3-D spatial interpolation: Erskine data set

In this section, the MWNI algorithm is used to interpolate a 3-D prestack common azimuth data set acquired in the Erskine (Southern Alberta, Canada). The target of the survey is gas sand in the Leduc formation. Some of acquisition parameters of the Erskine 3-D data are:

- time sampling interval: 2 ms;
- number of samples per trace: 1000;
- inline CDP interval: 33.5 m;
- crossline CDP interval: 50.29 m;
- nominal fold: 20;
- datum elevation: 840 m;
- N/S inlines: #1-157 E/W crosslines: #1-40;
- CDP bins: 33.5 $\times$ 50.29 m;
- Primary sort direction: N/S azimuth: 180.587860.

Note that All traces with azimuth other than 180 degree have been thrown away to form the Erskine 3-D common azimuth data set.

In addition, the following processing steps have been applied to the data set prior to interpolation:

- spherical divergence;
- deconvolution;
- surface consistent statics;

- bandpass filtering (10/15 Hz- 65/80 Hz).

The field data set is acquired with a orthogonal geometry where source and receiver lines are laid out orthogonal to each other. Because the receives cover a large area, this method is sometimes referred to as the patch method (Cordsen et al., 2000). In an orthogonal design, active receiver lines form a rectangular patch surrounding each source point location; creating a series of cross-spreads that overlap each other. The patch often has a longer axis in the inline direction. The distinction between narrow and wide azimuth surveys is made on the basis of the aspect ratio of the recording patch. The aspect ratio is defined as the cross-line dimension of the patch divided by the inline dimension. Recording patches with an aspect ratio less than 0.5 are considered narrow azimuth, while recording patches with an aspect ratio greater than 0.5 are wide azimuth. Large-aspect-ratio (i.e. 0.6 to 1.0) patch leads to a good azimuth distribution which increases the ability to detect azimuth-dependent variations that arise from the dip and/or anisotropy.

The original Erskine data set contains 157 inlines and 40 crosslines with offsets aligned along the inline direction. The offset distribution in each CMP bin is illustrated in Figure 5.1. Figure 5.2a shows the original sparse offset sampling geometry in the crossline-midpoint offset domain for inline #6 (only parts of the crossline midpoints are shown) and Figure 5.2b shows the offset sampling geometry after interpolation. Prestack interpolation is simultaneously applied along three dimensions, namely: inline-midpoint, crossline-midpoint and offset. Figure 5.3a shows original CMPs for inline #6 and crosslines #15-18. The reconstructed result is shown in Figure 5.3b. Notice that the MWNI reconstruction has managed to reconstruct the missing traces. Traditional resampling methods like f-x interpolation (Spitz, 1991) cannot handle these type of situations. They are only valid approaches for resampling from a regular geometry to another regular geometry; consequently, irregularly sampled data and large gaps cannot be interpolated. It is also important to mention that most interpolation methods operate quite well on small windows of individual seismic gathers. This is because they are often built upon the assumption of predicability of linear events (Spitz, 1991; Soubaras, 1995; Sacchi and Kuehl, 2001; Gulunay, 2003). The linear event model is only valid within small data windows. This is why for realistic data reconstructions it is necessary to go beyond the linear event model.

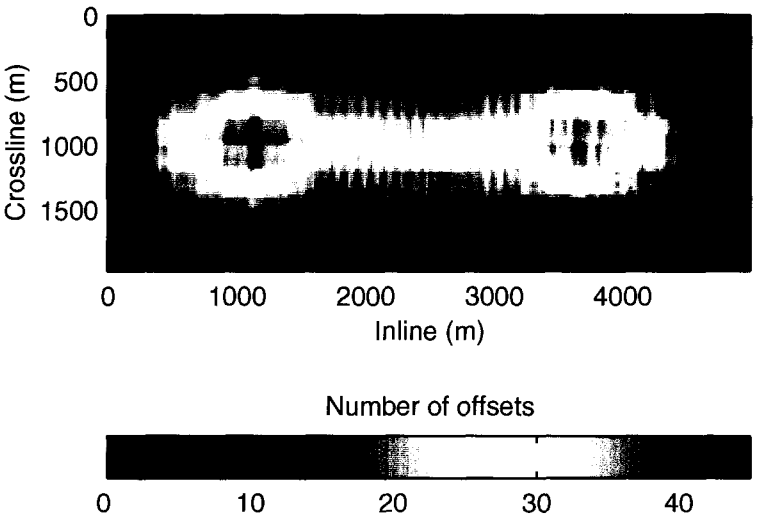

Figure 5.1: Distribution of offsets for the Erskine 3-D data set used to test our interpolation algorithm.

The MWNI does not make any assumption about the linearity of events in the data and therefore, breaking down the data into small windows is not necessary.

To continue with our experiment, 3-D common azimuth wave equation DSR AVA migration is applied to both original and interpolated data sets. Figure 5.4a-5.4b show migrated images for crossline #36 and inline #71; in both cases data before interpolation were used in the migration. Note that the irregular and sparse data sampling results in images of poor quality. Migrated images obtained with interpolated data are portrayed in Figures 5.4c-5.4d. The impact of interpolation before AVA imaging can also be seen in the ray parameter CIG domain. CIG gathers for crossline #36 and inline #71 are shown in Figures 5.5a and 5.5b, respectively. Migration with interpolated data as input yields a CIG gather (Figure 5.5b) with reduced artifacts and better event continuity.

5.2 4-D MWNI, application to 3-D multi-azimuth data set (WCSB)

In this section, a 4-D MWNI scheme is used to interpolate a multi-azimuth 3-D land data set from the WCSB provided by the Encana Corporation.

The data set was acquired using the mega-bin acquisition scheme. The mega-bin

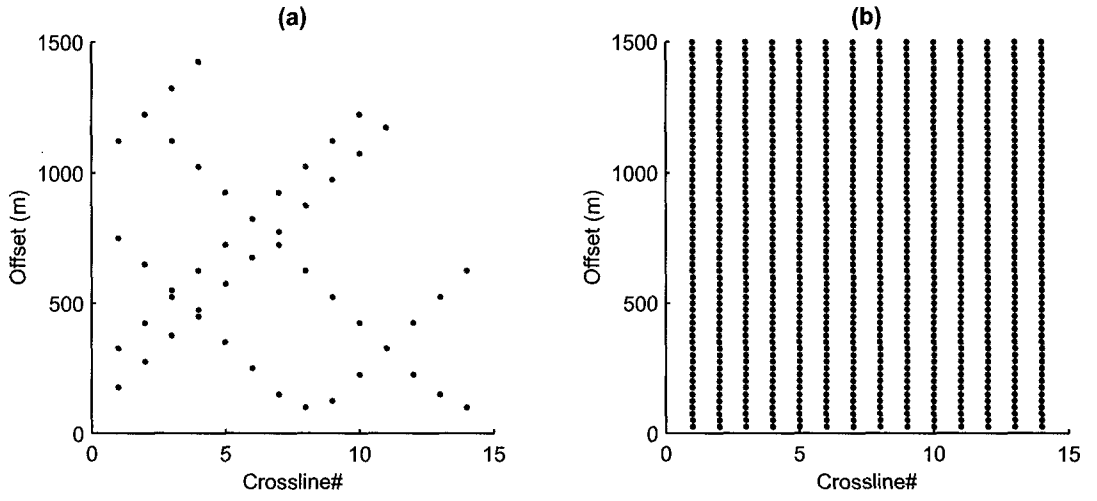

Figure 5.2: (a) The map of the incomplete geometry for inline #6 (Note only parts of the crossline midpoints are shown). (b) The complete geometry after interpolation for inline #6.

method was developed by Goodway and Ragan (1995) from Encana. The technology is designed to improve upon traditional 3-D seismic resolution by providing a clearer, high-resolution image of geological formations. The higher resolution produced by mega-bin is due to spatial sampling and acquisition design enhancements. This technique, coupled with wave-field interpolation (i.e. premigration f-x interpolation), results in superior statistics for processing that gives a higher quality 3-D seismic image.

Figure 5.6 shows a window of shot distribution of the survey used to acquire the 3-D data set. Shot and receiver geometries of the survey are also illustrated in Figure 5.7a and 5.7c, respectively. The original shot spacing along the inline and crossline direction is 140 m. The receiver spacing is 70 m along the inline direction and 140 m along the crossline direction. Note that many shots and receivers are missing in the real geometry. Shot and receiver geometries of the interpolated output are shown in Figure 5.7b and 5.7d, respectively. Note that after interpolation, the shot spacing along the inline direction is reduced to 70 m and the shot spacing along the crossline direction remains the same. Both inline and crossline receiver spacings are reduced to 35 m after interpolation. Also note that original geometries produce a bin size of (70 m $\times$ 70 m) while new geometries produce a smaller bin size of (17.5 m$\times$17.5 m).

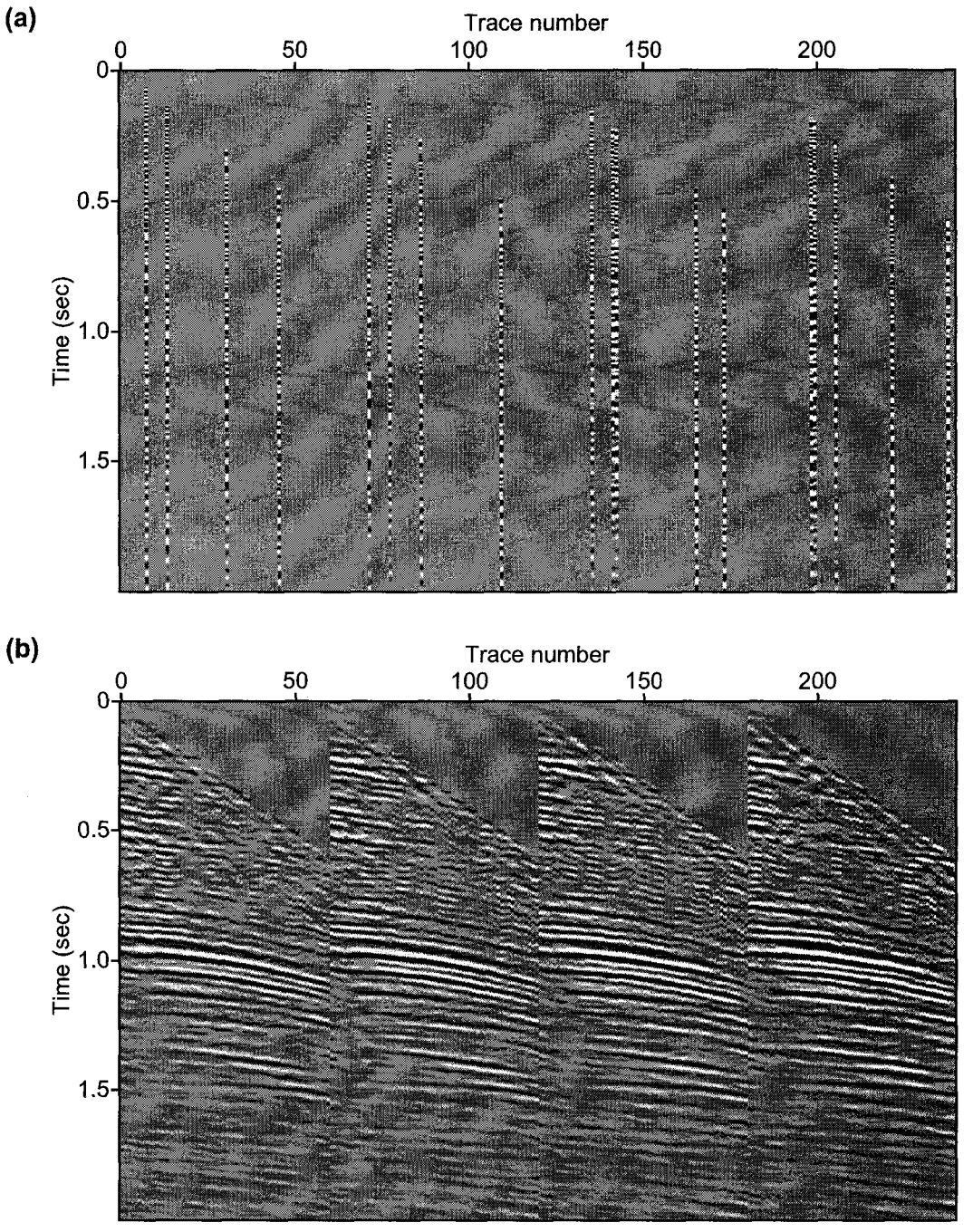

Figure 5.3: (a) Original traces in four adjacent CMPs corresponding to inline #6 and crosslines #15 – 18. (b) Reconstructed CMPs.

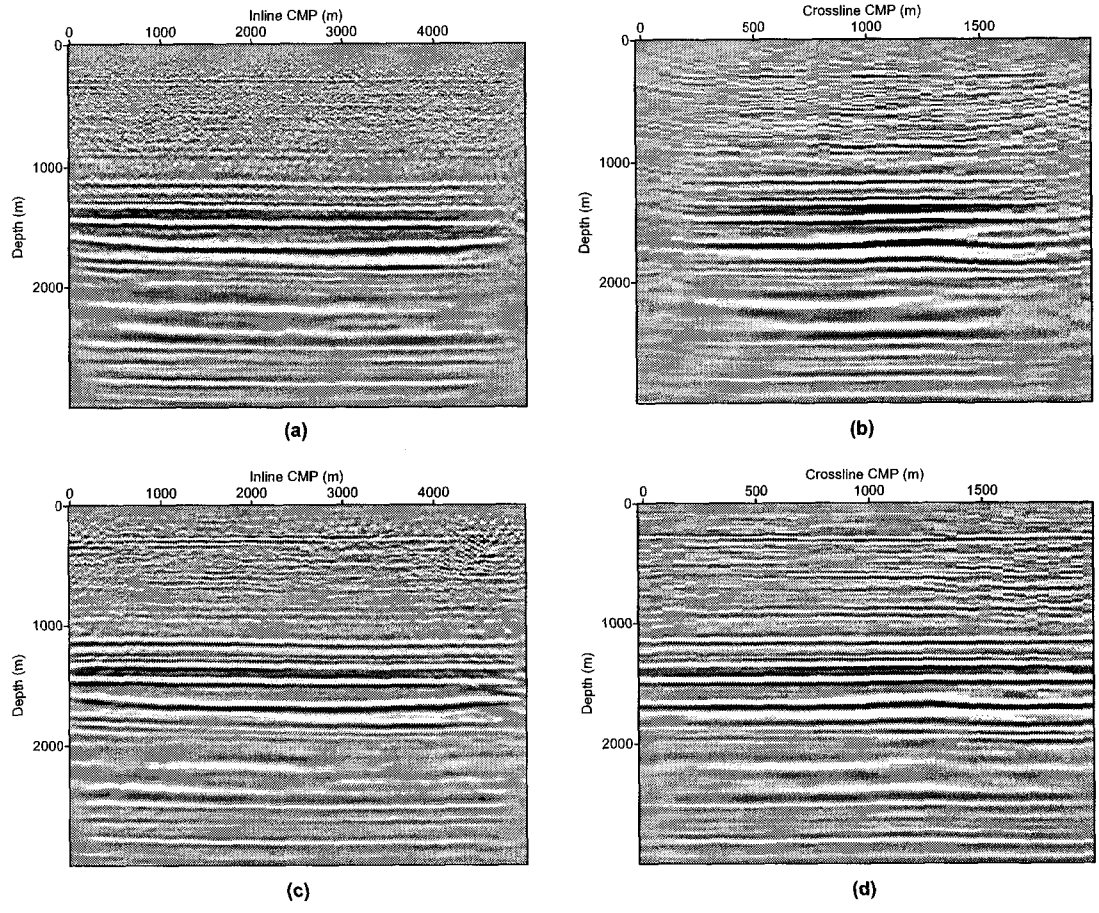

Figure 5.4: (a) The migrated image for crossline #36 without interpolation. (b) The migrated image for inline #71 without interpolation. (c) The migrated image for crossline #36 with interpolation. (b) The migrated image for inline #71 with interpolation.

Before interpolation, the data have been datumed to the same depth. Both data with and without NMO correction are used as the input for interpolation. The interpolation began by dividing the whole survey area into many sections, the 4-D MWNI is applied along x_s, y_s, x_r, y_r coordinates in each section. Figure 5.8 shows the output shot geometry in one section. There are approximately 8 $\times$ 8 shots in each section.

Figure 5.9 shows a comparison of inline receivers before (Figure 5.9a) and after (Figure 5.9b) interpolation without NMO correction. The inline receiver sampling rate is doubled after interpolation. Part of the data (in the window) are zoomed and shown in Figure 5.10. Crossline receivers before and after interpolation are shown in Figure

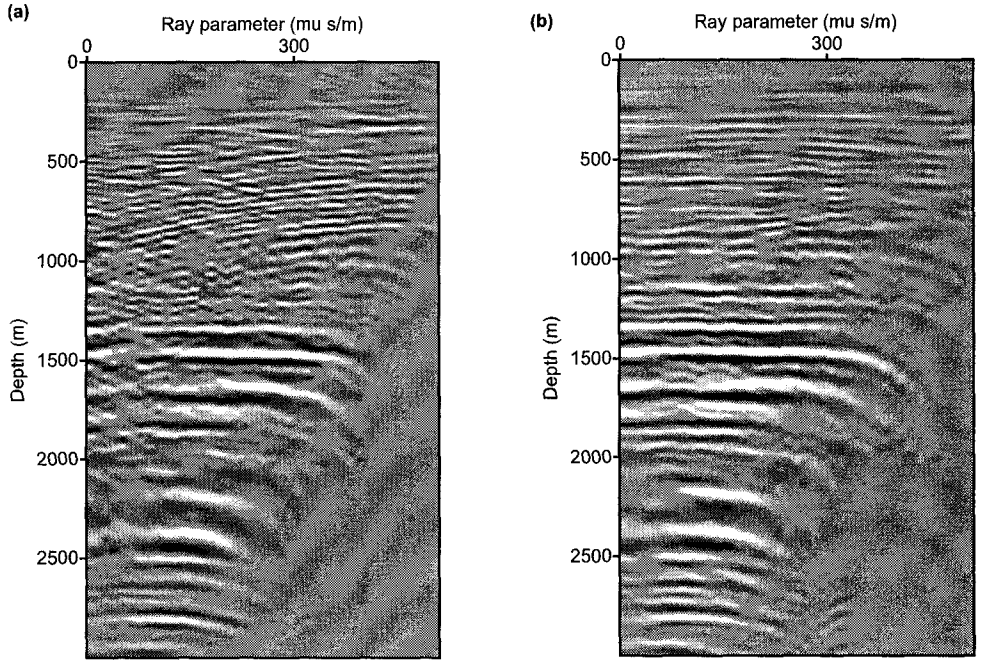

Figure 5.5: Ray parameter domain CIGs obtained with the undersampled data (original prestack volume) (a) and the reconstructed data (b).

5.11a and Figure 5.11b, respectively. Note that after interpolation, the receiver sampling along crossline is reduced to 35 m from 140 m. The data in the window of Figure 5.11 are zoomed and shown in Figure 5.12.

Figure 5.13a and 5.13b show a comparison of inline receivers before (Figure 5.13a) and after (Figure 5.13b) interpolation where NMO correction has been applied before interpolation to reduced the wavenumber bandwidth. Crossline receivers before and after interpolation with NMO correction are shown in Figure 5.13c and 5.13d, respectively.

A comparison of a 3-D cube of final stacks with and without interpolation is shown in Figure 5.14. Finally, the data are migrated using prestack Kirchhoff time migration. The crossline migrated images without and with interpolation are shown in Figure 5.15a and 5.15b, respectively. Part of the images are zoomed and shown in Figure 5.16. Note the improved spatial resolution in the migrated image with interpolation.

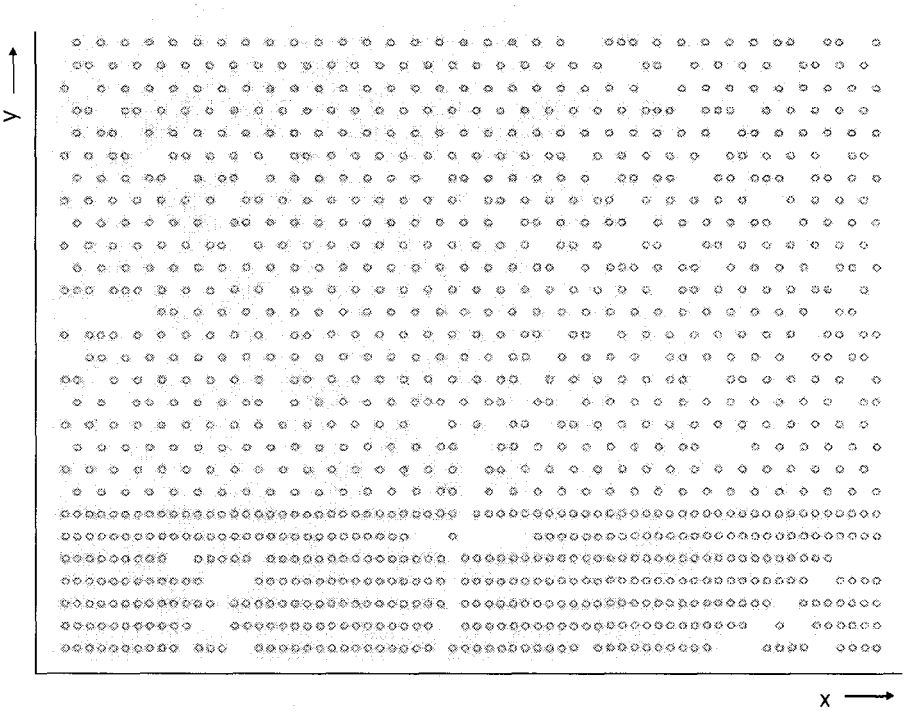

Figure 5.6: Window showing the distribution of shots for the data used to test 4-D MWNI algorithm

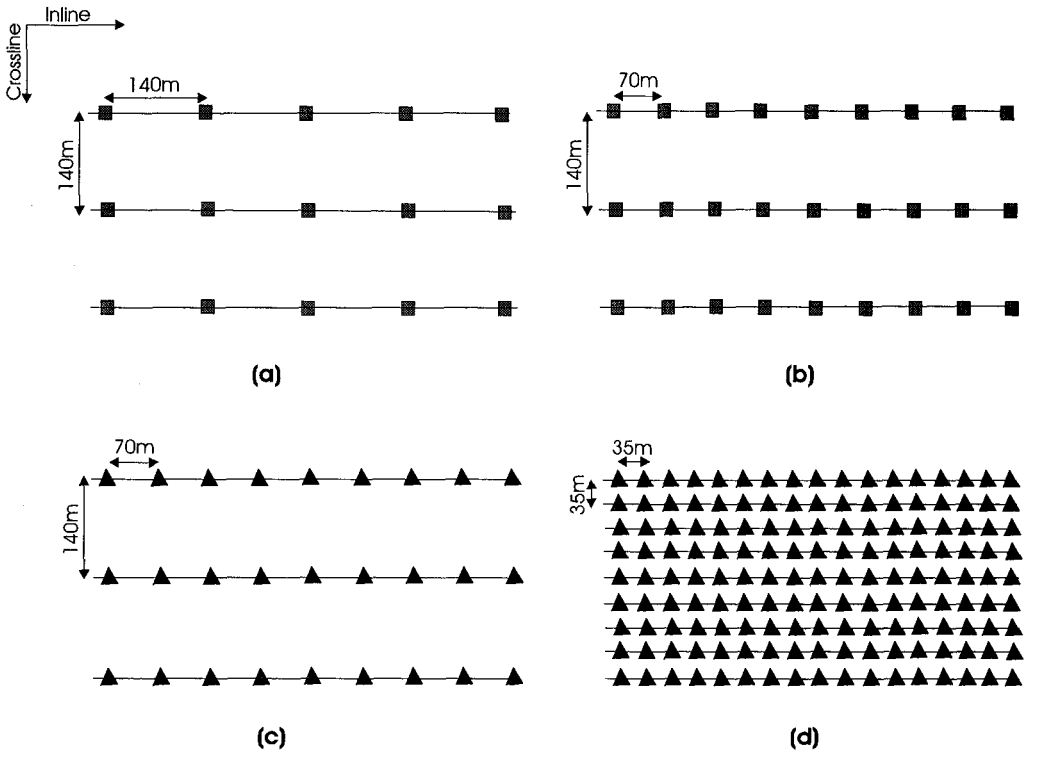

Figure 5.7: The input and output geometry of the 4-D interpolation. (a) The original shot geometry. (b) The output shot geometry. (c) The original input receiver geometry. (d) The output receiver geometry.

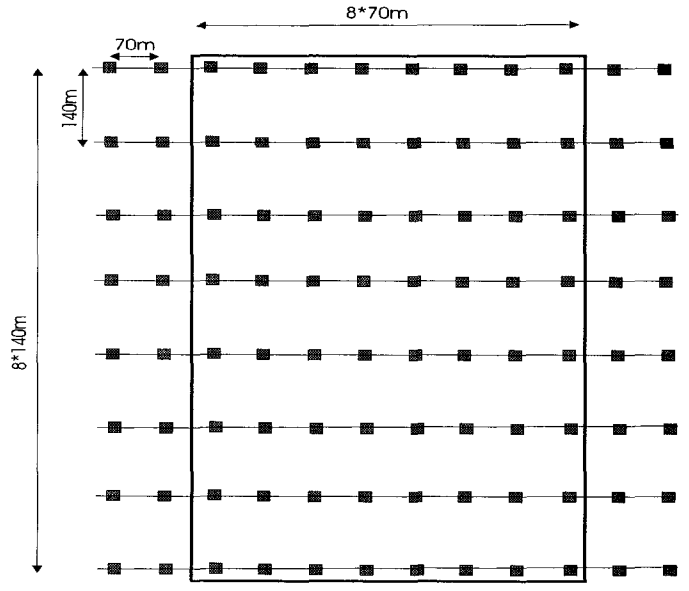

Figure 5.8: The output shot geometry in one section of interpolation. There are approximately 8×8 shots in each section.

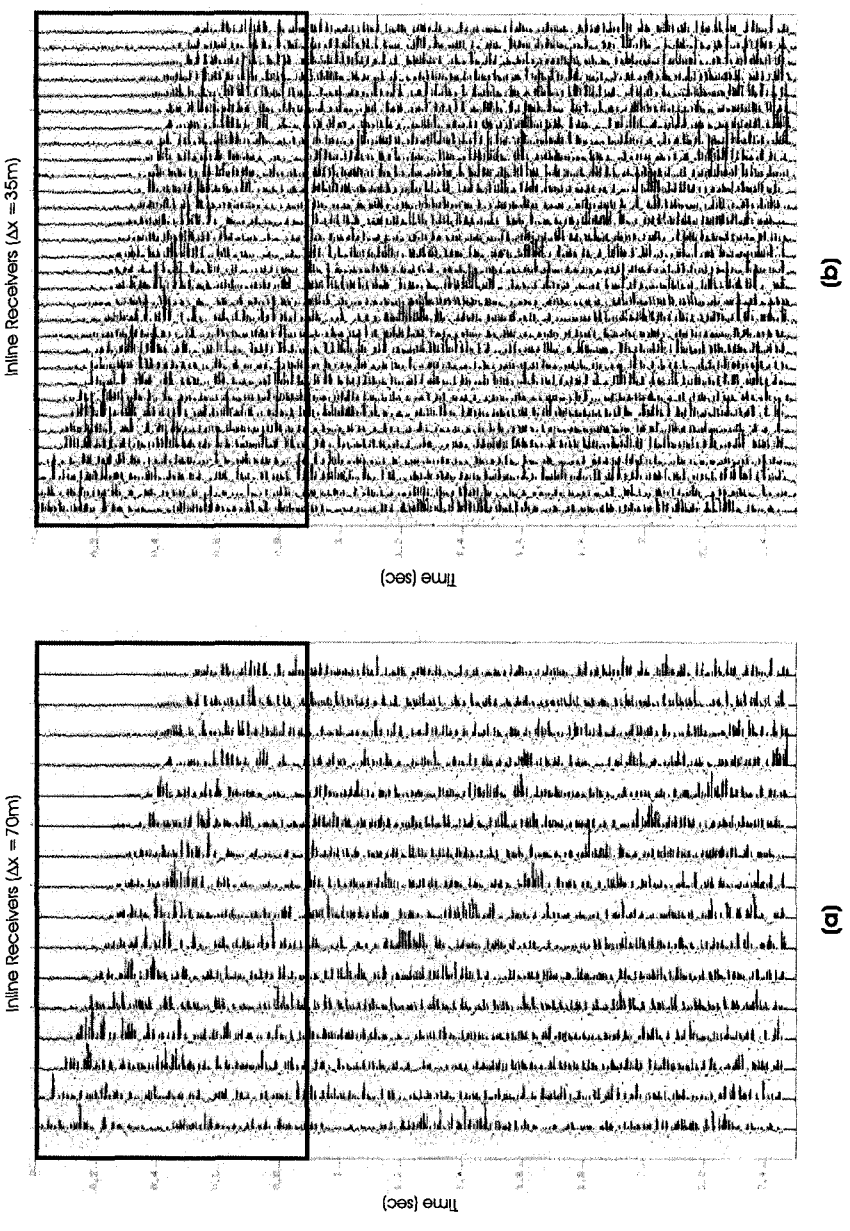

Figure 5.9: Inline receiver interpolation. (a) The original receiver line with a sampling interval of 140 m. (b) The interpolated receiver line with a sampling interval of 35 m.

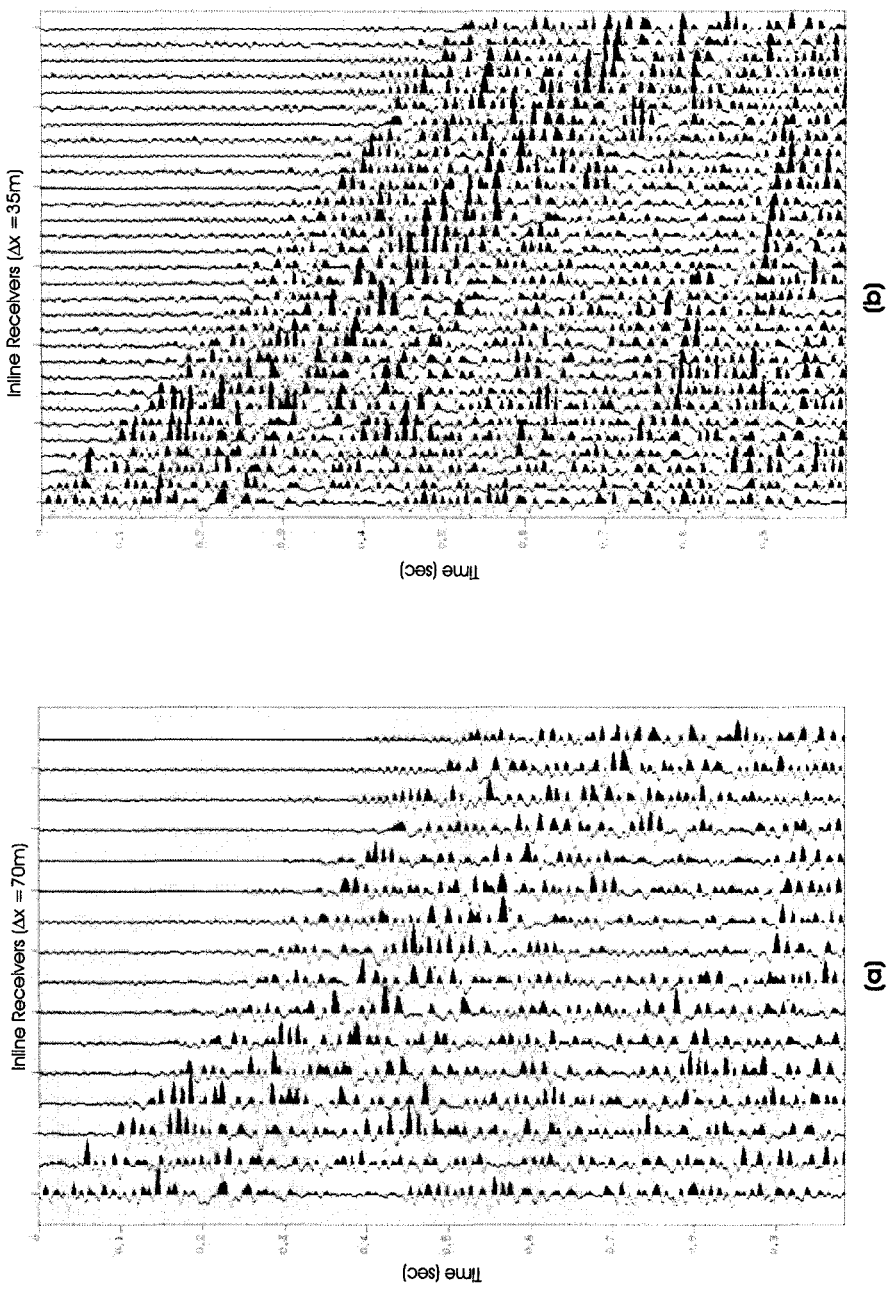

Figure 5.10: Inline receiver interpolation (zoomed). (a) The original receiver line with a sampling interval of 70 m. (b) The interpolated receiver line with a sampling interval of 35 m.

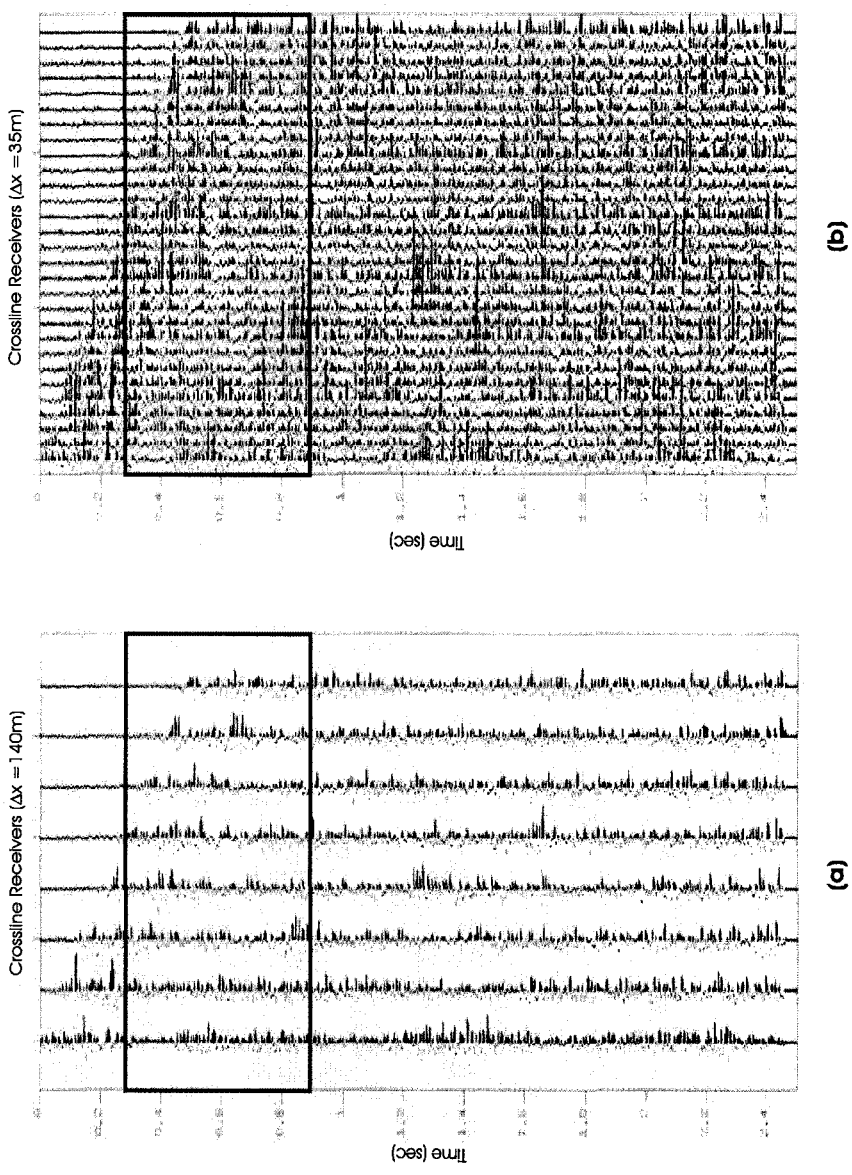

Figure 5.11: Crossline receiver interpolation. (a) The original receiver line with a sampling interval of 140 m. (b) The interpolated receiver line with a sampling interval of 35 m.

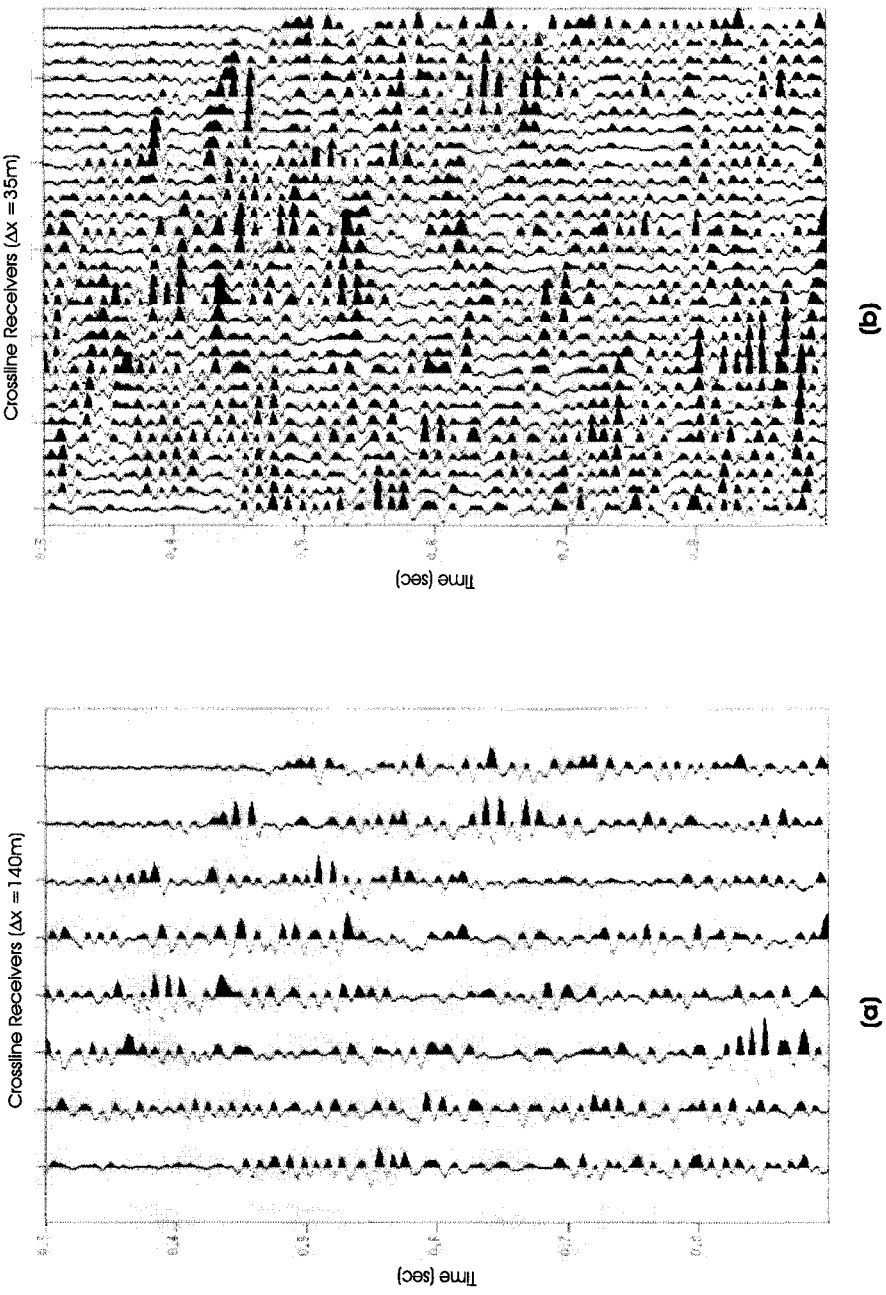

Figure 5.12: Crossline receiver interpolation (zoomed). (a) The original receiver line with a sampling interval of 140 m. (b) The interpolated receiver line with a sampling interval of 35 m.

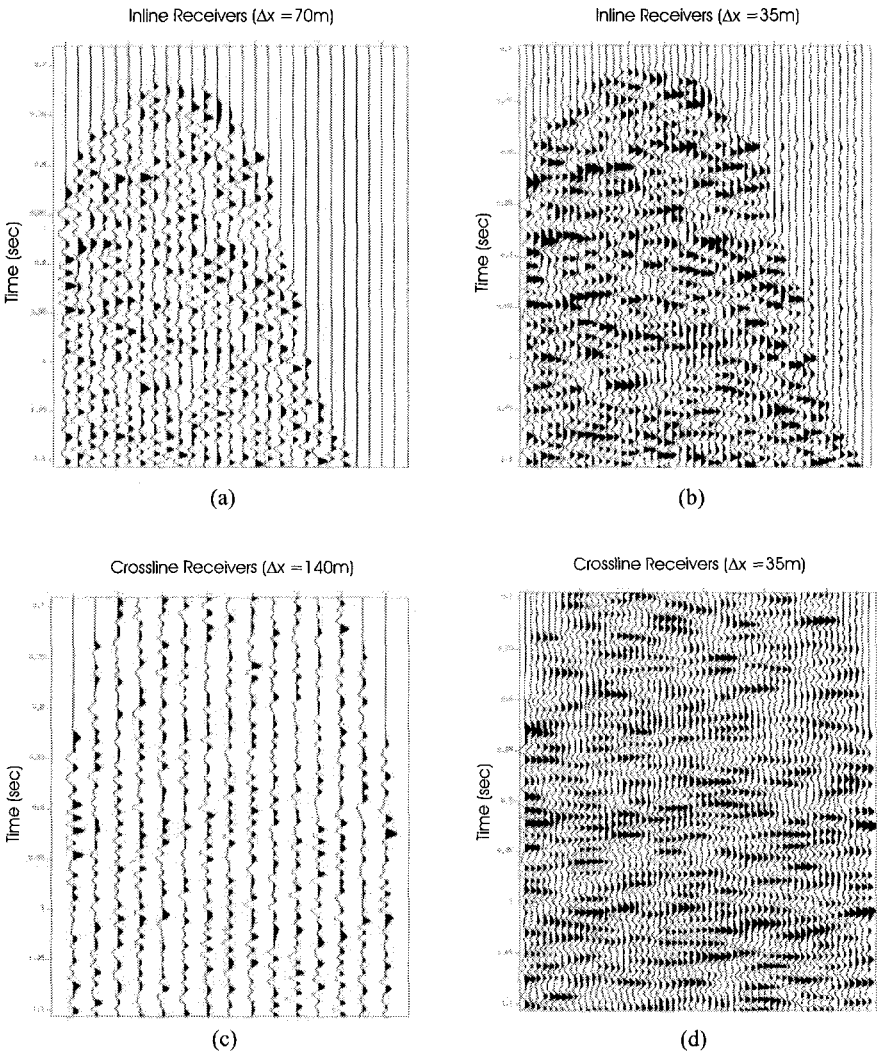

Figure 5.13: Interpolation of inline and crossline receivers with NMO (zoomed). (a) Original inline receivers with a sampling interval of 70 m. (b) Interpolated inline receivers with a sampling interval of 35 m. (c) Original crossline receivers with a sampling interval of 140 m. (d) Interpolated crossline receivers with a sampling interval of 35 m.

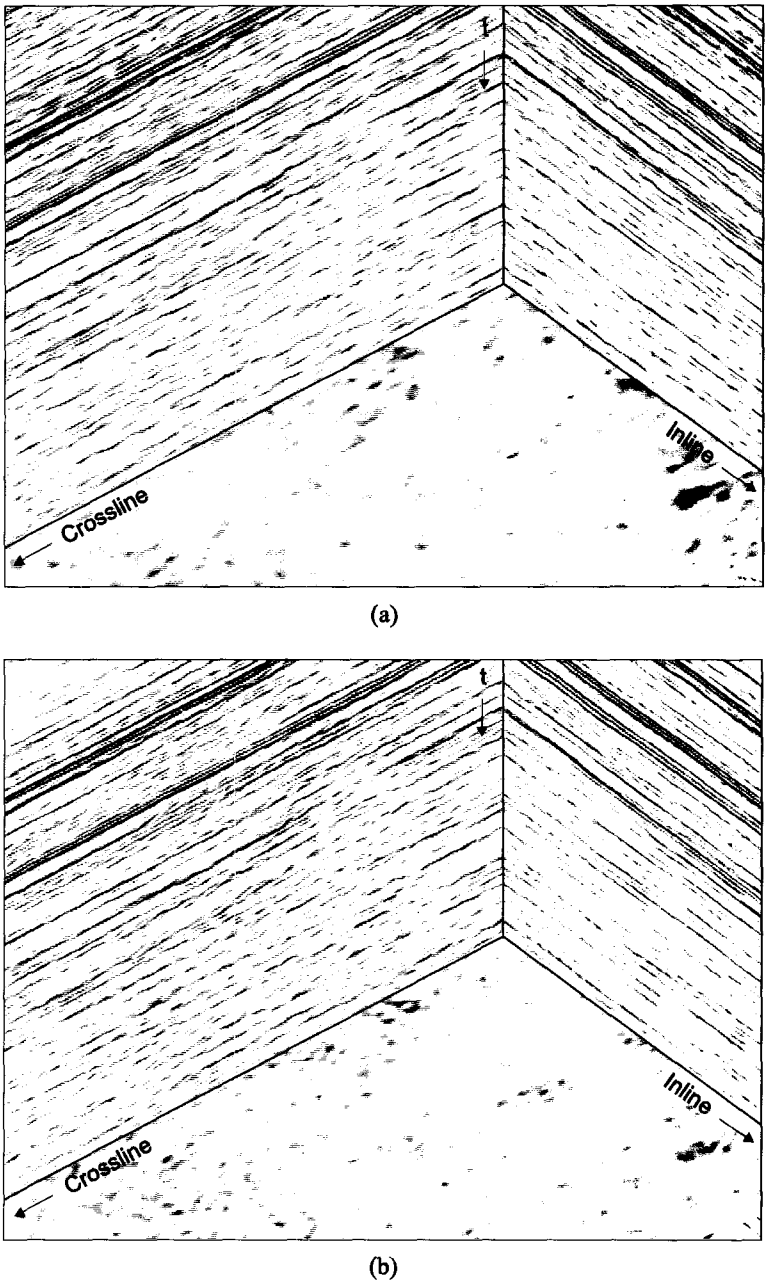

Figure 5.14: 3-D cubes of final stacks. (a) The original 3-D cube of the stack without interpolation. (b) The 3-D cube of the stack with interpolation.

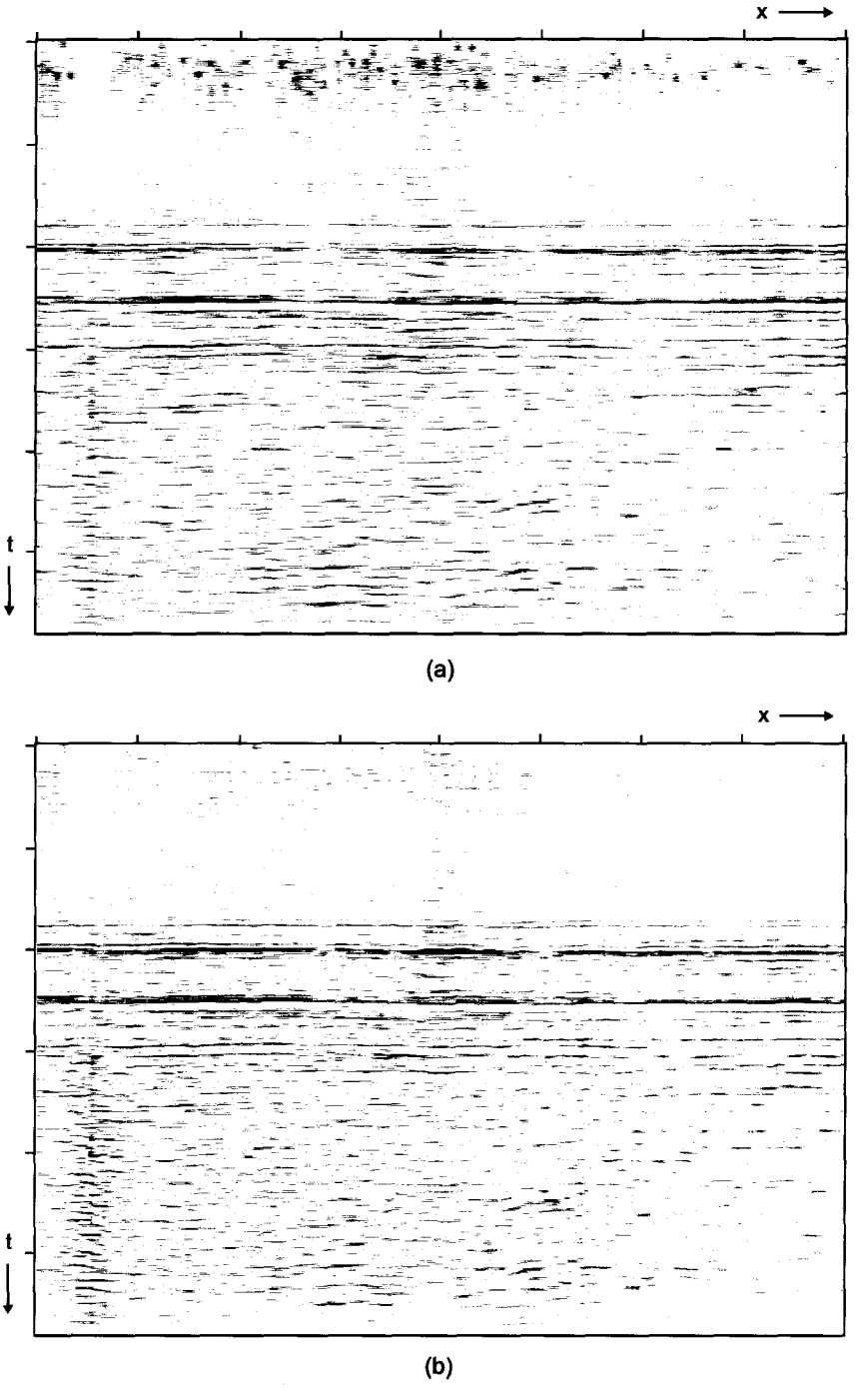

Figure 5.15: Migrated crossline using the original data (a) and the interpolated data (b).

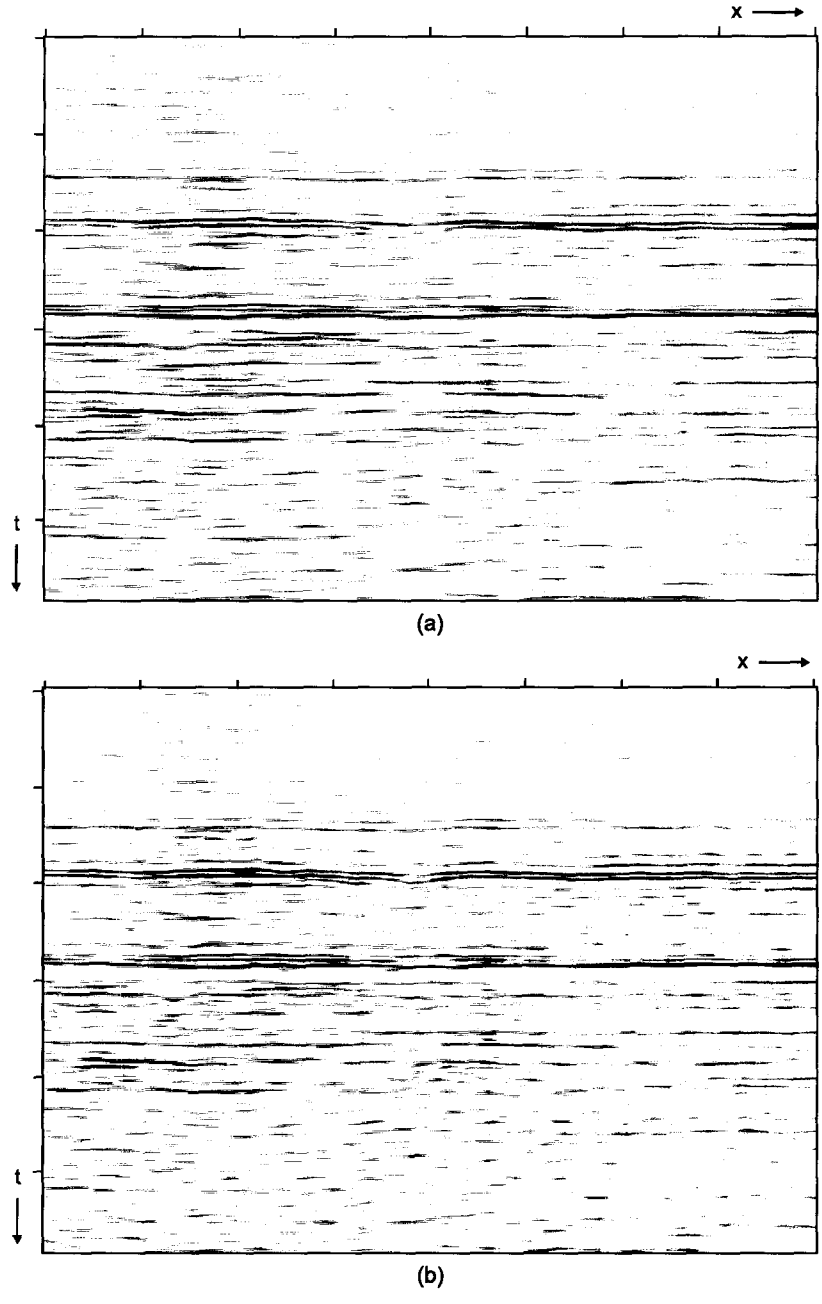

Figure 5.16: Migrated crossline (zoomed) using the original data (a) and the interpolated data (b).

Chapter 6

Discussion and Conclusions

Data recorded in a reflection seismic survey is a discrete version of a continuous wavefield. To uniquely characterize the continuous wavefield from the recorded data, the wavefield should be sampled at a rate higher than its Nyquist rate. However, recorded seismic data are always spatially incomplete to some degree. In this case, the problem of reconstruction can be dealt in the discrete space domain with inverse theory.

This thesis proposed a minimum weighted norm interpolation algorithm where band limited interpolation is formulated as a minimum norm least squares type problem where an adaptive DFT-weighted norm regularization term is used to constrain solutions. The method permits one to incorporate the a priori spectral signature (bandwidth and the signal spectrum shape) of the unknown wavefield.

Numerical examples with synthetic and field data are used to demonstrate the merits of the proposed interpolation scheme. It is found that the minimum weighted norm interpolation algorithm often yields a better solution than a regular minimum norm interpolation algorithm.

The MWNI is efficiently implemented with the preconditioned CG and the FFT. The computational efficiency makes it attractive to interpolate huge 3-D prestack datasets and to deal with higher dimensional interpolation problems where other interpolation methods become prohibitive. The innovative multi-dimensional schemes are proposed which allow the method to exploit the multi-dimensional nature of the seimsc data wavefield for and optimal seimic data reconstruction. The 3-D and 4-D MWNI schemes have been successfully applied to 3-D common-azimuth and multi-azimuth field data reconstruc-

tion problems.

The incompleteness of the recorded wavefield creates problems for multichannel processing steps such as suppression of coherent noise (multiple and ground roll), migration and inversion which often require regular and dense sampling. The proposed algorithm can be used to render seismic data into a form that makes is more suitable multichannel processing algorithms. In this thesis, we have particularly demonstrated the effectiveness of the 2-D/3-D MWNI scheme at the time of preconditioning seismic data for wave equation AVA imaging. Examples with synthetic and real 3-D data show an important reduction of sampling artifacts both in the stacked image and in individual AVA gathers by using MWNI before AVA imaging.

The proposed MWNI algorithm is different from the high resolution DFT approach using sparseness constraints. Also, present work does not attempt to invert the non-uniform DFT (Duijndam et al., 1999; Schonewille, 2000; Zwartjes and Duijndam, 2000), the MWNI implementation utilizes FFTs and therefore an important gain in efficiency is achieved when interpolating data that depend on more than one spatial dimension. For irregularly sample data, the data should be regularized first. For example, binning data with into small bins; assuming regularly spaced traces and ignoring variations in their true location. Note that binning data with a smaller bin size will increase the data volume to be interpolated. In this case, methods like the pruning FFT may be used to further cut the computation time.

Aliasing is always a challenge that needs to be faced when dealing with Fourier based interpolation methods. The anti-alias iterative strategy introduced in Chapter 3 can be only used to deal with mild aliasing. An anti-aliasing f-k domain Fourier reconstruction method was discussed by Gulunay (2003), where an anti-aliasing filter derived from the non-aliased low frequency part of the data is incorporated in the aliased high frequency reconstruction. Such strategy can also be used to derive weights for the MWNI algorithm and finally, enable us to interpolate aliased data. However, this strategy requires regularly spaced inputs and it is only valid on small windows where the assumption of linear events is valid. By doing so, the efficiency and flexibility achieved by MWNI is greatly compromised.

References

Aki, K., and Richards, P. G., 1980, Quantitative seismology: Theory and methods: W. H. Freeman and Co.

Bagaini, C., and Spagnolini, U., 1993, Common shot velocity analysis by shot continuation operator: 63rd Ann. Internat. Mtg, 673–676.

Bagaini, C., and Spagnoliniz, U., 1996, 2-d continuation operators and their applications: Geophysics, **61**, no. 06, 1846–1856.

Berkhout, A. J., and Wapenaar, C. P. A., 1990, Delphi: Delft philosophy on acoustic and elastic inversion: The Leading Edge, **09**, no. 02, 30–33.

Berkhout, A. J., 1994, Seismic resolution, resolving power of acoustical eco techniques: Handbook of geophysical exploration, seismic exploration:, volume 12 Geophysical Press.

Bingham, C., Godfrey, M. D., and Tukey, J. W., 1967, Modern techniques of power spectrum estimation: IEEE Trans. AU.

Biondi, B., and Palacharla, G., 1996, 3-d prestack migration of common-azimuth data: Geophysics, **61**, 1822–1832.

Bolondi, G., Loinger, E., and Rocca, F., 1982, Offset continuation of seismic sections: Geophysical prospecting, **30**, 813–828.

Cabrera, S. D., and Parks, T. W., 1991, Extrapolation and spectral estimation with iterative weighted norm modification: IEEE Transactions on Signal Processing, **39**, no. 4, 842–850.

Campell, S., and Meyer, C., 1979, Generalized inverses of linear transformations: Pitman Publ. Ltd.

Canning, A., and Gardner, G. H. F., 1998, Reducing 3-d acquisition footprint for 3-d dmo and 3d prestack migration: Geophysics, **63**, 1177–1183.

Cary, P., 1997, High-resolution 'beyond nyquist' stacking of irregularly sampled and spare 3d seismic data: Annual Meeting Abstracts, CSEG, pages 66–70.

Castagna, J. P., and Smith, S. W., 1994, Comparison of avo indicators: A modeling study: Geophysics, **59**, no. 12, 1849–1855.

Chemingui, N., 1999, Imaging irregularly sampled 3d prestacked data: Ph.D. thesis, Stanford University.

Claerbout, J. F., 1985, Imaging the earth's interior: Blackwell Scienfific Publications.

Claerbout, J. F., 1992, Earth soundings analysis: Processing versus inversion: Blackwell Scientific Publication.

Cordsen, A., Calbraith, M., and Peirce, J., 2000, Planing land 3-d seismic surveys: Soc. of Expl. Geophys.

Crawley, S., Claerbout, J. F., and Clapp, R., 1999, Interpolation with smoothly nonstationary prediction-error filters: 69th Ann. Internat. Mtg., Soc. of Expl. Geophys., Expanded Abstracts, pages 1154–1157.

Davis, P. J., 1979, Circulant matrices: Willey.

de Bruin, C. G. M., Wapenaar, C. P. A., and Berkhout, A. J., 1990, Angle-dependent reflectivity by means of prestack migration: Geophysics, **55**, no. 09, 1223–1234.

Dudgeon, D. E., and Mersereau, R., 1984, Multidimensional digital signal processing: Prentice-hall.

Duijndam, A. J. W., Schonewille, M., and Hindriks, K., 1999, Reconstruction of seismic signals, irregularly sampled along one spatial coordinate: Geophysics, **64**, 524–538.

Duquet, B., Marfurt, K. J., and Dellinger, J., 2000, Kirchhoff modeling, inversion for reflectivity, and subsurface illumination: Geophysics, **65**, no. 4, 1195–1209.

Fomel, S., 2003, Seismic reflection data interpolation with differential offset and shot continouation: Geophysics, **68**, no. 2, 733–744.

Golub, G., and Reinsch, C., 1970, Singular value decomposition and least squares solution: Numer. Math., **14**, 403–420.

Goodway, W. N., and Ragan, B., 1995, Focused 3d: Consequences of mid-point scatter and spatial sampling in acquisition design: Ann. Mtg. Can. Soc. of Expl. Geophys., pages 177–178.

Gray, S., 1997, True-amplitude seismic migration: A comparison of three approaches: Geophysics, **62**, no. 3, 929–936.

Gulunay, N., and Chambers, R. E., 1996, Unaliased f-k domain trace interpolation: 66th Ann. Internat. Mtg. Soc. of Expl. Geophys., Expanded Abstracts, pages 1461–1464.

Gulunay, N., and Chambers, R. E., 1997, Generalized f-k domain trace interpolation: 67th Ann. Internat. Mtg. Soc. of Expl. Geophys., Expanded Abstracts, pages 1100–1103.

Gulunay, N., 2003, Seismic trace interpolation in the fourier transform domain: Geophysics, **68**, no. 1, 355–369.

Guo, J., Zhou, X., Yang, H. J., and Diao, S., 1996, Efficient f-k domain seismic trace interpolation for spatially aliased data: 66th Ann. Internat. Mtg. Soc. of Expl. Geophys., Expanded Abstracts, pages 1458–1460.

Haber, E., 1997, Numerical strategies for the solution of inverse problems: Ph.D. thesis, University of British Columbia.

Hansen, P. C., 1998, Rank-deficient & discrete ill-posed problems: Numerical aspects of linear inversion: SIAM.

Herrmann, P., Mojesky, T., Magesan, M., and Hugonnet, P., 2000, De-aliased, high-resolution radon transforms.: 70th Ann. Internat. Mtg., Soc. of Expl. Geophys., Expanded Abstracts, pages 1953–1956.

Hestenes, M., and Stiefel, E., 1952, Methods of conjugate gradients for solving linear systems: Nat. Bur. Standards J. Res., **49**, 403–436.

Hestenes, M., 1975, Pseudoinverses and conjugate gradients: Comm. ACM, **18**, 40–43.

Hindriks, K., and Duijndam, A. J. W., 2000, Reconstruction of 3-d seismic signals irregularly sampled along two spatial coordinates: Geophysics, **65**, 253– 256.

Hindriks, K., Duijndam, A. J. W., and Schonewille, M. A., 1997, Reconstruction of two-dimensional irregularly sampled wavefields: Ann. Internat. Mtg., Soc. of Expl. Geophys., Expanded Abstracts, pages 1163–1166.

Hugonnet, P., and Canadas, G., 1997, Regridding of irregular data using 3-d radon decompositions: 67th Ann. Internat. Mtg: Soc. of Expl. Geophys., Expanded Abstracts, pages 1111–1114.

Hugonnet, P., Herrmann, P., and Ribeiro, C., 2001, High resolution radon - a review: 63rd Mtg., Eur. Assn. of Expl. Geophys., Expanded Abstracts.

Jain, A., and Ranganath, S., 1981, Extrapolation algorithms for discrete signals with application in spectrum estimation: IEEE Trans. Acoust. Speech and Signal Processing, **29**, 830–845.

Jakubowicz, H., 1994, Wavefield reconstruction: 64th Ann. Internat. Meg., Soc. Expl. Geophys., pages 1557–1560.

Kao, C. N., 1997, A trace interpolation method for spatially aliased and irregularly spaced seismic data: 67nd Annual Mtg. Soc. Expl. Geophys., Expanded Abstracts, pages 1108–1110.

Kuehl, H., and Sacchi, M. D., 2002, Robust avp estimation using ls wave-equation migration: 72nd Annual Mtg. Soc. Expl. Geophys., Expanded Abstracts.

Kuehl, H., and Sacchi, M. D., 2003, Least-squares wave-equation migration for avp/ava inversion: Geophysics, **68**, no. 1, 262–273.

Kuehl, H., 2002, Least-squares wave-equation migration/inversion: Ph.D. thesis, University of Alberta.

Larner, K., Gibson, B., and Rothman, D., 1981, Trace interpolation and the design of seismic survey: Geophysics, **46**, 407–?

Liu, B., and Sacchi, M. D., 2001, Minimum weighted norm interpolation of seismic data with adaptive weights: 71st Ann. Internat. Mtg., Soc. of Expl. Geophys., Expanded Abstracts, pages 1921–1924.

Liu, B., and Sacchi, M. D., 2003, 2d/3d seismic wavefield reconstruction for ava imaging: 71st Ann. Internat. Mtg., Soc. of Expl. Geophys., Expanded Abstracts, pages 235–238.

Lu, L., 1985, Application of local slant stack to trace interpolation: 55th Ann. Internat. Mtg: Soc. of Expl. Geophys., Expanded Abstracts, pages 560–562.

Lyons, R. G., 1997, Understanding digital signal processing: Prentice Hall.

Mazzucchelli, P., Rocca, F., Spagnolini, U., and Spitz, S., 1998, Wavefield interpolation-continuation or prediction filter techniques?: 60th EAGE Conference, Extended Abstracts, pages 2–51.

Mosher, C., and Foster, D., 2000, Common angle imaging conditions for prestack depth migration: 70th Ann. Internat. Mtg., Soc. of Expl. Geophys., Expanded Abstracts, pages 830–833.

Mosher, C. C., Keho, T. H., Weglein, A. B., and Foster, D. J., 1996, The impact of migration on avo: Geophysics, **61**, 1603–1615.

Mosher, C. C., Foster, D. J., and Hassanzadeh, S., 1997, Common angle imaging with offset plane waves: 67nd Annual Mtg. Soc. Expl. Geophys., Expanded Abstracts, pages 1379–1382.

Nemeth, T., Wu, C., and Schuster, G. T., 1999, Least-squares migration of incomplete reflaction data: Geophysics, **64**, 208–221.

Oppenheim, A. V., and Schafer, R. W., 1989, Discrete-time signal processing: Prentice-Hall, second edition.

Oppenheim, A. V., Willsky, A. S., and Young, I. T., 1983, Signals and systems: Prentice-Hall.

Petersen, D. P., and Middleton, D., 1962, Sampling and reconstruction of wave-number limited functions in n-dimensional euclidean spaces: Information and Control, **5**, 279–323.

Pieprzak, A. W., and McClean, J. W., 1988, Trace interpolation of severely aliased events: 58th Ann. Internat. Mtg., Soc. of Expl. Geophys.

Prucha, M., Biondi, B., and Symes, W., 1999, Angle domain common image gathers by wave-equation migration: 69nd Annual Mtg. Soc. Expl. Geophys., Expanded Abstracts, pages 824–827.

Resnick, J. R., Ng, P., and Larner, K., 1986, Amplitude versus offset analysis in the presence of dip: 56th Ann. Internat. Mtg., Soc. of Expl. Geophys., Expanded Abstracts, pages 617–620.

Rickett, J. E., 2002, Offset and angle-domain common image-point gathers for shot-profile migration: Geophysics, **67**, no. 3, 883–889.

Ronen, J., 1987, Wave-equation trace interpolation: Geophysics, **52**, 973–984.

Russell, B. Practical inversion:. Presented at the CSEG Continuing Education Doodle Train, 2003.

Sacchi, M. D., and Kuehl, H., 2001, Arma formulation of fx prediction error filters and projection filters: Journal of Seismic Exploration, **9**, 185–197.

Sacchi, M. D., and Ulrych, T. J., 1996, Estimation of the discrete fourier transform, a linear inversion approach: Geophysics, **61**, 1128–1136.

Sacchi, M. D., Ulrych, T. J., and Walker, C., 1998, Interpolation and extrapolation using a high-resolution discrete fourier transform: IEEE Trans. Signal Processing, **46**, no. 1, 31–38.

Sava, P. C., and Fomel, S., 2003, common-image gathers by wavefield continuation methods: Geophysics, **68**, 1065–1074.

Sava, P., Biondi, B., and Fomel, S., 2001, Amplitude-preserved common image gathers by wave-equation migration: 71st Ann. Internat. Mtg., Soc. of Expl. Geophys., Expanded Abstracts, pages 296–299.

Schonewille, M. A., and Duijndam, A. J. W., 1998, Efficient nonuniform fourier and radon filtering and reconstruction: 68th Ann. Internat. Mtg: Soc. of Expl. Geophys., Expanded Abstracts, pages 1692–1695.

Schonewille, M., 2000, Fourier reconstruction of irregularly sampled seismic data: Ph.D. thesis, Delft University of Technology.

Shuey, R. T., 1985, A simplification of the zoeppritz-equations: Geophysics, **50**, no. 4, 609–614.

Soubaras, R., 1995, Prestack random and impulsive noise attenuation by f-x projection filtering: 65th Ann. Internat. Mtg: Soc. of Expl. Geophys., Expanded Abstracts, pages 711–714.

Spitz, S., 1991, Seismic trace interpolation in the f-x domain: Geophysics, **56**, 785–794.

Strang, G., 1986, Introduction of applied mathematics: Wellesley-Cambridge Press.

Tarantola, A., 1987, Inverse problem theory: Methods for data fitting and model parameter esitmation: Elsevier Science Publishing Inc.

Thorson, J. R., 1984, Velocity-stack and slant-stack inversion methods: Ph.D. thesis, Stanford University.

Trad, D. O., Ulrych, T. J., and Sacchi, M. D., 2002, Accurate interpolation with high-resolution time-variant radon transforms: Geophysics, **67**, no. 2, 644–656.

Trad, D. O., 2001, Implementations and applications of the sparse randon transform: Ph.D. thesis, The University of British Columbia.

Tygel, M., Santos, L., and Schleicher, J., 1999, Kirchhoff imaging as a tool for avo/ava analysis: The Leading Edge, **18**, no. 8, 940–945.

Vermeer, G., 1990, Seismic wavefield sampling: Soc. of Expl. Geophys.

Vermeer, G., 1998, 3-d symmetric sampling: Geophysics, **63**, no. 5, 1629–1647.

Versteeg, R. J., 1993, Sensitivity of prestack depth migration to the velocity model: Geophysics, **58**, no. 6, 873–882.

Versteeg, R. J., 1994, The marmousi experience: Velocity model determination on a synthetic complex data set: The Leading Edge, **13**, no. 9, 927–936.

Wang, J., Kuehl, H., and Sacchi, M. D., 2003, Least-squares wave-equation avp imaging of 3d common azimuth data: 73th Ann. Internat. Mtg: Soc. of Expl. Geophys., Expanded Abstracts, pages 1039–1042.

Wapenaar, C. P. A., Van WijngaardenA, J., Geloven, W., and van der Leij, T., 1999, Apparent ava effects of fine layering: Geophysics, **64**, no. 6, 1939–1948.

Yilmaz, O., and Taner, M. T., 1994, Discrete plane-wave decomposition by least-mean-square-error method: Geophysics, **59**, 973–982.

Zheng, Y., Gray, S., Cheadle, S., and Anderson, P., 2001, Factors affecting avo analysis of prestack migrated gathers: 71th Ann. Internat. Mtg., Soc. of Expl. Geophys., Expanded Abstracts, pages 989–992.

Zwartjes, P., and Duijndam, A. J. W., 2000, Optimizing reconstruction for sparse spatial sampling: 70th Ann. Internat. Mtg., Soc. of Expl. Geophys., Expanded Abstracts, pages 2162–2165.

Appendix A

Table of Symbols

SYMBOL	name or discription
1-D, 2-D, 3-D, 4-D	one, two, three, four-dimensional
adj	adjoint
HRFT	high resolution Fourier transform
k_i	wavenumber corresponding to x_i, $i = s, r, m, o$
$\|k_i\|_{\max}$	maximum wavenumber k_i corresponding to $f_{\max}$ and $V_{\max}$
MNI	minimum norm interpolation
MWNI	minimum weighted norm interpolation
n	integer variable
n_1, n_2	n for two dimensions
$\mathbf{n}$	vector of integer variables
N-D	N-dimensional
NMO	normal moveout
$p(\cdot)$	probability density function
P_k^2	spectral domain weights
$\underset{\sim}{\mathbf{Q}}$	circulant convolution filtering matrix
$s(t)$, $s(t_1, t_2)$	periodic impulse train
$S(\Omega)$, $S(\Omega_1, \Omega_2)$	continuous Fourier transform of $s(t)$, $s(t_1, t_2)$
t	time variable
t_1, t_2	independent variables for 2-D signals
$\mathbf{t}$	vector of time variables

SYMBOL	name or discription
T	(1) sampling period (2) superscript for transpose
T_1, T_2	horizontal and vertical sampling intervals
$\underset{\sim}{\mathbf{T}}$	sampling operator
$\underset{\sim}{\mathbf{U}}$	general matrix defining for periodicity of 2-D functions in the Fourier domain
V_1, V_2	medium velocities
V_i	apparent velocity in (t, x_i), $i = s, r, m, o$
$V_{\min}$	minimum phase velocity of events
$\underset{\sim}{\mathbf{V}}$	sampling matrix for 2-D function with arbitrary sampling geometries
w	continuous seismic wavefield
w_m	positive and even window, e.g. a hanning window
W	Fourier transform of continuous seismic wavefield w
$\underset{\sim}{\mathbf{W}}$	weighting matrix
WCSB	Western Canadian Sedimentary Basin
$x(n)$, $x(n_1, n_2)$, $x(\mathbf{n})$	discrete sequence
$x_c(t)$, $x_c(t_1, t_2)$, $x_c(\mathbf{t})$	continuous function
x_m	samples of complete (unknown) data
$x_r(t)$, $x_r(t_1, t_2)$	reconstructed continuous function
$x_s(t)$, $x_s(t_1, t_2)$	sampled continuous function
$X(\omega)$, $X(\omega_1, \omega_2)$, $X(\boldsymbol{\omega})$	DTFT of $x(n)$, $x(n_1, n_2)$, $x(\mathbf{n})$
$X_c(\Omega)$, $X_c(\Omega_1, \Omega_2)$, $X_c(\boldsymbol{\Omega})$	continuous Fourier transform of $x_c(t)$, $x_c(t_1, t_2)$, $x_c(\mathbf{t})$
X_k	DFT of the samples of complete data x_m
$X_s(\Omega)$, $X_s(\Omega_1, \Omega_2)$	continuous Fourier transform of $x_s(t)$, $x_s(t_1, t_2)$
$\mathbf{x}$	vector of complete data
$\hat{\mathbf{x}}$	estimation of $\mathbf{x}$
$\mathbf{x}_m$	midpoint vector (x_m, y_m)
$\mathbf{x}_o$	offset vector (x_o, y_o)
$\mathbf{x}_r$	receiver vector (x_r, y_r)

SYMBOL	name or discription
$\mathbf{x}_s$	shot vector (x_s, y_s)
$\mathbf{X}$	vector of DFT of complete data
(x_m, y_m)	midpoint coordinates
(x_o, y_o)	offset coordinates
(x_r, y_r)	receiver coordinates
(x_s, y_s)	shot coordinates
$\mathbf{y}$	vector of incomplete data
$\delta(t)$, $\delta(t_1, t_2)$	unit impulse function
γ	angle of incidence
$\mathcal{K}$	region of spectral support
$\underline{\underline{\mathbf{\Lambda}}}$	diagonal matrix
ρ	trade off parameter
ρ_1, ρ_2	medium density
σ_c	scale parameter
σ_n^2	variance of noise
ω	angular frequency defined by DTFT
ω_1, ω_2	ω for two dimensions
$\boldsymbol{\omega}$	vector of angular frequencies defined by DTFT
Ω	frequency variable defined by continuous Fourier transform
Ω_1, Ω_2	Ω for two dimensions
Ω_c	cutoff frequency for low-pass filter
Ω_N	Nyquist sampling frequency
Ω_s	sampling frequency
$\mathbf{\Omega}$	vector of frequency variables defined by continuous Fourier transform
$\|\| \cdot \|\|_w$	a weighted norm
$*$	(1) convolution (2) superscript for conjugate transpose
$\dagger$	superscript for pseudoinverse
$\otimes$	kronecker product

Appendix B

Sampling in shot-receiver and midpoint/offset domain

The wavefield sampling in the shot-receiver domain/midpoint-offset domain can be represented by a sampling matrix. The sampling matrix defines the general matrix that describes the periodicity of the spectrum of the sampled wavefield according to equation (2.2.27). In this appendix, we derive general matrices for the sampling matrices $\underset{\sim}{\mathbf{V}}_{sr}$ and $\underset{\sim}{\mathbf{V}}_{mo}$ defined by equations (2.3.15) and (2.3.19).

Giving sampling matrices $\underset{\sim}{\mathbf{V}}_{sr}$ defined by equation (2.3.15), we can write general matrices $\underset{\sim}{\mathbf{U}}_{sr}$ of frequency panel according to equation (2.2.27):

$$\underset{\sim}{\mathbf{U}}_{sr} = 2\pi(\underset{\sim}{\mathbf{V}}_{sr})^{-1})' \tag{B.0.1}$$

$$= 2\pi\frac{1}{\det \underset{\sim}{\mathbf{V}}_{sr}}(\mathrm{adj}(\underset{\sim}{\mathbf{V}}_{sr}))', \tag{B.0.2}$$

where adj denotes adjoint matrix. Since

$$\det \underset{\sim}{\mathbf{V}}_{sr} = (V_{\min}/f_{\max})^2 \tag{B.0.3}$$

and

$$\mathrm{adj}(\underset{\sim}{\mathbf{V}}_{sr}) = \begin{bmatrix} V_{\min}/f_{\max} & 0 \\ 0 & V_{\min}/f_{\max} \end{bmatrix}', \tag{B.0.4}$$

substitute equation (B.0.3) and (B.0.4) into equation (B.0.1), we have

$$\underset{\sim}{\mathbf{U}}_{sr} = 2\pi \begin{bmatrix} f_{\max}/V_{\min} & 0 \\ 0 & f_{\max}/V_{\min} \end{bmatrix}. \tag{B.0.5}$$

Similarly, given $\underset{\sim}{\mathbf{V}}_{mo}$ defined by equation (2.3.19) Since

$$\det \underset{\sim}{\mathbf{V}}_{mo} = -(V_{\min}/f_{\max})^2 \tag{B.0.6}$$

and

$$\operatorname{adj}(\underset{\sim}{\mathbf{V}}_{mo}) = \begin{bmatrix} -V_{\min}/f_{\max} & -V_{\min}/f_{\max} \\ -V_{\min}/2f_{\max} & V_{\min}/2f_{\max} \end{bmatrix}', \tag{B.0.7}$$

we have

$$\underset{\sim}{\mathbf{U}}_{mo} = 2\pi \begin{bmatrix} f_{\max}/V_{\min} & f_{\max}/V_{\min} \\ f_{\max}/2V_{\min} & -f_{\max}/2V_{\min} \end{bmatrix}. \tag{B.0.8}$$

Appendix C

The method of Lagrange Multipliers

The minimum norm solution is found by minimizing the following cost function:

$$J = \boldsymbol{\lambda}^T(\underset{\sim}{\mathbf{T}}\mathbf{x} - \mathbf{y}) + ||\mathbf{x}||^2_{\mathcal{W}} \tag{C.0.1}$$

subject to

$$\underset{\sim}{\mathbf{T}}\mathbf{x} - \mathbf{y} = \mathbf{0} \tag{C.0.2}$$

In the above equation $\boldsymbol{\lambda}$ denotes the vector of Lagrange multipliers. Notes that if when the constraints $\underset{\sim}{\mathbf{T}}\mathbf{x} - \mathbf{y} = \mathbf{0}$ are satisfied then $J \equiv ||\mathbf{x}||^2_{\mathcal{W}}$ and the minimum of J will also give the minimum of $||\mathbf{x}||^2_{\mathcal{W}}$. J is minimized by differentiating with respect to $\mathbf{x}$, which give us

$$2\underset{\sim}{\mathbf{Q}}^{\dagger}\mathbf{x} + \underset{\sim}{\mathbf{T}}^T\boldsymbol{\lambda} = 0\,. \tag{C.0.3}$$

Therefore

$$\begin{aligned} \mathbf{x} &= (2\underset{\sim}{\mathbf{Q}}^{\dagger})^{-1}\underset{\sim}{\mathbf{T}}^T\boldsymbol{\lambda} && \text{(C.0.4)} \\ &= \frac{1}{2}\underset{\sim}{\mathbf{Q}}\underset{\sim}{\mathbf{T}}^T\boldsymbol{\lambda}\,. && \text{(C.0.5)} \end{aligned}$$

Substitute $\mathbf{x}$ from equation (C.0.5) to equation (C.0.2), we have

$$\boldsymbol{\lambda} = -2(\underset{\sim}{\mathbf{T}}\underset{\sim}{\mathbf{Q}}\underset{\sim}{\mathbf{T}}^T)^{-1}\mathbf{y} \tag{C.0.6}$$

substitute $\boldsymbol{\lambda}$ in equation (C.0.6) back into equation (C.0.5), we have

$$\hat{\mathbf{x}} = \underset{\sim}{\mathbf{Q}}\underset{\sim}{\mathbf{T}}^T(\underset{\sim}{\mathbf{T}}\underset{\sim}{\mathbf{Q}}\underset{\sim}{\mathbf{T}}^T)^{-1}\mathbf{y} \tag{C.0.7}$$

as shown in equation (3.2.15).

Appendix D

Reduction to standard form

The original cost function to minimize (as shown in equation (3.2.18)) is

$$J = ||\underset{\sim}{\mathbf{T}}\mathbf{x} - \mathbf{y}||^2 + \rho^2 ||\mathbf{x}||^2_{\mathcal{W}}, \tag{D.0.1}$$

where ρ^2 is the trade-off parameter of the problem. Minimizing J is equivalent to find the least-squares solution of overdetermined system of equation

$$\begin{pmatrix} \underset{\sim}{\mathbf{T}} \\ \rho\underset{\sim}{\mathbf{W}} \end{pmatrix} \mathbf{x} \approx \begin{pmatrix} \mathbf{y} \\ \mathbf{0} \end{pmatrix} \tag{D.0.2}$$

as shown in equation (3.2.19), where the matrix of weights $\underset{\sim}{\mathbf{W}}$ is given by

$$\underset{\sim}{\mathbf{W}} = \underset{\sim}{\mathbf{\Lambda}}^{\dagger 1/2} \underset{\sim}{\mathbf{F}}. \tag{D.0.3}$$

If $\underset{\sim}{\mathbf{W}}$ is well posed, then let $\mathbf{z} = \underset{\sim}{\mathbf{W}}\mathbf{x}$, equation (D.0.1) can be rewritten as

$$J = ||\underset{\sim}{\mathbf{T}}\underset{\sim}{\mathbf{W}}^{-1}\mathbf{z} - \mathbf{y}||^2 + \rho^2 ||\mathbf{z}||^2_{\mathcal{W}}. \tag{D.0.4}$$

Define $\hat{\underset{\sim}{\mathbf{T}}} = \underset{\sim}{\mathbf{T}}\underset{\sim}{\mathbf{W}}^{-1}$, the problem is now in its standard form (Haber, 1997). Minimize this new objective function is equivalent to find the least-squares solution of overdetermined system of equation

$$\begin{pmatrix} \underset{\sim}{\mathbf{T}}\underset{\sim}{\mathbf{W}}^{-1} \\ \rho\underset{\sim}{\mathbf{I}} \end{pmatrix} \mathbf{z} \approx \begin{pmatrix} \mathbf{y} \\ \mathbf{0} \end{pmatrix}. \tag{D.0.5}$$

However, we have defined $\underset{\sim}{\mathbf{W}}$ as a band limiting operator, it has a non-empty null space , the set $\{\mathbf{x}_0 : \underset{\sim}{\mathbf{W}}\mathbf{x} = \boldsymbol{\theta}\}$, where $\boldsymbol{\theta}$ denotes the null vector. Let $\mathbf{z} = \underset{\sim}{\mathbf{W}}\mathbf{x}$, and $\underset{\sim}{\mathbf{W}}^{\dagger}$ be the pseudo-inverse of $\underset{\sim}{\mathbf{W}}$, the solution of $\mathbf{x}$ can be divided into two parts, $\mathbf{x}_W$ which is in

the active space of $\underset{\sim}{\mathbf{W}}$, and $\mathbf{x}_o$ which is in the null space of $\underset{\sim}{\mathbf{W}}$:

$$\begin{aligned} \mathbf{x} &= \mathbf{x}_W + \mathbf{x}_0 && \text{(D.0.6)} \\ &= \underset{\sim}{\mathbf{W}}^{\dagger}\mathbf{z} + \underset{\sim}{\mathbf{W}}_0\mathbf{z_0}\,, && \text{(D.0.7)} \end{aligned}$$

where $\underset{\sim}{\mathbf{W}}_0$ denotes matrix which contains the null space of $\underset{\sim}{\mathbf{W}}$, i.e. $\underset{\sim}{\mathbf{W}}\underset{\sim}{\mathbf{W}}_0 = 0$. Substitute equation (D.0.7) into equation (3.2.19) gives:

$$\begin{pmatrix} \underset{\sim}{\mathbf{T}} \\ \rho\underset{\sim}{\mathbf{W}} \end{pmatrix} [\underset{\sim}{\mathbf{W}}^{\dagger}\mathbf{z} + \underset{\sim}{\mathbf{W}}_0\mathbf{z_0}] \approx \begin{pmatrix} \mathbf{y} \\ \mathbf{0} \end{pmatrix} \tag{D.0.8}$$

This is equivalent to these two systems equations:

$$\underset{\sim}{\mathbf{T}}\underset{\sim}{\mathbf{W}}^{\dagger}\mathbf{z} + \underset{\sim}{\mathbf{T}}\underset{\sim}{\mathbf{W}}_0\mathbf{z}_0 = \mathbf{y} \tag{D.0.9}$$

$$\rho(\underset{\sim}{\mathbf{W}}\underset{\sim}{\mathbf{W}}^{\dagger}\mathbf{z} + \underset{\sim}{\mathbf{W}}\underset{\sim}{\mathbf{W}}_0\mathbf{z}_0) = \rho\underset{\sim}{\mathbf{W}}\underset{\sim}{\mathbf{W}}^{\dagger}\mathbf{z} = \mathbf{0} \tag{D.0.10}$$

First, $\underset{\sim}{\mathbf{W}}$ is underdetermined therefore $\underset{\sim}{\mathbf{W}}\underset{\sim}{\mathbf{W}}^{\dagger}$ is identity matrix. Also, The fact that we are solving for a band limited solution ($k \in \mathcal{K}$), means that

$$\mathbf{x}_0 = \underset{\sim}{\mathbf{W}}_0\mathbf{z}_0 = \boldsymbol{\theta}$$

Therefore, equation (D.0.2) can be transform into

$$\begin{pmatrix} \underset{\sim}{\mathbf{T}}\underset{\sim}{\mathbf{W}}^{\dagger} \\ \rho\underset{\sim}{\mathbf{I}} \end{pmatrix} \mathbf{z} \approx \begin{pmatrix} \mathbf{y} \\ \mathbf{0} \end{pmatrix}, \tag{D.0.11}$$

which is shown in equation (3.2.23). In this case, we are equivalently minimizing a objective function

$$J = ||\underset{\sim}{\mathbf{T}}\underset{\sim}{\mathbf{W}}^{\dagger}\mathbf{z} - \mathbf{y}||^2 + \rho^2||\mathbf{z}||^2_{\mathcal{W}}\,. \tag{D.0.12}$$

Define $\hat{\underset{\sim}{\mathbf{T}}} = \underset{\sim}{\mathbf{T}}\underset{\sim}{\mathbf{W}}^{\dagger}$, the problem is now in its standard form.